

# Shear-flexible geometrically exact beam element based on finite differences

Milan Jirásek<sup>a</sup>, Martin Horák<sup>a,c</sup>, Emma La Malfa Ribolla<sup>b,\*</sup>, Chiara Bonvissuto<sup>b</sup>

<sup>a</sup>*Department of Mechanics, Faculty of Civil Engineering,  
Czech Technical University in Prague, Czech Republic*

<sup>b</sup>*Department of Engineering, University of Palermo, Italy*

<sup>c</sup>*Institute of Information Theory and Automation,  
Czech Academy of Sciences, Czech Republic*

---

## Abstract

The proposed two-dimensional geometrically exact beam element extends our previous work by including the effects of shear distortion, and also of distributed forces and moments acting along the beam. The general flexibility-based formulation exploits the kinematic equations combined with the inverted sectional equations and the integrated form of equilibrium equations. The resulting set of three first-order differential equations is discretized by finite differences and the boundary value problem is converted into an initial value problem using the shooting method. Due to the special structure of the governing equations, the scheme remains explicit even though the first derivatives are approximated by central differences, leading to high accuracy. The main advantage of the adopted approach is that the error can be efficiently reduced by refining the computational grid used for finite differences at the element level while keeping the number of global degrees of freedom low. The efficiency is also increased by dealing directly with the global centerline coordinates and sectional inclination with respect to global axes as the primary unknowns at the element level, thereby avoiding transformations between local and global coordinates.

Two formulations of the sectional equations, namely the widely used Reissner model and a less common version referred to as the Ziegler model, are presented and compared. In particular, stability of an axially loaded beam/column is investigated and the connections to the Haringx and En-

---

\*Corresponding author. Tel.: +39 09123896570

*Email address:* [emma.lamalfaribolla@unipa.it](mailto:emma.lamalfaribolla@unipa.it) (Emma La Malfa Ribolla)

gesser stability theories are discussed. Both approaches are tested in a series of numerical examples, which illustrate (i) high accuracy with quadratic convergence when the spatial discretization is refined, (ii) easy modeling of variable stiffness along the element (such as rigid joint offsets), (iii) efficient and accurate characterization of the buckling and post-buckling behavior.

*Keywords:* geometrically nonlinear beam, shear flexible beam, large rotations, shooting method, buckling, stability

---

## 1. Introduction

In a wide range of applications and scientific areas, including mechanical and structural engineering, biomedical engineering, and soft robotics, slender beam- or rod-like elements are essential constituents. Examples are lattice-based metamaterials, which exploit structural topology to achieve certain favorable mechanical and physical properties, high-tensile industrial webbings, hard-magnetic soft rods and biomedical prostheses. The need to predict the mechanical behavior of these flexible structures has stimulated the development of increasingly efficient and robust computational tools based on the pioneering finite-strain beam models.

Long slender bodies can be modeled using various rod [1] and beam theories. To introduce the terminology used throughout the paper, several pivotal studies on large-strain beam models are mentioned below. The origins date back to Euler's formulation [2] based on the assumptions of (i) perpendicularity between the beam centerline and cross sections and (ii) axial inextensibility. The Kirchhoff model [3] enhanced the formulation to account for axial strain and torsion, while still neglecting the shear strain. Under the assumptions of small displacements and rotations, the effects of shear were included in the Timoshenko-Ehrenfest beam theory [4]. Much later, Reissner [5] proposed the first full formulation that accounts for the shear distortion without kinematic restrictions. Based on Reissner's work, Simo [6] developed a formulation known as the geometrically exact beam theory, which is truly consistent in the sense that the kinematic quantities and relations are systematically derived from the 3D continuum theory, while the constitutive law is postulated. Various numerical implementations were based on finite element approaches, corotational methods [7, 8, 9], Absolute Nodal Coordinate formulations [10, 11], Lagrangian approaches [12], finite differences [13] and iso-geometric schemes [14, 15].

It should be emphasized that the Reissner–Simo beam model accounting for transverse shear deformation can lead to shear locking for displacement-

based finite element formulations[16, 17]. Substantial research work related to the shear-deformable beam model has been conducted and, even recently, new theoretical[18, 19] as well as computational[20, 21] developments have been proposed. In a recent study, Kim et al. [22] have listed various possible choices of the internal forces in shear-flexible models.

In our recent papers, we have presented a geometrically exact formulation for the planar behavior of beams that are initially straight [23] or curved[24]. Locally, the beam is treated by finite differences, but in the context of structural analysis it plays the same role as a traditional finite element. The advantage is that the accuracy of the numerical approximation can be increased by refinement of the finite difference grid while keeping the number of global degrees of freedom constant. A locking-free behavior is observed, which is closely related to the fact that no a priori chosen shape functions for the kinematic approximation are needed.

The present study extends the beam element from[24] by incorporating the effects of (i) shear distortion and (ii) distributed external forces and moments acting along the beam. In addition to the theoretical enhancement, the numerical scheme is also improved by a modified choice of the primary variables (centerline coordinates instead of displacements), which eliminates the need to convert variables from local to global reference systems.

In the following, a brief outline of the paper content is provided. In Section 2, two models which differ in the choice of the basic deformation variables are briefly presented and the fundamental equations are summarized (their detailed derivation can be found in Appendix A). The first model (Section 2.2), referred to as the *Reissner* model, is characterized by stretching and shear deformation variables work-conjugate to internal forces perpendicular and parallel to the deformed section, respectively. In this case, axial stiffness is activated only by the change of distance between the neighboring sections and not by parallel sliding of the sections. This choice finds its corresponding buckling model in the work of Haringx [25], who studied the stability of helical springs. The second model (Section 2.3), referred to as the *Ziegler* model, is characterized by stretching and shear deformation variables work-conjugate to internal forces parallel and perpendicular to the deformed centerline, respectively. In this case, axial stretching occurs also during parallel sliding of sections. Such approach can be considered as an extension of the original Engesser model for stability of a shear-deformable column [26] to the axially compressible case, as presented by Ziegler [27].

For both models, Section 3 shows how to treat the fundamental equations numerically in a general case by an efficient procedure that exploits the idea of the shooting method. In Section 4, numerical simulations of several exam-

ples are performed and compared with existing solutions from the literature and with the analytical solution from Appendix B. Additional examples related to bifurcations from the straight state and to the subsequent post-critical response are presented in Section 5, where the numerical results are compared with analytical solutions derived in Appendix C. Finally, Section 6 summarizes the conclusions and discusses possible extensions.

Throughout the paper, we will consistently use the following terminology:

- **Euler** refers to the 2D beam with an inextensible centerline and with sections perpendicular to the centerline, which deforms only by **bending**.
- **Kirchhoff** is used for the beam with sections perpendicular to the centerline, which deforms by **axial stretching** and **bending** (in 3D also by torsion).
- **Reissner** and **Ziegler** are two formulations that, in addition to **axial stretching** and **bending**, incorporate also the effect of **shear** distortion.

In particular, it is worth noting that we consider the Kirchhoff beam as axially extensible, even though this is not always recognized in the literature. For instance, Kirchhoff rods are in [1] considered as the 3D extension of Euler’s elastica, with torsion included but axial deformation still neglected. However, Kirchhoff’s original paper [3] explicitly includes a term that accounts for changes in the centerline length.

## 2. Shear-flexible beam model

### 2.1. Basic assumptions and variables

In the Timoshenko beam theory[4], the condition of normality between the section and the deformed centerline (i.e., the Euler-Bernoulli hypothesis) is relaxed, and the transverse shear strain is no longer zero. In one of his classic papers, Reissner[5] presented a shear-flexible planar beam model that can be considered as a geometrically exact extension of the Timoshenko approach to large strains, since the relations between the deformation variables and the kinematic variables characterizing the displacements and rotations do not exploit any simplifications based on the assumed smallness of certain quantities.

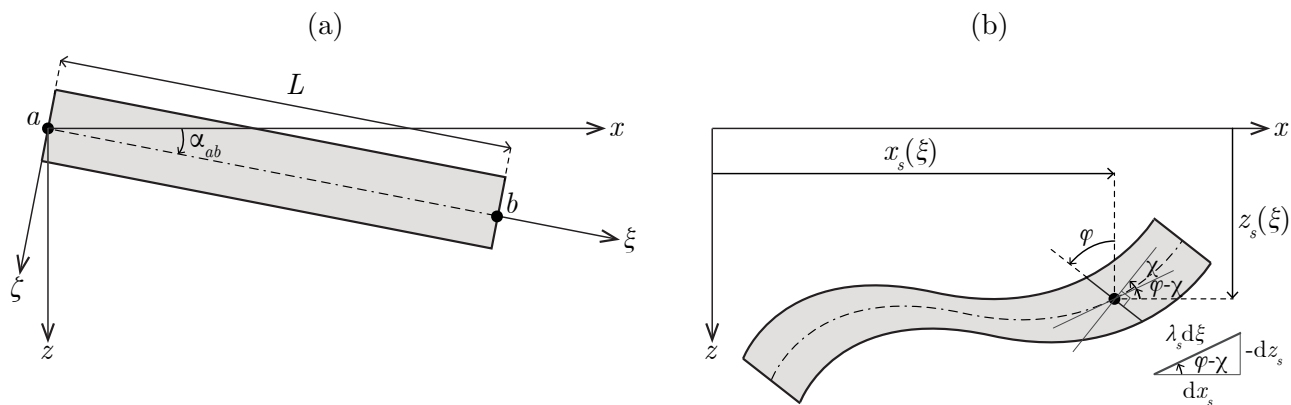


Figure 1: Kinematics of the geometrically exact beam model in the global  $x$ - $z$  plane: (a) undeformed straight beam and (b) deformed beam.

Consider an initially straight planar beam of length  $L$ , which connects joints  $a$  and  $b$  located in the global  $x$ - $z$  plane of the global coordinate system, as indicated in Fig. 1a. A generic section initially located at distance  $\xi$  from the left end is in the deformed state described by (i) coordinates  $x_s$  and  $z_s$  of its centroid and (ii) inclination angle  $\varphi$  between the section (assumed to remain plane) and the global  $z$ -axis. The angle between the tangent to the deformed centerline and the normal to the section, denoted here as  $\chi$ , represents the shear distortion. Based on the geometry of the infinitesimal triangle shown in Fig. 1b, it is possible to express the shear angle

$$\chi = \varphi - \arctan \frac{-dz_s}{dx_s} = \varphi + \arctan \frac{z'_s}{x'_s} \quad (1)$$

and also the centerline stretch

$$\lambda_s = \frac{1}{d\xi} \sqrt{dx_s^2 + dz_s^2} = \sqrt{x_s'^2 + z_s'^2} \quad (2)$$

Primes denote here derivatives with respect to  $\chi$ . The bending part of deformation is characterized by the curvature, usually defined as

$$\kappa = \frac{d\varphi}{d\xi} = \varphi' \quad (3)$$

For a Kirchhoff beam, the shear distortion is neglected, the infinitesimal segment is decomposed into individual fibers parallel to the centerline, and each fiber is considered to be under uniaxial tension. The stretch and thus

also the strain in each fiber can be linked to the centerline stretch and curvature by a simple relation. Therefore, one can start from a given uniaxial hyperelastic stress-strain law, characterized by an expression for the strain energy density (per unit volume) as a function of strain, and then integrate over the section and construct the corresponding strain energy density per unit length, considered as a function of the axial strain and curvature. In this way, the sectional equations that link the deformation variables to the internal forces can be deduced in a consistent way from the selected constitutive model; see for instance [24, 28, 29].

Extension of this approach to shear-flexible beam models is in principle possible but is not straightforward, because it is no longer sufficient to work with a uniaxial stress-strain law. Unless the application area is restricted to small-strain cases, the effects of the longitudinal fiber strain and the shear strain become coupled, and the transversal normal strain needs to be eliminated based on a suitable assumption regarding the stress state. The resulting mathematical problem is tractable in closed form only in rare cases. Therefore, a simple alternative route is frequently taken, and the strain energy density is directly postulated on the level of an infinitesimal beam segment, as a function of properly selected deformation variables. Two formulations of this kind are presented in detail in Appendix A, and the resulting equations are summarized in the next two sections.

## 2.2. Reissner model

The sectional equations in the form originally suggested by Reissner [5] can be written as

$$N = EA\varepsilon, \quad Q = GA_s\gamma, \quad M = EI\kappa \quad (4)$$

They link the deformation variables

$$\varepsilon = \lambda_s \cos \chi - 1, \quad \gamma = \lambda_s \sin \chi, \quad \kappa = \varphi' \quad (5)$$

to the work-conjugate internal forces, with the normal force  $N$  understood as the component perpendicular to the section, and the shear force  $Q$  as the component parallel to the section. Symbol  $M$  denotes the bending moment, and  $EA$ ,  $GA_s$  and  $EI$  are the sectional stiffnesses related to axial stretching, shear distortion and bending. It is useful to remark that the deformation variables  $\varepsilon$  and  $\gamma$  defined in (5) can be directly linked to the kinematic variables  $x_s$ ,  $z_s$  and  $\varphi$ , making use of relations (1)–(2). In particular, in Appendix A.1 it is shown that

$$x'_s = (1+\varepsilon) \cos \varphi + \gamma \sin \varphi, \quad z'_s = \gamma \cos \varphi - (1+\varepsilon) \sin \varphi, \quad \varphi' = \kappa \quad (6)$$

where the last equation is just copied from (5c).

A variational approach elaborated in detail in Appendix A.1 leads to equilibrium equations in the differential form (A.21-A.23) and to boundary conditions (A.25-A.30). After integration, the equilibrium equations read

$$N = -(X_{ab} + P_x) \cos \varphi + (Z_{ab} + P_z) \sin \varphi \quad (7)$$

$$Q = -(X_{ab} + P_x) \sin \varphi - (Z_{ab} + P_z) \cos \varphi \quad (8)$$

$$M = -M_{ab} + X_{ab}(z_s - z_a) - Z_{ab}(x_s - x_a) + M_p \quad (9)$$

where

$$P_x(\xi) = \int_0^\xi p_x(s) ds \quad (10)$$

$$P_z(\xi) = \int_0^\xi p_z(s) ds \quad (11)$$

$$M_p(\xi) = -\int_0^\xi m(s) ds + \int_0^\xi P_x(s) z'_s(s) ds - \int_0^\xi P_z(s) x'_s(s) ds \quad (12)$$

are functions that can be deduced from the prescribed distributed load intensities  $p_x$ ,  $p_z$  and  $m$ . In the above,  $X_{ab}$ ,  $Z_{ab}$  and  $M_{ab}$  are constants that represent the global components of the force and the moment between the left end of the beam and the joint to which it is attached (see Fig. 2), and  $x_a$  and  $z_a$  are the current coordinates of the centroid of the left end section, i.e.,  $x_a = x_s(0)$  and  $z_a = z_s(0)$ .

Equations (4) and (6)–(9) can be combined into a set of three first-order differential equations that form the basis of the numerical scheme to be developed next. Such combined equations (A.43)–(A.45) presented in Appendix A.1 are rather lengthy, and so the algorithm actually implements individual equations (4) and (6)–(9) as intermediate steps, to keep the procedure transparent.

### 2.3. Ziegler model

The path to the formulation that we refer to as the Ziegler model is described in Appendix A.2. The selected deformation  $\varepsilon_s = \lambda_s - 1$ ,  $\chi$  and  $\kappa$  are linked to the internal forces by sectional equations

$$\tilde{N} = EA\varepsilon_s, \quad \tilde{Q} = GA_s\chi, \quad M = EI\kappa \quad (13)$$

The difference compared to the Reissner model is that the axial stretching mode is characterized by axial strain  $\varepsilon_s$  and the shear mode by the shear angle  $\chi$ , which leads to work-conjugate internal forces  $\tilde{N}$  and  $\tilde{Q}$  that represent

the components in the direction parallel and perpendicular to the centerline (and not to the section). Moreover,  $\tilde{Q}$  is actually the force perpendicular to the centerline,  $Q^*$ , multiplied by the axial stretch  $\lambda_s$ ; see Appendix A.2 for a detailed explanation. The variational approach then leads to differential equilibrium equations which, after integration, have the form

$$\tilde{N} = -(X_{ab} + P_x) \cos(\varphi - \chi) + (Z_{ab} + P_z) \sin(\varphi - \chi) \quad (14)$$

$$Q^* = -(X_{ab} + P_x) \sin(\varphi - \chi) - (Z_{ab} + P_z) \cos(\varphi - \chi) \quad (15)$$

$$M = -M_{ab} + X_{ab}(z_s - z_a) - Z_{ab}(x_s - x_a) + M_p \quad (16)$$

where  $Q^* = \tilde{Q}/\lambda_s$  is the true shear force. Relations (6) valid for the Reissner model are now replaced by

$$x'_s = (1 + \varepsilon_s) \cos(\varphi - \chi), \quad z'_s = -(1 + \varepsilon_s) \sin(\varphi - \chi), \quad \varphi' = \kappa \quad (17)$$

and the resulting set of three first-order differential equations is given by (A.83)–(A.84) and (A.87) in Appendix A.2.

### 3. Numerical procedures

#### 3.1. Basic concept

##### 3.1.1. Evaluation of generalized end forces

We have shown that, for the assumptions adopted, the description of a shear-flexible beam in the  $x$ - $z$  plane can be reduced to a set of three first-order differential equations for three primary unknown functions,  $x_s$ ,  $z_s$  and  $\varphi$ , which characterize the deformed centerline and the sectional inclination. The numerical solution of these equations will be based on the finite difference scheme. For the solution to be unique, three first-order differential equations require three additional conditions, but for our problem we have a total of six boundary conditions, because the end coordinates and inclinations are supposed to be given (see Fig. 2). At the same time, the governing differential equations contain not only the primary unknown functions and given constants (such as the sectional stiffnesses) but also the left-end forces,  $X_{ab}$  and  $Z_{ab}$ , and the left-end moment,  $M_{ab}$ . Their values need to be determined so that the six kinematic boundary conditions can be satisfied simultaneously. This will be achieved by using a shooting method. Three kinematic boundary conditions at the left end will be used as initial conditions for integration of three first-order differential equations, and the left-end forces and moment will be considered as additional unknown variables (not functions). Their values will first be estimated (for instance, set



to zero, or taken from the previous step or iteration at the structural level), and then iteratively adjusted until the numerically computed right-end coordinates and inclination get sufficiently close to their prescribed values.

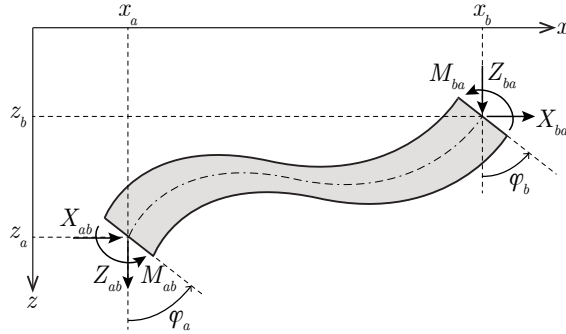


Figure 2: Deformed beam, generalized end coordinates and generalized end forces

To formalize the outlined procedure, let us introduce the column matrices of generalized left-end forces,  $\mathbf{f}_a = (X_{ab}, Z_{ab}, M_{ab})^T$ , generalized right-end forces,  $\mathbf{f}_b = (X_{ba}, Z_{ba}, M_{ba})^T$ , generalized left-end coordinates,  $\mathbf{r}_a = (x_a, z_a, \varphi_a)^T$  and generalized right-end coordinates,  $\mathbf{r}_b = (x_b, z_b, \varphi_b)^T$ . Their meaning is apparent from Fig. 2. Notice that the force components and coordinates are taken with respect to the global coordinate system, and that the inclinations  $\varphi_a$  and  $\varphi_b$  are understood as the angles by which the respective section deviates from the global  $z$ -axis counterclockwise. They differ from the rotations of the structural joints to which the end sections are attached by the initial deviation of the sections from the vertical direction. More specifically, if joints  $a$  and  $b$  rotate by  $\Phi_a$  and  $\Phi_b$ , and the beam centerline in the undeformed state deviates by angle  $\alpha_{ab}$  clockwise from the global  $x$ -axis (as indicated in Fig. 1a), then we have

$$\varphi_a = \Phi_a - \alpha_{ab} \quad (18)$$

$$\varphi_b = \Phi_b - \alpha_{ab} \quad (19)$$

Since, for a given beam,  $\alpha_{ab}$  is a fixed constant, the increments or variations of  $\varphi$  and  $\Phi$  are the same, only the total values differ by a constant. Incorporation of the initial beam position directly into the beam-level algorithm avoids the need for transformation of forces, displacements and coordinates between the global and local (beam-related) coordinate systems.

A numerical algorithm, to be described later, can integrate the governing differential equations along the beam and compute the generalized coordinates of the right end,  $\mathbf{r}_b$ , based on the specified generalized coordinates of

the left end,  $\mathbf{r}_a$ , and generalized left-end forces,  $\mathbf{f}_a$ . This defines a mapping  $\mathbf{g}$  such that

$$\mathbf{r}_b = \mathbf{g}(\mathbf{f}_a, \mathbf{r}_a) \quad (20)$$

If the generalized coordinates at both ends are given, condition (20) can be interpreted as a set of three nonlinear algebraic equations with three unknowns—the generalized forces assembled in  $\mathbf{f}_a$ . This set of equations is solved by the Newton-Raphson method, starting from an initial guess,  $\mathbf{f}_a^{(0)}$ . In a generic iteration number  $k$ , equations (20) are replaced by their linearized version

$$\mathbf{g}(\mathbf{f}_a^{(k-1)}, \mathbf{r}_a) + \mathbf{G}(\mathbf{f}_a^{(k-1)}, \mathbf{r}_a) \Delta \mathbf{f}_a^{(k)} = \mathbf{r}_b \quad (21)$$

where

$$\mathbf{G}(\mathbf{f}_a, \mathbf{r}_a) = \frac{\partial \mathbf{g}(\mathbf{f}_a, \mathbf{r}_a)}{\partial \mathbf{f}_a} \quad (22)$$

is the Jacobi matrix of partial derivatives of function  $\mathbf{g}$  with respect to the first set of arguments,  $\mathbf{f}_a$ . Components of this matrix are computed simultaneously with the evaluation of  $\mathbf{g}$  using consistent linearization of the algorithm around the current solution. The iterative correction

$$\Delta \mathbf{f}_a^{(k)} = \mathbf{G}^{-1}(\mathbf{f}_a^{(k-1)}, \mathbf{r}_a) \left( \mathbf{r}_b - \mathbf{g}(\mathbf{f}_a^{(k-1)}, \mathbf{r}_a) \right) \quad (23)$$

is then added to the current approximation of  $\mathbf{f}_a$ , and an improved approximation

$$\mathbf{f}_a^{(k)} = \mathbf{f}_a^{(k-1)} + \Delta \mathbf{f}_a^{(k)} \quad (24)$$

is evaluated. The iterative loop runs until the norm of the residual  $\mathbf{r}_b - \mathbf{g}(\mathbf{f}_a^{(k)}, \mathbf{r}_a)$  becomes negligibly small (a weighted norm is used, because two components of the residual have the dimension of length while the last one is dimensionless). When convergence is achieved, the most recent approximation  $\mathbf{f}_a^{(k)}$  represents the generalized forces acting on the left end of the beam, which can be directly incorporated into the global equilibrium conditions of joint  $a$  on the structural level. The generalized right-end forces,  $\mathbf{f}_b^{(k)}$ , are provided among the output variables of the algorithm that integrates the fundamental equations along the beam. Alternatively, they can be evaluated from the equilibrium equations written for the whole beam, which lead to

$$X_{ba} = -X_{ab} - P_z(L) \quad (25)$$

$$Z_{ba} = -Z_{ab} - P_z(L) \quad (26)$$

$$M_{ba} = -M_{ab} + X_{ab}(z_b - z_a) - Z_{ab}(x_b - x_a) + M_p(L) \quad (27)$$

The evaluation of  $M_p(L)$  using formula (12) with  $\xi = L$  would require numerical integration, and so it is better to provide the value as one of the output variables of the numerical algorithm, which needs to compute  $M_p$  along the way anyway. In the absence of distributed loading,  $M_p$  vanishes.

### 3.1.2. Evaluation of element stiffness matrix

For the solution of the joint equilibrium equations at the structural level, the beam element must be able to provide not only the end forces, but also the element tangent stiffness matrix, which links infinitesimal increments of generalized end displacements to infinitesimal increments of generalized end forces. Suppose that  $\mathbf{r}_a$  and  $\mathbf{r}_b$  are the prescribed generalized end coordinates and  $\mathbf{f}_a$  are the corresponding generalized left-end forces, calculated from equation (20). Infinitesimal increments of these variables are linked by the linearized form of (20), which can be written as

$$d\mathbf{r}_b = \mathbf{G}(\mathbf{f}_a, \mathbf{r}_a) d\mathbf{f}_a + \mathbf{G}_r(\mathbf{f}_a, \mathbf{r}_a) d\mathbf{r}_a \quad (28)$$

where  $\mathbf{G}$  is the already defined Jacobi matrix of partial derivatives  $\partial\mathbf{g}/\partial\mathbf{f}_a$ , and

$$\mathbf{G}_r = \frac{\partial\mathbf{g}}{\partial\mathbf{r}_a} \quad (29)$$

is another matrix that contains partial derivatives of mapping  $\mathbf{g}$  with respect to the second set of arguments—the generalized left-end displacements.

For simplicity, we will omit the arguments  $\mathbf{f}_a$  and  $\mathbf{r}_a$  in the subsequent derivations. The (infinitesimal) increment of left-end forces that would be caused by increments  $d\mathbf{r}_a$  and  $d\mathbf{r}_b$  of the generalized end coordinates (which coincide with the increments of displacements and rotations of the joints to which the beam element is attached) are easily expressed from (28) as

$$d\mathbf{f}_a = \mathbf{G}^{-1}(d\mathbf{r}_b - \mathbf{G}_r d\mathbf{r}_a) = -\mathbf{G}^{-1}\mathbf{G}_r d\mathbf{r}_a + \mathbf{G}^{-1}d\mathbf{r}_b \quad (30)$$

Consequently, matrix  $-\mathbf{G}^{-1}\mathbf{G}_r$  represents the upper left  $3 \times 3$  block of the tangent element stiffness matrix that links the column  $(d\mathbf{f}_a^T, d\mathbf{f}_b^T)^T$  (increments of generalized end forces) to the column  $(d\mathbf{r}_a^T, d\mathbf{r}_b^T)^T$  (increments of generalized end coordinates or displacements), and matrix  $\mathbf{G}^{-1}$  is the upper right  $3 \times 3$  block of the tangent element stiffness matrix. In this way, we obtain the first three rows of the stiffness matrix, and then, based on equilibrium equations written for the whole beam, we can construct the remaining three rows.

The Jacobi matrix  $\mathbf{G}$  is computed by the end-force evaluation algorithm, because it is needed for the iterative process described by (23)–(24). For

evaluation of the tangent stiffness, we also need matrix  $\mathbf{G}_r$ , but not all of its entries have to be computed numerically. If the left-end coordinates  $x_a$  and  $z_a$  are changed by  $dx_a$  and  $dz_a$  and everything else is kept fixed, then the resulting right-end coordinates  $x_b$  and  $z_b$  will also be changed by  $dx_a$  and  $dz_a$ , and the resulting right-end inclination  $\varphi_b$  will remain unchanged. Physically, one can think of a rigid body translation applied to the deformed beam, which does not disturb the validity of the basic equations. Consequently, the first two columns of matrix  $\mathbf{G}_r$  are  $(1, 0, 0)^T$  and  $(0, 1, 0)^T$ , and the first two columns of matrix  $\mathbf{G}^{-1}\mathbf{G}_r$  will be just copies of the first two columns of  $\mathbf{G}^{-1}$ .

Let us now imagine what happens if the left-end inclination  $\varphi_a$  is changed by  $d\varphi_a$ . One might expect a similar effect as if the whole beam is rotated by  $d\varphi_a$ , keeping the same deformed shape. However, this is true only if the forces acting on the beam rotate as well. For a beam subjected to distributed loading, this cannot be easily emulated, and the third column of  $\mathbf{G}_r$  needs to be evaluated numerically. Only if the beam is not loaded by forces distributed along its length, the third column can be constructed analytically. If we rotate the whole deformed beam and simultaneously also the end forces by  $d\varphi_a$  counterclockwise, then the generalized coordinates at the right end change by  $dx_b = (z_b - z_a)d\varphi_a$ ,  $dz_b = -(x_b - x_a)d\varphi_a$  and  $d\varphi_b = d\varphi_a$ , as an effect of a rigid rotation of the beam, during which the deformed shape remains the same. The same change can be thought of as resulting from the effect of rotation of the left end section at constant (non-rotating) left-end forces, combined with the effect of a modification of the global components of left-end forces by changes that would arise during rotation of these forces. Since the rotation  $d\varphi_a$  is infinitesimal, counterclockwise rotation of the horizontal force contributes by  $-X_{ab}d\varphi_a$  to the vertical component while counterclockwise rotation of the vertical force contributes by  $Z_{ab}d\varphi_a$  to the horizontal component. Using the formalism of equation (28), this decomposition can be described by

$$\begin{pmatrix} z_b - z_a \\ x_a - x_b \\ 1 \end{pmatrix} d\varphi_a = \mathbf{G} \begin{pmatrix} Z_{ab} \\ -X_{ab} \\ 0 \end{pmatrix} d\varphi_a + \mathbf{G}_r \begin{pmatrix} 0 \\ 0 \\ 1 \end{pmatrix} d\varphi_a \quad (31)$$

Cancelling  $d\varphi_a$  and regrouping the terms, we find out that the third column of  $\mathbf{G}_r$  could be evaluated by summing the column  $(z_b - z_a, x_a - x_b, 1)^T$ , the first column of  $\mathbf{G}$  multiplied by  $-Z_{ab}$ , and the second column of  $\mathbf{G}$  multiplied by  $X_{ab}$ . We do not even have to evaluate this expression, because what is actually needed is the third column of  $-\mathbf{G}^{-1}\mathbf{G}_r$ , and from (31) multiplied

from the left by  $\mathbf{G}^{-1}$  we can deduce that

$$-\mathbf{G}^{-1}\mathbf{G}_r \begin{pmatrix} 0 \\ 0 \\ 1 \end{pmatrix} = \mathbf{G}^{-1} \begin{pmatrix} z_a - z_b \\ x_b - x_a \\ -1 \end{pmatrix} + \begin{pmatrix} Z_{ab} \\ -X_{ab} \\ 0 \end{pmatrix} \quad (32)$$

The left-hand side is the third column of  $-\mathbf{G}^{-1}\mathbf{G}_r$ , i.e., of the upper left  $3 \times 3$  block of the element stiffness matrix, and the right-hand side provides a rule for its evaluation: Take the column  $(Z_{ab}, -X_{ab}, 0)^T$  and add a linear combination of the columns of  $\mathbf{G}^{-1}$  with coefficients  $z_a - z_b$ ,  $x_b - x_a$  and  $-1$ . All this is true in the absence of distributed external forces.

If nonzero external forces acting on the beam are prescribed, the first two columns of  $-\mathbf{G}^{-1}\mathbf{G}_r$  still correspond to the first two columns of  $\mathbf{G}^{-1}$  with reverted signs, but the third column of  $\mathbf{G}_r$  must be computed numerically by evaluating the effect of  $d\varphi_a$  on  $dx_b$ ,  $dz_b$  and  $d\varphi_b$ , and then multiplication from the left by  $-\mathbf{G}^{-1}$  leads to the third column of  $-\mathbf{G}^{-1}\mathbf{G}_r$ .

As already explained, matrices  $-\mathbf{G}^{-1}\mathbf{G}_r$  and  $\mathbf{G}^{-1}$  together fill the upper half of the  $6 \times 6$  stiffness matrix, i.e., the first three rows. Based on force equilibrium of the whole beam, it is easy to see that the fourth row is equal to minus the first row, and the fifth row is equal to minus the second row. The sixth row can be deduced from the moment equilibrium condition, which is somewhat more tricky. Differentiation of (A.36) leads to

$$\begin{aligned} dM_{ba} &= -dM_{ab} + dX_{ab}(z_b - z_a) + X_{ab}(dz_b - dz_a) - dZ_{ab}(x_b - x_a) + \\ &- Z_{ab}(dx_b - dx_a) + dM_p(L) \end{aligned} \quad (33)$$

In the absence of distributed external loads,  $M_p(L)$  vanishes and its change  $dM_p(L)$  as well, and the formula can be translated into a prescription for the sixth row of the element stiffness matrix: Initialize by  $(Z_{ab}, -X_{ab}, 0, -Z_{ab}, X_{ab}, 0)$ , add the first row multiplied by  $z_b - z_a$  and the second row multiplied by  $x_a - x_b$ , and subtract the third row.

In the presence of external loads, the contribution of  $dM_p(L)$  must be added. From the algorithm in Section 3.3.2 it will be clear that the sensitivities of  $M_p$  at individual grid points (to be introduced in the next section) to infinitesimal changes  $dX_{ab}$ ,  $dZ_{ab}$ ,  $dM_{ab}$  and  $d\varphi_a$  must be computed anyway, because they affect the evaluation of  $d\varphi$  at individual grid points. When the solution process reaches the right end of the beam, these sensitivities evaluated for the last grid point represent the derivatives of  $M_p(L)$  with respect to the left-end generalized forces and to the left-end inclination (notice that changes of the left-end coordinates have no effect on  $M_p$ ). The derivatives

with respect to the left-end generalized forces are then used as three coefficients that multiply the first, second and third row of the stiffness matrix in order to obtain the contribution of distributed loads to the last row of the stiffness matrix. The fourth coefficient, i.e., the derivative of  $M_p(L)$  with respect to  $\varphi_a$ , is simply added to the stiffness entry in the third column of the last row, i.e., to  $K_{63}$ .

### 3.2. Finite difference scheme

Recall that the governing differential equations to be solved are described by (A.43)–(A.45) for the Reissner model and by (A.83)–(A.84) and (A.87) for the Ziegler model. The spatial derivatives of unknown functions will be replaced by suitable finite difference approximations. Interestingly, for both models, the equations that describe the spatial derivatives of  $x_s$  and  $z_s$  have right-hand sides that can be evaluated exclusively from  $\varphi$ , and the equation that describes the spatial derivative of  $\varphi$  has a right-hand side that can be evaluated exclusively from  $x_s$  and  $z_s$ . Consequently, we can use central differences for the approximation of the first derivatives while keeping the algorithm explicit. Let us divide the interval  $[0, L]$  into  $N$  equally sized segments of length  $\Delta\xi = L/N$ , and define the coordinates of grid points

$$\xi_i = i \Delta\xi, \quad i = 0, 1, 2, \dots, N \quad (34)$$

and midpoints

$$\xi_{i-1/2} = (i - 1/2) \Delta\xi, \quad i = 1, 2, \dots, N \quad (35)$$

If the governing equations are presented in the symbolic form

$$x'_s = f_x(\varphi) \quad (36)$$

$$z'_s = f_z(\varphi) \quad (37)$$

$$\varphi' = f_\varphi(x_s, z_s) \quad (38)$$

then their finite difference approximations are

$$\frac{x_i - x_{i-1}}{\Delta\xi} = f_x(\varphi_{i-1/2}), \quad i = 1, 2, \dots, N \quad (39)$$

$$\frac{z_i - z_{i-1}}{\Delta\xi} = f_z(\varphi_{i-1/2}), \quad i = 1, 2, \dots, N \quad (40)$$

$$\frac{\varphi_{i+1/2} - \varphi_{i-1/2}}{\Delta\xi} = f_\varphi(x_i, z_i), \quad i = 1, 2, \dots, N - 1 \quad (41)$$

where  $x_i$  and  $z_i$  are numerical values of functions  $x_s$  and  $z_s$  at the grid points, and  $\varphi_{i-1/2}$  are numerical values of function  $\varphi$  at the midpoints. To

initiate the algorithm,  $x_0$  and  $z_0$  are set to the values  $x_a$  and  $z_a$  equal to the current coordinates of the left end centroid, and  $\varphi_{1/2}$  is evaluated from the given  $\varphi_0 = \varphi_a$  by adopting a forward Euler formula

$$\frac{\varphi_{1/2} - \varphi_0}{\Delta\xi/2} = f_\varphi(x_0, z_0) \quad (42)$$

for the first half-step. In a similar fashion, the value of  $\varphi_N$  at the end of the interval is calculated from a backward Euler formula

$$\frac{\varphi_N - \varphi_{N-1/2}}{\Delta\xi/2} = f_\varphi(x_N, z_N) \quad (43)$$

adopted for the last half-step. Even this formula is explicit, because the values of  $x_N$  and  $z_N$  are already known and  $\varphi_N$  is not needed on the right-hand side.

Functions  $f_x$ ,  $f_z$  and  $f_\varphi$  could be directly replaced by the complicated expressions on the right-hand sides of (A.43)–(A.45), or of (A.83)–(A.84) and (A.87). However, for a clean numerical implementation, it is preferable to evaluate individual terms sequentially, which allows for easier physical interpretation of the intermediate results. For example, for the Reissner model we get back to the individual equations from which (A.43)–(A.45) was composed, noting that the differential character of the equations comes from (6), while the remaining relations (4) and (7)–(9) are algebraic.

### 3.3. Reissner model

#### 3.3.1. Evaluation of right-end generalized coordinates

The basic algorithm needed for the implementation is the numerical evaluation of function  $\mathbf{g}(\mathbf{f}_a, \mathbf{r}_a)$ , which takes as input the left-end generalized forces  $\mathbf{f}_a = (X_{ab}, Z_{ab}, M_{ab})^T$  and left-end generalized coordinates  $\mathbf{r}_a = (x_a, z_a, \varphi_a)^T$  and provides as output the right-end generalized coordinates  $\mathbf{r}_b = (x_b, z_b, \varphi_b)^T$ .

If the beam is loaded by distributed forces, it is useful to precompute and store the partial load resultants

$$P_{r,1/2} = \frac{p_r(0) + p_r(\xi_{1/2})}{4} \Delta\xi \quad (44)$$

$$P_{r,i+1/2} = P_{r,i-1/2} + \frac{p_r(\xi_{i-1/2}) + p_r(\xi_{i+1/2})}{2} \Delta\xi, \quad i = 1, 2, \dots, N-1 \quad (45)$$

$$P_{r,N} = P_{r,N-1/2} + \frac{p_r(L) + p_r(\xi_{N-1/2})}{4} \Delta\xi \quad (46)$$

where  $r \in \{x, z\}$ . If the distributed forces are fixed, this needs be done only once, even before the incremental-iterative solution of the beam structure is started. If the distributed forces are increased proportionally to a load factor which is varied in each step, the pre-computed partial resultants represent reference values and in the algorithm below need to be multiplied by the load factor. It is worth noting that one could easily incorporate concentrated forces acting on the beam as well. Their global components would be simply added to  $P_{x,i+1/2}$  and  $P_{z,i+1/2}$  when the corresponding coordinate  $\xi_{i+1/2}$  becomes for the first time greater than the coordinate of the section at which the concentrated force is applied.

The algorithm for evaluation of  $\mathbf{g}(\mathbf{f}_a, \mathbf{r}_a)$  can be organized as follows:

1. Set initial values  $x_0 = x_a$ ,  $z_0 = z_a$ ,  $\varphi_0 = \varphi_a \equiv \Phi_a - \alpha_{ab}$ ,  $M_{p0} = 0$ , and  $M_0 = -M_{ab}$ .
2. For  $i = 1, 2, \dots, N$  evaluate

$$\varphi_{i-1/2} = \varphi_{i-1} + \frac{M_{i-1}}{EI} \frac{\Delta\xi}{2} \quad (47)$$

$$c = \cos \varphi_{i-1/2} \quad (48)$$

$$s = \sin \varphi_{i-1/2} \quad (49)$$

$$N_{i-1/2} = -c (X_{ab} + P_{x,i-1/2}) + s (Z_{ab} + P_{z,i-1/2}) \quad (50)$$

$$Q_{i-1/2} = -s (X_{ab} + P_{x,i-1/2}) - c (Z_{ab} + P_{z,i-1/2}) \quad (51)$$

$$\varepsilon_{i-1/2} = \frac{N_{i-1/2}}{EA} \quad (52)$$

$$\gamma_{i-1/2} = \frac{Q_{i-1/2}}{GA_s} \quad (53)$$

$$\Delta x = (c(1 + \varepsilon_{i-1/2}) + s\gamma_{i-1/2}) \Delta\xi \quad (54)$$

$$\Delta z = (c\gamma_{i-1/2} - s(1 + \varepsilon_{i-1/2})) \Delta\xi \quad (55)$$

$$x_i = x_{i-1} + \Delta x \quad (56)$$

$$z_i = z_{i-1} + \Delta z \quad (57)$$

$$M_{pi} = M_{p,i-1} - m(\xi_{i-1/2}) \Delta\xi + P_{x,i-1/2} \Delta z - P_{z,i-1/2} \Delta x \quad (58)$$

$$M_i = -M_{ab} + X_{ab}(z_i - z_a) - Z_{ab}(x_i - x_a) + M_{pi} \quad (59)$$

$$\varphi_i = \varphi_{i-1/2} + \frac{M_i}{EI} \frac{\Delta\xi}{2} \quad (60)$$

3. The resulting coordinates and inclination at the right end are  $x_b = x_N$ ,  $z_b = z_N$  and  $\varphi_b = \varphi_N$ . It is also useful to provide  $M_{pN}$  as part of the output.



Notice that  $c$  and  $s$  are values of the cosine and sine of angle  $\varphi_{i-1/2}$ , which change in each cycle but for brevity are not denoted by subscript  $i - 1/2$ . These auxiliary variables are also used in the loop that computes the Jacobi matrix, to be presented in the next section.

It is also worth noting that the present algorithm could be adjusted to accommodate the Kirchhoff beam model as a limit case with an infinite shear stiffness, resulting into a zero shear measure  $\gamma$ . Evaluation of  $Q_{i-1/2}$  in (51) and of  $\gamma_{i-1/2}$  in (53) would be skipped, and the terms with  $\gamma_{i-1/2}$  would be deleted from (54)–(55). Instead of introducing branches in the algorithm or writing a special code for the Kirchhoff case, it is even simpler to implement the operation in (53) as multiplication of the shear force by the sectional shear compliance  $C_s \equiv 1/GA_s$ , and to consider this compliance (instead of the stiffness  $GA_s$ ) as one of the input parameters describing the beam. The results for a Kirchhoff beam can then be obtained without touching the algorithm, simply by using  $C_s = 0$  on input. One can even go further and implement the fraction in (50) as the multiplication of the normal force by the sectional axial compliance  $C_a \equiv 1/EA$ , and the fractions in (47) and (60) as the multiplication of the bending moment by the sectional flexural compliance  $C_b \equiv 1/EI$ . Then, by using  $C_s = 0$  and  $C_a = 0$ , we obtain the Euler elastica, and by using also  $C_b = 0$ , we obtain a perfectly rigid beam. In general, the sectional properties can vary along the beam, and by setting  $C_s = 0$ ,  $C_a = 0$  and  $C_b = 0$  in certain numerical segments, we can easily combine flexible parts of the beam with rigid segments, e.g., near the joints, which might be useful to obtain a more realistic frame model for 3D-printed beam assemblies, as demonstrated in [21]. Only minor changes in the code are needed, consisting in the added control of the values of sectional compliances at individual grid points. The actual sequence of operations in the algorithm does not need to be changed.

### 3.3.2. Evaluation of Jacobi matrix

The Jacobi matrix is needed for the iterative evaluation of the generalized end forces on the element level as well as for the construction of the element stiffness matrix. The entries of the Jacobi matrix  $\mathbf{G}(\mathbf{f}_a, \mathbf{r}_a)$  are evaluated numerically using the linearized form of the computational scheme. Simultaneously, the derivatives  $\partial \mathbf{g}(\mathbf{f}_a, \mathbf{r}_a) / \partial \varphi_a$  are computed, since they are needed to construct the element stiffness matrix, as described in Section 3.1.2.

Suppose that the input values  $X_{ab}$ ,  $Z_{ab}$  and  $M_{ab}$  are changed by infinitesimal increments  $dX_{ab}$ ,  $dZ_{ab}$  and  $dM_{ab}$ . Linearization of equations (47)–(60) around the currently considered solution leads to the following algorithm:

1. Set one of the values of  $dX_{ab}$ ,  $dZ_{ab}$ ,  $dM_{ab}$  or  $d\varphi_a$  to 1 and the others

to 0, depending on which column of the extended Jacobi matrix is to be computed (the fourth column now corresponds to  $\partial \mathbf{g} / \partial \varphi_a$ ). Set initial values  $dx_0 = 0$ ,  $dz_0 = 0$ ,  $dM_{p0} = 0$ , and  $dM_0 = -dM_{ab}$ .

2. For  $i = 1, 2, \dots, N$  evaluate

$$d\varphi_{i-1/2} = d\varphi_{i-1} + \frac{dM_{i-1}}{EI} \frac{\Delta\xi}{2} \quad (61)$$

$$dN_{i-1/2} = -c dX_{ab} + s dZ_{ab} - Q_{i-1/2} d\varphi_{i-1/2} \quad (62)$$

$$dQ_{i-1/2} = -s dX_{ab} - c dZ_{ab} + N_{i-1/2} d\varphi_{i-1/2} \quad (63)$$

$$d\varepsilon_{i-1/2} = \frac{dN_{i-1/2}}{EA} \quad (64)$$

$$d\gamma_{i-1/2} = \frac{dQ_{i-1/2}}{GA_s} \quad (65)$$

$$d\Delta x = (c d\varepsilon_{i-1/2} + s d\gamma_{i-1/2} - (s(1 + \varepsilon_{i-1/2}) - c\gamma_{i-1/2}) d\varphi_{i-1/2}) \Delta\xi \quad (66)$$

$$d\Delta z = (c d\gamma_{i-1/2} - s d\varepsilon_{i-1/2} - (s\gamma_{i-1/2} + c(1 + \varepsilon_{i-1/2})) d\varphi_{i-1/2}) \Delta\xi \quad (67)$$

$$dx_i = dx_{i-1} + d\Delta x \quad (68)$$

$$dz_i = dz_{i-1} + d\Delta z \quad (69)$$

$$dM_{pi} = dM_{p,i-1} + P_{x,i-1/2} d\Delta z - P_{z,i-1/2} d\Delta x \quad (70)$$

$$dM_i = -dM_{ab} + dX_{ab}(z_i - z_a) + X_{ab} dz_i - dZ_{ab}(x_i - x_a) - Z_{ab} dx_i + dM_{pi} \quad (71)$$

$$d\varphi_i = d\varphi_{i-1/2} + \frac{dM_i}{EI} \frac{\Delta\xi}{2} \quad (72)$$

For  $dX_{ab} = 1$  and  $dZ_{ab} = dM_{ab} = d\varphi_a = 0$ , the final values of  $dx_N$ ,  $dz_N$  and  $d\varphi_N$  obtained by running this algorithm represent entries of the first column of the Jacobi matrix  $\mathbf{G}$ . In a similar fashion, an evaluation working with  $dX_{ab} = 0$ ,  $dZ_{ab} = 1$  and  $dM_{ab} = d\varphi_a = 0$  provides the second column, and an evaluation working with  $dX_{ab} = dZ_{ab} = d\varphi_a = 0$  and  $dM_{ab} = 1$  provides the third column. In practice, all three columns of the Jacobi matrix are computed in a single loop, along with the value of function  $\mathbf{g}$ . Also, in the presence of distributed loads, the algorithm is simultaneously executed with  $dX_{ab} = dZ_{ab} = dM_{ab} = 0$  and  $d\varphi_a = 1$ , leading to the third column of matrix  $\mathbf{G}_r$ , which contains the derivatives  $\partial \mathbf{g} / \partial \varphi_a$ . Everything is done within a single loop, and so the values of internal forces  $N_{i-1/2}$  and  $Q_{i-1/2}$  and deformation variables  $\varepsilon_{i-1/2}$  and  $\gamma_{i-1/2}$  are those calculated by the algorithm presented in Section 3.3.1, and  $c$  and  $s$  have the meaning of the cosine and sine of  $\varphi_{i-1/2}$ . Since they are reused, the corresponding formulas are not repeated here. All variables with identifiers starting by the symbol “d” are in fact arrays with 3 or 4 values, depending on whether we compute

the columns of  $\mathbf{G}$  only, or also the third column of  $\mathbf{G}_r$ .

### 3.4. Ziegler model

#### 3.4.1. Iterative scheme for shear angle evaluation

For evaluation of internal forces at midpoint  $\xi_{i-1/2}$ , we need the midpoint shear angle  $\chi_{i-1/2}$ , which is defined implicitly as the solution of nonlinear equation (A.80), in which  $P_1$  is replaced by  $X_{ab} + P_x$ ,  $P_2$  by  $Z_{ab} + P_z$ ,  $\varphi$  by  $\varphi_{i-1/2}$  and  $\chi$  by  $\chi_{i-1/2}$ . Since the midpoint rotation  $\varphi_{i-1/2}$  can be evaluated independently of  $\chi_{i-1/2}$ , and the forces  $X_{ab}$ ,  $Z_{ab}$ ,  $P_x$  and  $P_z$  are given (in the context of this algorithm), this equation can be presented in the form

$$F(\chi_{i-1/2}) = 0 \quad (73)$$

where function

$$F(\chi) = GA_s\chi - \left(1 + \frac{f_N(\chi)}{EA}\right) f_Q(\chi) \quad (74)$$

is defined using auxiliary functions

$$f_N(\chi) = -(X_{ab} + P_x) \cos(\varphi_{i-1/2} - \chi) + (Z_{ab} + P_z) \sin(\varphi_{i-1/2} - \chi) \quad (75)$$

$$f_Q(\chi) = -(X_{ab} + P_x) \sin(\varphi_{i-1/2} - \chi) - (Z_{ab} + P_z) \cos(\varphi_{i-1/2} - \chi) \quad (76)$$

It is easy to see that  $df_N/d\chi = f_Q$  and  $df_Q/d\chi = -f_N$ , and so

$$F'(\chi) \equiv \frac{dF(\chi)}{d\chi} = GA_s + f_N(\chi) \left(1 + \frac{f_N(\chi)}{EA}\right) - \frac{f_Q^2(\chi)}{EA} \quad (77)$$

The iterative process typically starts from the first guess  $\chi^{(0)} = \chi_{i-3/2} =$  shear angle at the midpoint of the previous spatial segment (for  $i = 1$ , the initial guess is set to zero). Improved approximations are calculated using the recursive formula

$$\chi^{(j)} = \chi^{(j-1)} - \frac{F(\chi^{(j-1)})}{F'(\chi^{(j-1)})}, \quad j = 1, 2, \dots \quad (78)$$

and it is terminated when the absolute value of  $F(\chi^{(j)})$  becomes sufficiently small. The converged value  $\chi^{(j)}$  is then used as  $\chi_{i-1/2}$ , and we can proceed to the evaluation of other quantities at the midstep. In fact, the values of  $f_N(\chi^{(j)})$  and  $f_Q(\chi^{(j)})$  calculated during the evaluation of  $F(\chi^{(j)})$  are directly the internal forces at midstep,  $\tilde{N}_{i-1/2}$  and  $Q_{i-1/2}^*$ , and the already evaluated expression  $1 + f_N(\chi^{(j)})/EA$  is the centerline stretch,  $\lambda_{i-1/2}$ , from which the corresponding increments of primary variables  $x_s$  and  $z_s$  can be evaluated.

### 3.4.2. Evaluation of right-end displacements and rotation

If the beam is loaded by distributed forces, it is useful to precompute and store the partial load resultants using the same formulae (44)–(46) as for the Reissner model. This is done only once. Afterwards, the following algorithm is invoked.

1. Set initial values  $x_0 = x_a$ ,  $z_0 = z_a$ ,  $\varphi_0 = \varphi_a \equiv \Phi_a - \alpha_{ab}$ ,  $M_{p0} = 0$  and  $M_0 = -M_{ab}$ . Set the tolerance  $\epsilon_{tol}$  of the internal iteration loop.
2. For  $i = 1, 2, \dots, N$  evaluate

$$\varphi_{i-1/2} = \varphi_{i-1} + \frac{M_{i-1}}{EI} \frac{\Delta\xi}{2} \quad (79)$$

$$\chi_{i-1/2} = \chi_{i-3/2} \quad (\text{or } \chi_{i-1/2} = 0 \text{ if } i = 1) \quad (80)$$

repeat:

$$c = \cos(\varphi_{i-1/2} - \chi_{i-1/2}) \quad (81)$$

$$s = \sin(\varphi_{i-1/2} - \chi_{i-1/2}) \quad (82)$$

$$\tilde{N}_{i-1/2} = -c(X_{ab} + P_{x,i-1/2}) + s(Z_{ab} + P_{z,i-1/2}) \quad (83)$$

$$Q_{i-1/2}^* = -s(X_{ab} + P_{x,i-1/2}) - c(Z_{ab} + P_{z,i-1/2}) \quad (84)$$

$$\lambda_{i-1/2} = 1 + \frac{\tilde{N}_{i-1/2}}{EA} \quad (85)$$

$$F = GA_s \chi_{i-1/2} - \lambda_{i-1/2} Q_{i-1/2}^* \quad (86)$$

if  $|F| < \epsilon_{tol}$  then go to (89)

$$F' = GA_s + \lambda_{i-1/2} \tilde{N}_{i-1/2} - \frac{Q_{i-1/2}^{*2}}{EA} \quad (87)$$

$$\chi_{i-1/2} = \chi_{i-1/2} - F/F' \quad (88)$$

until the maximum number of internal iterations is exceeded (report failure)

$$\Delta x = c \lambda_{i-1/2} \Delta\xi \quad (89)$$

$$\Delta z = -s \lambda_{i-1/2} \Delta\xi \quad (90)$$

$$x_i = x_{i-1} + \Delta x \quad (91)$$

$$z_i = z_{i-1} + \Delta z \quad (92)$$

$$M_{pi} = M_{p,i-1} - m(\xi_{i-1/2}) \Delta\xi + P_{x,i-1/2} \Delta z - P_{z,i-1/2} \Delta x \quad (93)$$

$$M_i = -M_{ab} + X_{ab}(z_i - z_a) - Z_{ab}(x_i - x_a) + M_{pi} \quad (94)$$

$$\varphi_i = \varphi_{i-1/2} + \frac{M_i}{EI} \frac{\Delta\xi}{2} \quad (95)$$

3. The resulting coordinates and rotation at the right end are  $x_b = x_N$ ,  $z_b = z_N$  and  $\varphi_b = \varphi_N$ . It is also useful to provide  $M_{pN}$  as part of the output.

### 3.4.3. Evaluation of Jacobi matrix

Suppose that the input values  $X_{ab}$ ,  $Z_{ab}$  and  $M_{ab}$  are changed by infinitesimal increments  $dX_{ab}$ ,  $dZ_{ab}$  and  $dM_{ab}$ . Linearization of the algorithm described in Section 3.4.2 around the currently considered solution is straightforward, but special attention needs to be paid to the implicitly defined shear angle  $\chi_{i-1/2}$ , which is evaluated in the internal iterative loop (81)–(88). The converged solution is affected by changes in  $X_{ab}$  and  $Z_{ab}$ , and also by the change in  $\varphi_{i-1/2}$ . Consistent linearization of condition  $F = 0$  leads to

$$GA_s d\chi_{i-1/2} - Q_{i-1/2}^* d\lambda_{i-1/2} - \lambda_{i-1/2}^* dQ_{i-1/2}^* = 0 \quad (96)$$

in which

$$d\lambda_{i-1/2} = \frac{d\tilde{N}_{i-1/2}}{EA} \quad (97)$$

$$d\tilde{N}_{i-1/2} = -c dX_{ab} + s dZ_{ab} - Q_{i-1/2}^* (d\varphi_{i-1/2} - d\chi_{i-1/2}) \quad (98)$$

$$dQ_{i-1/2}^* = -s dX_{ab} - c dZ_{ab} + \tilde{N}_{i-1/2} (d\varphi_{i-1/2} - d\chi_{i-1/2}) \quad (99)$$

Substituting (97)–(99) into (96) and solving for  $d\chi_{i-1/2}$ , we get

$$d\chi_{i-1/2} = \frac{\left(-c Q_{i-1/2}^*/EA - s \lambda_{i-1/2}\right) dX_a + \left(s Q_{i-1/2}^*/EA - c \lambda_{i-1/2}\right) dZ_a + \left(\lambda_{i-1/2} \tilde{N}_{i-1/2} - Q_{i-1/2}^{*2}/EA\right) d\varphi_a}{GA_s + \lambda_{i-1/2} \tilde{N}_{i-1/2} - Q_{i-1/2}^{*2}/EA} \quad (100)$$

In combination with the linearized form of the explicit expressions (79) and (89)–(95), the following algorithm is obtained:

1. Set one of the values of  $dX_{ab}$ ,  $dZ_{ab}$ ,  $dM_{ab}$  or  $d\varphi_a$  to 1 and the others to 0, depending on which column of the Jacobi matrix is to be computed. Set initial values  $dx_0 = 0$ ,  $dz_0 = 0$ ,  $dM_{p0} = 0$ , and  $dM_0 = -dM_{ab}$ .

2. For  $i = 1, 2, \dots, N$  evaluate

$$d\varphi_{i-1/2} = d\varphi_{i-1} + \frac{dM_{i-1}}{EI} \frac{\Delta\xi}{2} \quad (101)$$

$$c = \cos(\varphi_{i-1/2} - \chi_{i-1/2}) \quad (102)$$

$$s = \sin(\varphi_{i-1/2} - \chi_{i-1/2}) \quad (103)$$

$$d\chi_{i-1/2} = \frac{\left(-\frac{cQ_{i-1/2}^*}{EA} - s\lambda_{i-1/2}\right) dX_a + \left(\frac{sQ_{i-1/2}^*}{EA} - c\lambda_{i-1/2}\right) dZ_a + \left(\lambda_{i-1/2}\tilde{N}_{i-1/2} - \frac{Q_{i-1/2}^{*2}}{EA}\right) d\varphi_a}{GA_s + \lambda_{i-1/2}\tilde{N}_{i-1/2} - \frac{Q_{i-1/2}^{*2}}{EA}} \quad (104)$$

$$d\tilde{N}_{i-1/2} = -c dX_{ab} + s dZ_{ab} - Q_{i-1/2}^* (d\varphi_{i-1/2} - d\chi_{i-1/2}) \quad (105)$$

$$d\lambda_{i-1/2} = \frac{d\tilde{N}_{i-1/2}}{EA} \quad (106)$$

$$d\Delta x = (c d\lambda_{i-1/2} - s\lambda_{i-1/2} (d\varphi_{i-1/2} - d\chi_{i-1/2})) \Delta\xi \quad (107)$$

$$d\Delta z = (-s d\lambda_{i-1/2} - c\lambda_{i-1/2} (d\varphi_{i-1/2} - d\chi_{i-1/2})) \Delta\xi \quad (108)$$

$$dx_i = dx_{i-1} + d\Delta x \quad (109)$$

$$dz_i = dz_{i-1} + d\Delta z \quad (110)$$

$$dM_{pi} = dM_{p,i-1} + P_{x,i-1/2} d\Delta z - P_{z,i-1/2} d\Delta x \quad (111)$$

$$dM_i = -dM_{ab} + dX_{ab} (z_i - z_a) + X_{ab} dz_i - dZ_{ab} (x_i - x_a) - Z_{ab} dx_i + dM_{pi} \quad (112)$$

$$d\varphi_i = d\varphi_{i-1/2} + \frac{dM_i}{EI} \frac{\Delta\xi}{2} \quad (113)$$

3. For  $dX_{ab} = 1$  and  $dZ_{ab} = dM_{ab} = d\varphi_0 = 0$ , the final values of  $dx_N$ ,  $dz_N$  and  $d\varphi_N$  obtained by running this algorithm represent the entries of the first column of the Jacobi matrix  $\mathbf{G}$ . In a similar fashion, an evaluation working with  $dX_{ab} = 0$ ,  $dZ_{ab} = 1$  and  $dM_{ab} = d\varphi_a = 0$  provides the second column, and an evaluation working with  $dX_{ab} = dZ_{ab} = d\varphi_a = 0$  and  $dM_{ab} = 1$  provides the third column. In practice, all three columns of the Jacobi matrix are computed in a single loop, along with the value of function  $\mathbf{g}$ . Also, in the presence of distributed loads, the algorithm is simultaneously executed with  $dX_{ab} = dZ_{ab} = dM_{ab} = 0$  and  $d\varphi_a = 1$ , leading to the third column of matrix  $\mathbf{G}_r$ .

#### 4. Examples—bending with shear

The accuracy and efficiency of the proposed numerical schemes will be tested using several benchmark examples. Unless stated otherwise, the ex-

amples consider an isotropic linear elastic material with Young’s modulus denoted as  $E$  and Poisson’s ratio set to  $\nu = 0.25$ , which leads to the shear modulus  $G = E/(2(1 + \nu)) = 0.4E$ . The cross section is taken as rectangular, characterized by width  $b$  and depth  $h$ , with the shear reduction factor set to the usual value of  $5/6$  (even though Cowper’s approach[30] would lead to a slightly different value), which provides the sectional shear stiffness  $GA_s = 5GA/6 = EA/3$  and dimensionless parameter  $\Gamma \equiv GA_s/EA = 1/3$ . Furthermore, the bending stiffness can be expressed as  $EI = Ebh^3/12 = EAh^2/12$ . A characteristic length (typically the beam span) is denoted as  $L$ . To eliminate the dependence of the results on the specific choice of input parameters, we normalize forces by  $EI/L^2$  and lengths by  $L$ , which means that moments are normalized by  $EI/L$ . Since the Poisson ratio  $\nu = 0.25$  is considered as fixed, there remains a single dimensionless input parameter  $h/L$ , i.e., the depth-to-span ratio. The resulting deflections and other displacements are normalized by  $L$ .

#### 4.1. Simply supported beam, concentrated force

Numerical examples start from a simply supported beam of span  $L$ , loaded by a vertical concentrated force  $F$  at midspan, as indicated in Fig. 3. The prescribed load is converted into the dimensionless factor  $FL^2/(EI)$ , and the resulting midspan deflection is reported in its dimensionless form  $w/L$ . To explore the effect of the beam shape (slenderness), let us analyze three cases with  $h/L=1/4, 1/8$ , and  $1/16$ .

##### 4.1.1. Deformed shapes

The problem is symmetric with respect to the vertical axis (except for the nonsymmetry in the horizontal support, which could be easily eliminated), and so it could be solved using only one half of the beam discretized by one single element. Equivalent results are obtained by discretizing the whole beam into two equally sized elements, each of them of length  $L/2$ , divided into a certain number of integration segments. In this case, the concentrated force is applied at the node located at the midspan. Fig. 3 shows the deformed centerlines for the three considered geometries (depth-to-span ratios) at the same normalized load level, obtained using the Reissner model (dotted, dashed and dash-dotted curves). Since the load is normalized by the bending stiffness, the largest deflection is found for the stocky beam with  $h/L = 1/4$ , for which the relative importance of the shear deformation is higher than for more slender beams. A kink in the middle of the deflection curve is clearly visible in this case. As illustrated by Fig. 4, the sectional inclination  $\varphi$  varies smoothly and remains differentiable, because

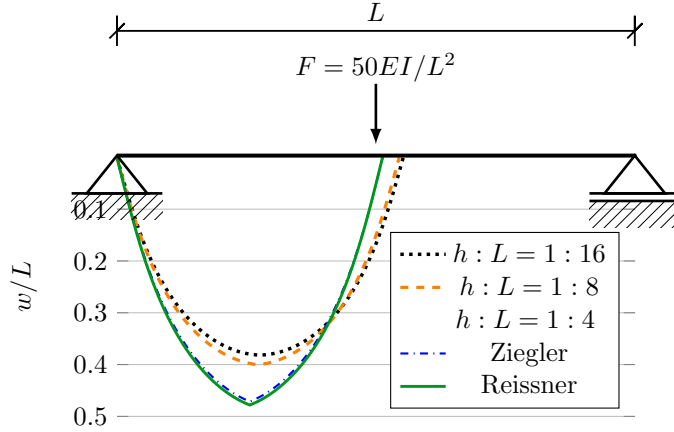


Figure 3: Simply supported beam loaded by a concentrated force  $F$  at midspan: undeformed beam with supports and loading, and deformed centerline shapes at load level  $F = 50EI/L^2$  evaluated for beams of various depth-to-span ratios using the Reissner model and, for  $h : L = 1 : 4$ , also the Ziegler model

its derivative is the curvature, proportional to the bending moment, which is continuous. However, the slope of the centerline differs from  $\varphi$  by the shear angle  $\chi$ , which is related to the shear force and has a jump at the section under the applied concentrated force. Such a jump is present in all the cases, but it is less conspicuous for slender beams. For comparison, Fig. 3 also contains the deformed centerline obtained with the Ziegler model for the stocky beam with  $h/L = 1/4$  (solid curve). The difference between the Reissner and Ziegler models is seen to be very small in this example. For slender beams, it is almost negligible, and only the Reissner curves are shown.

#### 4.1.2. Load-displacement diagrams

Load-displacement diagrams covering a wide range up to midspan deflections close to one half of the span are plotted in Fig. 5. In part (a), the Reissner model is used and the results are presented for various depth-to-span ratios. The curve obtained in the limit of  $h/L \rightarrow 0$  is also included. This limit corresponds to the Euler model with zero axial deformation and zero shear deformation, enforced by using  $1/EA = 0$  and  $1/GA_s = 0$ , as described at the end of Section 3.3.1). For a slender beam with  $h/L = 1/16$ , the full Reissner model with axial and shear flexibility included gives only a slight increase of the deflection (dashed curve). As expected, the increase is much more pronounced for stocky beams, especially for the depth-to-span



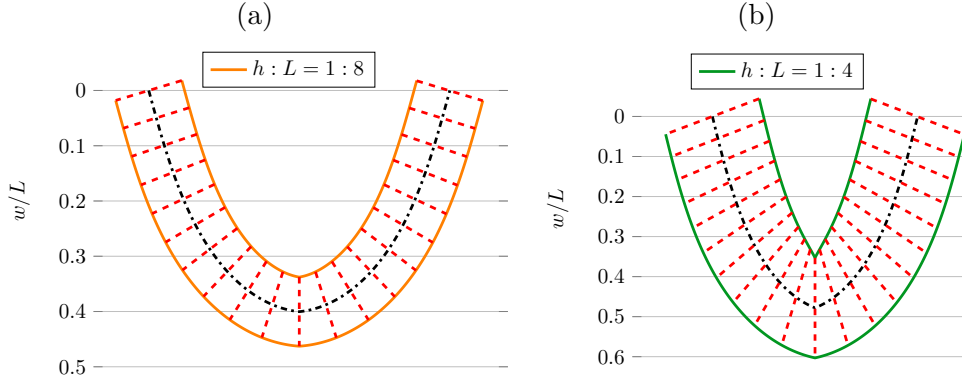


Figure 4: Simply supported beam loaded by a concentrated force  $F$  at midspan: the deformed centerline and selected sections at load level  $F = 50 EI/L^2$  evaluated for beams of depth-to-span ratios 1:8 and 1:4 using the Reissner model.

ratio 1:4 (black curve).

The load-displacement curves plotted in Fig. 5a correspond to the Reissner model. It turns out that for slender beams, such as those with  $h/L = 1/16$  and  $1/8$ , the Ziegler model gives load-displacement curves that are graphically indistinguishable from those for the Reissner formulation. Visible differences are found for the stocky beam with  $h/L = 1/4$ , as seen in Fig. 5b. In addition to the full Reissner and Ziegler formulations, the curves are plotted for the Kirchhoff model with shear deformation neglected but axial deformation still taken into account, and also for the Euler model, which neglects both effects. The comparison shows that, in the highly non-linear range, both effects (axial and shear deformation) significantly increase the resulting deflections. The Reissner formulation leads to slightly larger deflections than the Ziegler model.

#### 4.1.3. Initial stiffness

According to the linear Timoshenko theory, the normalized mid-span deflection would be

$$\frac{w}{L} = \frac{FL^2}{48EI} + \frac{F}{4GA_s} = \frac{FL^2}{EI} \frac{1}{48} \left( 1 + \frac{3h^2}{L^2} \right) \quad (114)$$

This means that the dimensionless structural stiffness (initial slope of the load-displacement diagram that links the normalized deflection to the normalized force  $FL^2/EI$ ) is 48 for the Kirchhoff beam with no shear deformation, while for the Timoshenko beam it is reduced by the factor  $1 + 3h^2/L^2$ ,

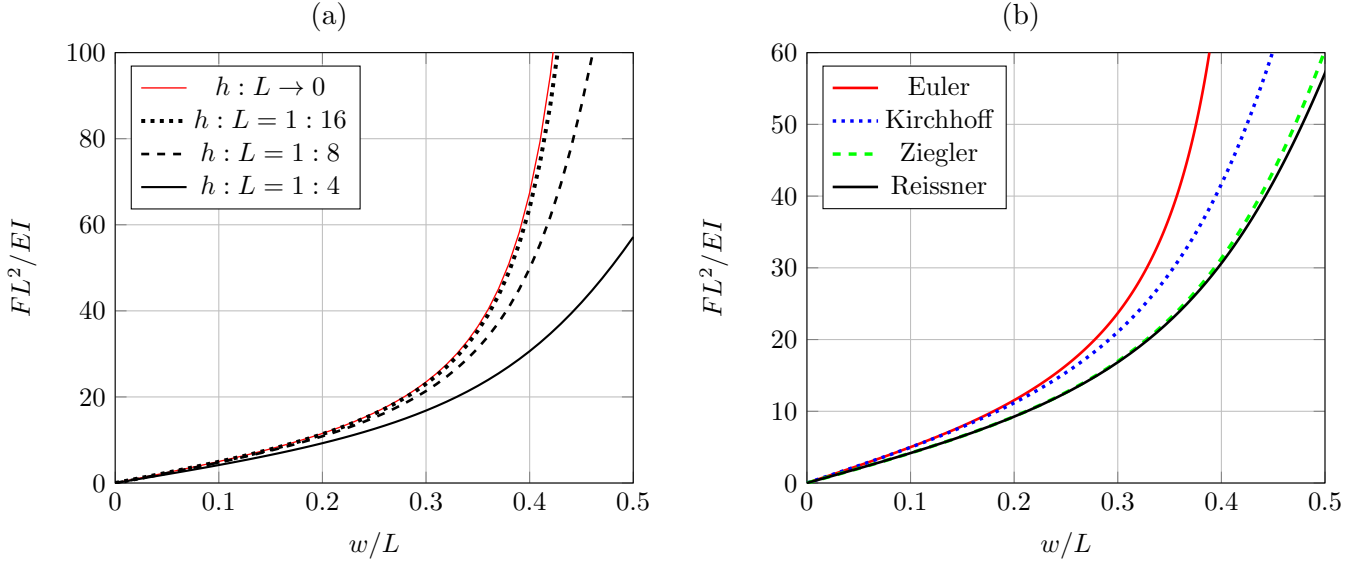


Figure 5: Simply supported beam loaded by a concentrated force at midspan: normalized load-displacement curves (a) for the Reissner model and various depth-to-span ratios, (b) for depth-to-span ratio 1:4 and various models

leading to the dimensionless stiffnesses of 40.421, 45.851 and 47.444 for  $h/L = 1/4, 1/8$  and  $1/16$ , respectively.

The initial slope of the load-displacement curves from Fig. 5 corresponds to the stiffness of the Timoshenko beam. This gives us an opportunity to evaluate the numerical error induced by discretization in space. The initial structural stiffness extracted from the tangent stiffness matrix calculated for the initial undeformed state is reported in Table 1. The results have been evaluated for the Reissner model, but the initial stiffness computed for the Ziegler model would be exactly the same. As the number of integration segments is increased, the numerically obtained value quickly converges to the theoretical limit, no matter whether the beam is slender ( $h/L = 1/16$ ) or stocky ( $h/L = 1/4$ ). Already for 8 integration segments per element, the error is below 1 %, and it decreases in proportion to the square of the segment size.

#### 4.1.4. Discretization error in nonlinear range

A comparable (even slightly lower) error level is observed in the nonlinear range, as documented in Table 2, which shows the deflection obtained for a fixed, rather high load. The reported deflection values refer to the state

Table 1: Simply supported beam loaded by a concentrated force at midspan and discretized by two elements: convergence of the initial structural stiffness

number of segments	$h/L = 1/4$		$h/L = 1/16$	
	$FL^3/(wEI)$	error [%]	$FL^3/(wEI)$	error [%]
2	36.5714	9.52	42.2268	11.0
4	39.3846	2.56	46.0225	3.00
8	40.1569	0.65	47.0805	0.77
16	40.3547	0.16	47.3526	0.19
32	40.4044	0.041	47.4211	0.048
64	40.4169	0.010	47.4383	0.012
128	40.4200	0.0026	47.4426	0.0030
analytical	40.4210		47.4440	

after convergence of global equilibrium iterations (with a sufficiently strict convergence criterion), but they still depend on the spatial resolution. For both models, Reissner and Ziegler, the relative accuracy is virtually the same when the same spatial resolution is used, even though the reference values obtained in the limit are slightly different. The “converged” reference values have been computed by using 10,000 integration segments, which is overkill (six-digit accuracy would be obtained already with 500 segments). Let us emphasize that the refinement of the grid inside the element does not affect the global number of degrees of freedom, which remains equal to 6 in the present example (can be reduced to 3 if symmetry is exploited, and even to 2 if the midspan deflection is prescribed instead of the midspan force).

It is worth noting that the quadratic nature of the convergence rate (as the spatial grid is refined) is independent of the slenderness and, for a given number of integration points, the error for a slender beam is only slightly larger than for a stocky beam. This indicates that the present formulation does not suffer from shear locking. For an extremely slender beam with  $h/L = 1/64$ , the relative error in the mid-span deflection at load level  $F = 50 EI/L^2$  computed using 16 integration segments per element would be 0.19 %, which is almost the same as for  $h/L = 1/16$  (the converged value of  $w/L$  is 0.375826 while the approximate value for 16 segments is 0.376523).

In fact, the algorithm is, after a minor change, applicable to the Kirchhoff formulation that neglects shear, without losing the nice convergence properties. The minimal modification is to replace formula (53) by  $\gamma_{i-1/2} = 0$  and formula (65) by  $d\gamma_{i-1/2} = 0$ ; see also the discussion at the end of Sec-

Table 2: Simply supported beam loaded by a concentrated force at midspan and discretized by two elements: convergence of the mid-span displacement obtained for a given load  $F = 50 EI/L^2$  as the number of integration segments per element is increased

number of segments	Reissner model				Ziegler model			
	$h/L = 1/4$		$h/L = 1/16$		$h/L = 1/4$		$h/L = 1/16$	
	$w/L$	error [%]	$w/L$	error [%]	$w/L$	error [%]	$w/L$	error [%]
2	0.506722	5.99	0.420842	10.28	0.499423	5.98	0.420817	10.28
4	0.486911	1.84	0.392607	2.88	0.479664	1.79	0.392582	2.88
8	0.480365	0.48	0.384369	0.72	0.473427	0.46	0.384345	0.72
16	0.478647	0.12	0.382297	0.18	0.471796	0.12	0.382273	0.18
32	0.478214	0.030	0.381779	0.045	0.471385	0.029	0.381755	0.045
64	0.478105	0.007	0.381650	0.011	0.471282	0.007	0.381626	0.011
128	0.478078	0.0019	0.381617	0.0028	0.471256	0.0019	0.381594	0.0028
converged	0.478069		0.381607		0.471247		0.381583	

tion 3.3.1.

#### 4.1.5. Comparison with results from the literature

Owing to symmetry, the simply supported beam considered here is equivalent to a cantilever of span  $L/2$ , loaded at its free end by a vertical force  $F/2$ . For this elementary problem, certain reference solutions are available. Analytical solutions were derived for the Reissner model with neglected axial compliance by Batista [31], and the results presented in Table 3 of [31] apply to our beam with  $F = 20$ ,  $L = 2$  and  $EI = 10$ . The results were reported for selected values of the shear stiffness  $GA_s$  and for an extremely high axial stiffness (we use  $EA = 10^8$ ). Table 3 compares the analytical values from [31] with our numerical results for values of  $GA_s = 5 \times 10^{20}$  and 500.

force, $F$	20	20	200	200
shear stiffness, $GA_s$	$5 \times 10^{20}$	500	$5 \times 10^{20}$	500
exact, Batista [31]	0.301720774	0.317813874		
Lyritsakis et al. [32]	0.3017206	0.3178137	0.8106113	0.8536137
present, converged	0.3017208	0.3178139	0.8106099	0.8539632
present, 16 segments	0.3022736	0.3183590	0.8123628	0.8554802
relative error	0.18 %	0.17 %	0.22 %	0.18 %

Table 3: Deflections reported in the literature and computed with the present approach using the Reissner model

Numerical solutions of the same problem were reported in Table 1 of Lyritsakis et al. [32], who used a hybrid beam element based on nonlinear programming. In addition to the moderate load level for which the deflection is about 30 % of the cantilever length (corresponding to 15 % of the span of a simply supported beam), they considered also 10 times higher load, in our notation  $F = 200$ . The comparison in Table 3 indicates that, for load  $F = 20$ , our converged values of maximum deflection (obtained with a sufficiently high number of integration segments) perfectly agree with the analytical solutions from [31] as well as with the numerical values from [32]. For the high load  $F = 200$ , there is a small difference between our converged results and the values reported in [32], which were obtained using an integration scheme with 6 quadrature points and probably were not fully converged. Our converged result for  $F = 200$  and extremely high  $GA_s$  agrees in the first 6 digits with the exact solution 0.8106090 reported in [32]. For simulations with 16 integration segments, the relative errors reported in the last row of Table 3 are around 0.2 %, even for the highly deformed state induced by force  $F = 200$ .

## 4.2. Clamped beam, uniformly distributed load

### 4.2.1. Initial stiffness

The second simple benchmark is a beam of span  $L$  clamped at both ends and subjected to a uniformly distributed vertical load of intensity  $f$ . According to the linear Timoshenko theory, the normalized mid-span deflection would be

$$\frac{w}{L} = \frac{fL^3}{384EI} + \frac{fL}{8GA_s} = \frac{fL^3}{EI} \frac{1}{384} \left( 1 + \frac{12h^2}{L^2} \right) \quad (115)$$

Here, the load is characterized by the dimensionless variable  $fL^3/EI$ , and we still assume a rectangular cross section and Poisson's ratio  $\nu = 0.25$ .

For a Kirchhoff beam, the dimensionless stiffness would be 384. The effect of shear reduces it by the factor  $(1 + 12h^2/L^2)$ . Let us consider two cases with the depth-to-span ratio 1/6 and 1/12. The corresponding dimensionless structural stiffnesses are 288 and 354.4615, respectively.

Since the applied load is distributed and applied at the beam level, the initial stiffness cannot be directly deduced from the structural stiffness. A simple check consists in calculating the mid-span deflection caused by a very small load. For  $h/L = 1/6$ , we set the dimensionless load to  $fL^3/EI = 0.0288$ . The deflection expected for a linear model is then  $w/L = 10^{-4}$ . Indeed, the numerical simulation with two elements and 10,000 integration segments per element leads to a deflection that differs from this

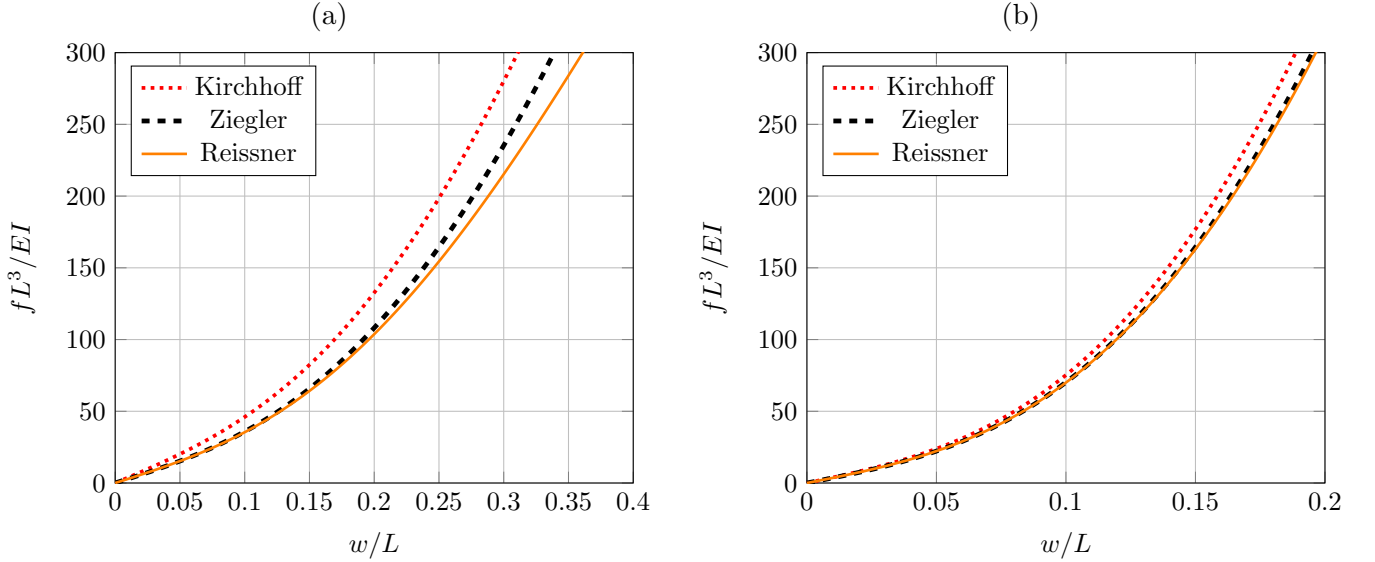


Figure 6: Clamped beam subjected to uniform load of intensity  $f$ : normalized load-displacement curves (a) for depth-to-span ratio 1:6, (b) for depth-to-span ratio 1:12

value approximately by  $2 \cdot 10^{-11}$ , so the relative error is only 0.00002 % (in fact, this difference is probably caused by the nonlinearity). With 16, 32 and 64 integration segments, the relative errors are found to be 0.59 %, 0.15 % and 0.037 %, respectively, which confirms the expected quadratic dependence of the error on the segment size. Similar results are obtained for the beam with  $h/L = 1/12$ , where a dimensionless load  $fL^3/EI = 0.03544615$  is expected to lead to  $w/L = 10^{-4}$ . Numerical simulations with 16, 32 and 64 integration segments lead to relative errors of 0.72 %, 0.18 % and 0.045 %, respectively. The relative errors do not depend on the adopted formulation (Reissner or Ziegler).

#### 4.2.2. Load-displacement diagrams

The complete load-displacement diagrams that cover the highly nonlinear range are plotted in Fig. 6. In addition to the results obtained with the Reissner and Ziegler models, the figure includes the response of the Kirchhoff model, i.e., a beam model without shear but with axial extensibility. For the beam clamped at both ends, the axially inextensible Euler model would not allow any changes of the centerline and thus cannot be used (except if the changes are considered as infinitesimal, in which case both Euler and Kirchhoff formulations reduce to the standard linear beam theory). For the

stocky beam with  $h/L = 1/6$ , the difference between the Reissner and Ziegler formulations is more pronounced than in the previous example of a simply supported beam; see also Fig. 7 with the deflected shapes that correspond to the load level of  $f = 300 EI/L^3$ . For  $h/L = 1/12$ , both formulations yield very similar results, but the effect of shear is still non-negligible.

#### 4.2.3. Discretization error in nonlinear range

As an additional convergence check, Table 4 shows the dimensionless mid-span deflections obtained numerically for the dimensionless load  $fL^3/EI = 300$  and the corresponding relative errors. The calculations are done for the stocky beam with  $h/L = 1/6$ , for which the Reissner and Ziegler models yield different results. The results indicate that, for the same computational grid, the Reissner model gives typically a lower error than the Ziegler

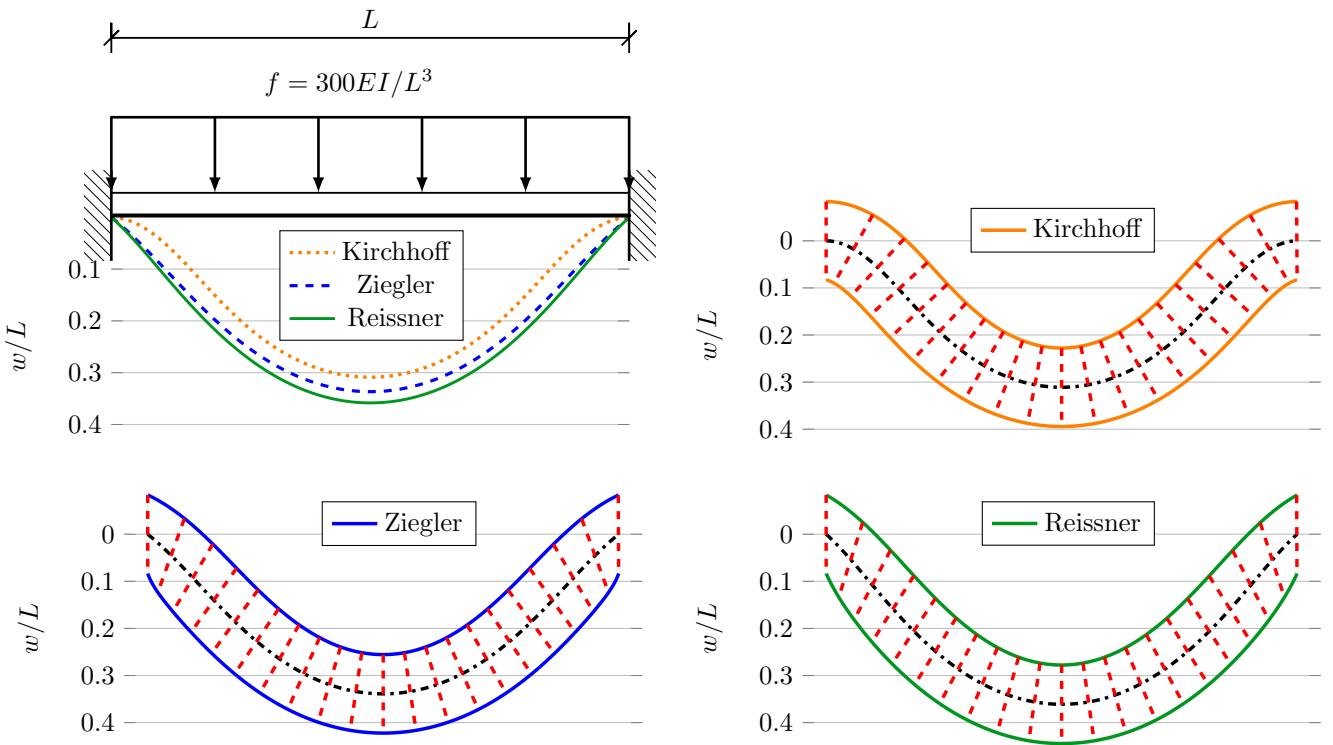


Figure 7: Clamped beam subjected to uniform load of intensity  $f$ : initial shape, boundary conditions and loading, and the deformed centerlines and rotated sections at load level  $f = 300 EI/L^3$  obtained for depth-to-span ratio 1:6 using various models

model. Asymptotically (for fine grids), the error is for both models proportional to the square of the segment size. Some irregularity is observed for very coarse grids (2 or 4 segments per element), for which the Reissner model yields surprisingly high accuracy.

Table 4: Clamped beam with  $h/L = 1/6$  subjected to uniform load: convergence of the mid-span displacement obtained for a given load  $f = 300 EI/L^3$  as the number of integration segments per element is increased

number of segments	Reissner model		Ziegler model	
	$w/L$	error [%]	$w/L$	error [%]
2	0.365004	1.09	0.355012	4.75
4	0.362076	0.28	0.344361	1.61
8	0.361554	0.13	0.340514	0.48
16	0.361227	0.045	0.339328	0.13
32	0.361109	0.012	0.339011	0.032
64	0.361077	0.0032	0.338930	0.0078
128	0.3610683	0.0008	0.3389102	0.0019
256	0.3610662	0.0002	0.3389052	0.0005
converged	0.3610655		0.3389035	

#### 4.2.4. Internal forces

The adopted numerical scheme provides good approximations not only for kinematic variables such as displacements and rotations, but also for static variables such as internal forces. To demonstrate that and to illustrate the difference between the two considered formulations, Fig. 8 shows the distribution of the normal forces and shear force along the beam, plotted as functions of the initial distance from the left end,  $\xi$ . For both internal forces, solid curves correspond to the almost converged solution and dashed curves to the results obtained with just 8 integration segments at load level  $f = 300 EI/L^3$ . The forces are normalized by  $EI/L^2$ . The values of internal forces are plotted at midpoints of integration segments and, for the accurate solution with 32 segments per element, connected by straight lines. Even for 8 segments per element, the error is seen to be quite small. On the other hand, the differences between the Reissner (blue) and Ziegler (red) internal forces are substantial, especially near the supports, where the shear distortion is high (cf. Fig. 7). Recall that for the Reissner model, the normal force is interpreted as the component perpendicular to the section, while for the Ziegler model it is aligned with the tangent to the centerline).



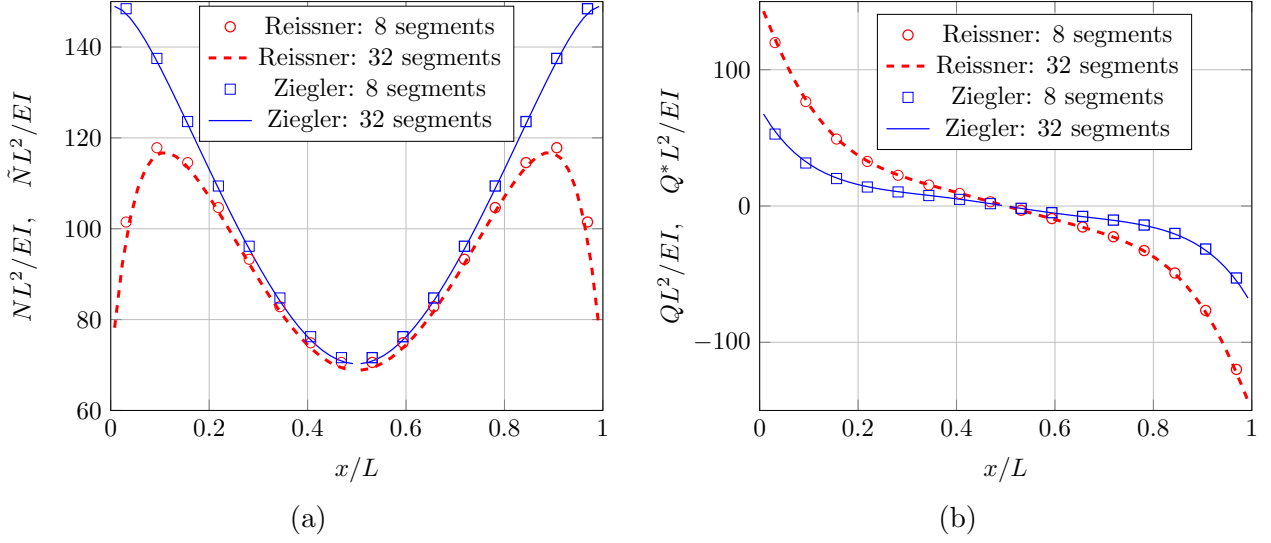


Figure 8: Clamped beam subjected to uniform load of intensity  $f$ : distribution of (a) normal force and (b) shear force at load level  $f = 300 EI/L^3$  obtained for depth-to-span ratio 1:6 with the Reissner (red) or Ziegler (blue) model using 8 (points) or 32 (curves) integration segments per element

#### 4.3. Cantilever, uniformly distributed external moment

The previous example demonstrated that the effect of distributed forces is properly captured by the developed algorithm. Let us now investigate a somewhat artificial yet interesting case of a cantilever subjected to an externally applied distributed moment of uniform intensity  $m$ . The beam can be expected to fold into a spiral-like shape. Since the normal and shear forces vanish (independently of the specific definition), shear plays no role here and the centerline does not change its length. The problem can be treated analytically (see Appendix B), which provides a reference solution for the numerical simulations.

Numerical simulation of the cantilever with uniform distributed moment load can be done using a single beam element, which means that only three global unknowns are introduced. The intensity of the moment load is increased in 60 equal steps up to the final value of  $m = 30EI/L^2$ , which corresponds to the dimensionless parameter  $\mu = \sqrt{30/\pi} \approx 3.0902$ . The left end of the beam, placed at the origin, is clamped, and the right end, placed at  $(x, z) = (L, 0)$ , is free. Fig. 9a shows the numerically evaluated position of the cantilever tip after each step (filled circles) and the analytical solution parametrically described by (B.9)–(B.10). The final deformed shape is

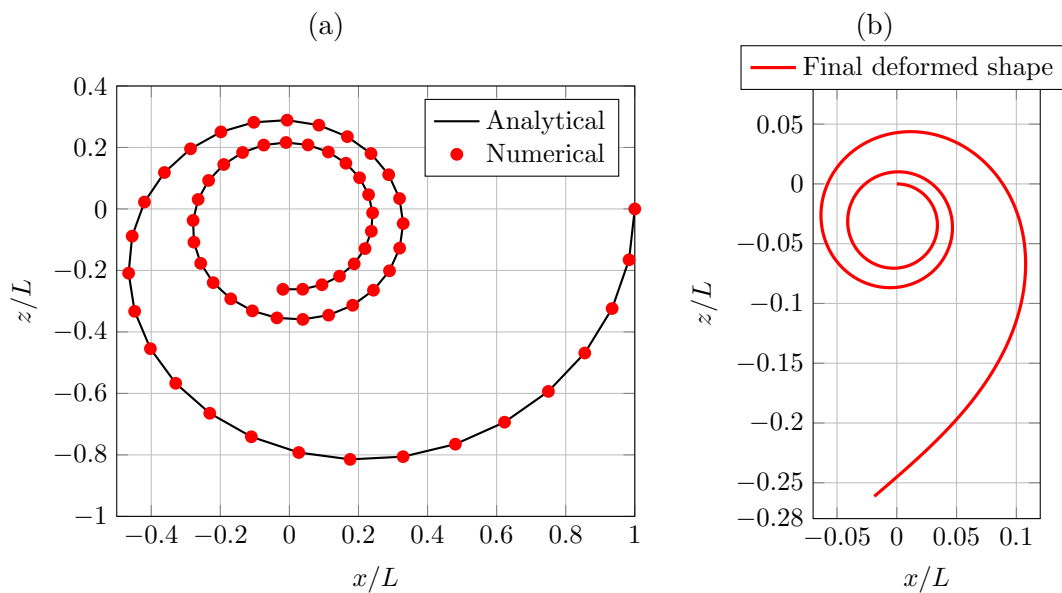


Figure 9: Cantilever loaded by a uniformly distributed external moment: (a) the trajectory of the cantilever tip when the applied moment intensity increases from 0 to  $30 EI/L^2$ , (b) the final deformed shape

depicted in Fig. 9b. The numerical solution divided the element into 500 integration segments, and the calculated position of the cantilever tip after the last step deviates from the exact value by  $6.14 \cdot 10^{-6}$  times the beam length  $L$ .

#### 4.4. Shallow frame dome with snap-through

For certain applications, it is useful to provide optional connections of beam elements to the joints by rigid arms. For instance, if the nodes of the beam model are placed at the centers of the actual physical joints of finite dimensions, the theoretical length of the beam element measured as the distance between nodes is longer than the actual beam segment that has the given cross sectional characteristics, and the response of the model may become more flexible than the actual behavior. As demonstrated by Di Re et al.[21], the experimental load-displacement curve measured on a 3D-printed spatial lattice structure by Jamshidian et al.[33] can be numerically reproduced by a beam finite element model only if the end portions of the beams are made stiffer than the regular part. Therefore, Di Re et al.[21] developed three-dimensional corotational finite elements with rigid joint offsets.

Among other examples, they tested their formulation on a shallow frame dome, previously studied by Battini et al.[34]. Even though the considered structure is spatial, its symmetry makes it possible to perform the analysis using a planar beam element. The dimensions and supports are shown in Fig. 10a, with  $L_h = 15$  m and  $H = 0.6$  m. The cross section is rectangular, of width  $b = 0.14$  m and depth  $h = 0.17$  m, and the material is considered as linear elastic, with Young's modulus  $E = 10$  MPa and Poisson's ratio  $\nu = 0.3$ . The frame dome consists of three beams located in vertical planes rotated with respect to each other by  $120^\circ$ . If it is loaded by a vertical force at the common joint, the resulting diagram exhibits snap-through.

To get a reference solution, Di Re et al.[21] analyzed the problem using the SAP2000 FE package, with each beam divided into 64 finite elements. Selected points in the load-displacement diagram obtained in this way are shown as filled circles in Fig. 10b. The solid curve corresponds to our simulation with a single beam element divided into 100 integration segments. Very good agreement is observed. The largest deviation in terms of force is 0.004 N, while the snap-through force is 7.7484 N.

Subsequently, Di Re et al.[21] studied the effect of increased stiffness near the beam ends. They considered rigid offsets over 10 % or 20 % of the total beam length near both ends. For the present comparison, we use the results obtained with their MLD-RB; see the squares and diamonds in Fig. 10. The continuous curves represent our simulations with a single beam element divided into 100 integration segments. The agreement is again very good. The largest deviation for 10 % offsets is 0.0255 N, while the snap-through force is 8.2827 N, and the largest deviation for 20 % offsets is 0.00256 N, while the snap-through force is 8.9288 N.

Modeling of rigid offsets within the present framework requires only minimal adjustments. It is sufficient to set the flexibilities  $1/EI$ ,  $1/EA$ , and  $1/GA_s$  to zero in all integration segments that are located in the rigid part of the beam. This is indeed the simplest modification that requires minimal programming effort. Of course, computational efficiency can be increased by handling all rigid integration segments at once and skipping all unnecessary operations. The modified code replaces the algorithmic steps (47)–(60) of the Reissner model or (79)–(95) of the Ziegler model by

$$x_i = x_{i-1} + \Delta\xi_R \cos \varphi_{i-1} \quad (116)$$

$$z_i = z_{i-1} - \Delta\xi_R \sin \varphi_{i-1} \quad (117)$$

$$\varphi_i = \varphi_{i-1} \quad (118)$$

where  $\Delta\xi_R$  is the total length of the rigid segment (which does not need to

be subdivided into integration segments of the same size as the flexible part of the beam). In the presence of loads acting directly on the beam, it is also necessary to evaluate

$$M_{pi} = M_{p,i-1} - (m(\xi_{i-1/2}) + P_{x,i-1/2} \cos \varphi_{i-1} + P_{z,i-1/2} \sin \varphi_{i-1}) \Delta \xi_R \quad (119)$$

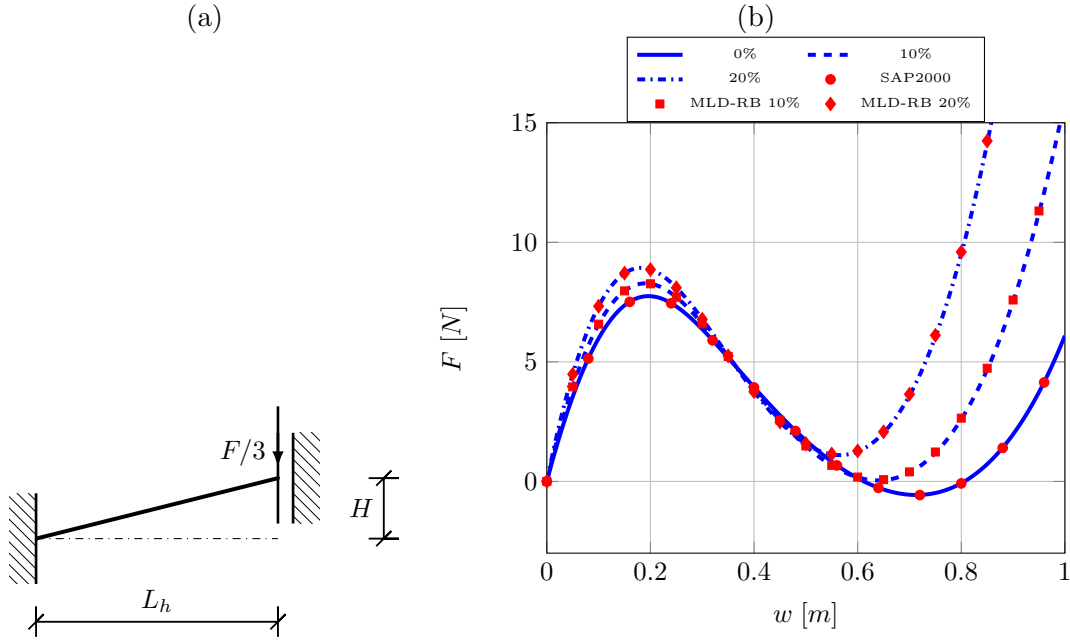


Figure 10: Shallow frame dome: (a) loading and supports of a planar beam that replaces 1/3 of the spatial structure, (b) load-displacement diagrams for standard beams (solid) and beams with 10 % (dashed) and 20 % (dash-dotted) rigid offsets; the isolated points correspond to the results obtained by Di Re et al. using SAP2000 (circles) and their MLD-RB elements with offsets modeled as rigid beams (squares and diamonds)

## 5. Examples—stability

When developing the theoretical background in Section 2 and Appendix A, we presented two alternative versions of sectional equations—one corresponding to the widely used Reissner approach (Appendix A.1.2 and Appendix A.1) and the other that can be referred to as the Ziegler approach (Section Appendix A.2.2 and Appendix A.2). In the geometrically linear approximation, both reduce to the same standard Timoshenko theory. Also, when the shear deformation is neglected, or the sectional shear stiffness is set

to infinity, they both reduce to what we consider as the Kirchhoff beam, even for large rotations. However, differences in the load-displacement curves are observed when large shear distortions occur; see e.g. Fig. 6a.

Let us now investigate how the choice of a specific formulation of the sectional equations affects the buckling load of an axially loaded straight column. In Appendix C it is shown that the Reissner model is closely related to the Haringx approach to stability analysis[25], while the Ziegler model is an extension of the Engesser approach[26] to the case of axially compressible columns. Analytical expressions for the critical load derived for both formulations in Appendix C can be used here as additional benchmarks for the numerical procedures.

### 5.1. Critical state of a clamped column in compression

The ability of the developed formulations to capture compressive buckling will be demonstrated using the example of a column clamped on both sides, with depth-to-span ratio 1:6 or 1:12. These are the same geometries as used in the example in Section 4.2, but this time the lateral loading is replaced by an axial displacement that is prescribed at one of the supports and initially induces uniform compression. When the reaction force reaches the critical level, buckling is expected. The critical state can be numerically detected by analyzing the eigenvalues of the structural stiffness matrix.

The described loading could in principle be simulated by a single beam element, but then there would be no global unknowns and the bifurcation would occur at the element level. To capture it using traditional techniques, let us model the column using two equally sized beam elements. The central node has three degrees of freedom that are used as global unknowns.

Since the column is clamped at both ends, its buckling length is  $L_b = L/2$ , and the corresponding slenderness can be evaluated as  $s = L_b/i_y = L/(2\sqrt{I/A}) = \sqrt{3}L/h^2$ . Therefore, the square of slenderness is  $s^2 = 3L^2/h^2 = 108$  for the stocky case with  $h/L = 1/6$ , and  $s^2 = 432$  for the more slender column with  $h/L = 1/12$ . Moreover, the sectional stiffness ratio  $\Gamma = GA_s = EA = 1/3$ , provided that the Poisson ratio is set to 0.25 and the shear reduction coefficient is considered as  $A_s/A = 5/6$  for a rectangular section. Substituting into the analytical formulae derived in the previous section, we obtain the critical loads that correspond to various models. The results are summarized in Table 5 in the form of critical strains, defined as  $\varepsilon_{crit} = P_{crit}/EA$ . The case of an incompressible model without shear corresponds to the standard Euler solution, with critical stress  $\sigma_{crit} = P_E/A = E\pi^2/s^2$ . The critical strain is formally obtained as the critical stress divided by the elastic modulus, i.e., it is given by  $\pi^2/s^2$ , but

should not be interpreted as the actual strain at the onset of buckling, since this particular model assumes that the centerline does not change its length. For the Reissner model, the critical strain  $\varepsilon_{Rc} = \sigma_{Rc}/E$  is evaluated using formula (C.44) with  $E$  removed. For the Ziegler model, formula (C.75) directly provides the critical strain  $\varepsilon_{Zc}$ .

Table 5: Critical strains (compressive) for the clamped-clamped column according to various models (numerical results computed with 2 beam elements and 32 integration segments per element, based on linear interpolation of the lowest eigenvalue over a prescribed strain increment of 0.001)

	$h/L = 1/6$		$h/L = 1/12$	
	analytical	numerical	analytical	numerical
Euler	0.091385	0.091312	0.022846	0.022828
Kirchhoff ( $GA_s \rightarrow \infty$ )	0.101700	0.101643	0.023394	0.023374
Reissner ( $GA_s/EA = 1/3$ )	0.078926	0.078870	0.021888	0.021871
Ziegler ( $GA_s/EA = 1/3$ )	0.077770	0.077716	0.021859	0.021842

In numerical simulations, the column is discretized into two beam elements of length 0.5 that connect nodes 1 and 2 and nodes 2 and 3. Node 3 is fixed (including rotation), and the axial displacement at node 1 is increased in each incremental step by 0.001. For the fundamental solution, the axial displacement at node 2 increases in each step by 0.0005 while the lateral displacement and the rotation remain zero. The structural tangent stiffness is in this example diagonal, and the diagonal stiffness coefficient that corresponds to the lateral displacement at node 2 gradually decreases. The simulation is terminated when this coefficient becomes negative, and the critical strain is evaluated by linear interpolation in the last incremental step. For instance, for the Reissner model and  $h/L = 1/6$  (simulated with  $EI = 1$ ,  $EA = 432$  and  $GA_s = 144$ ), analyzed using 32 integration segments per element, the diagonal stiffness coefficient is equal to 1.817168 after step 78 and to  $-0.270419$  after step 79, and the critical strain is estimated as  $0.078 + 0.001 \times 1.817168 / (1.817168 + 0.270419) = 0.078870$ . This is only by 0.07 % below the analytical value of 0.078926. For a simulation with 8 integration segments per element, the numerically estimated critical strain would be 0.078037, which is by 1.1 % below the analytical value.

Using a similar procedure, the numerical estimates have been constructed for the other cases (using 32 integration segments per element), and the results are reported in Table 5. Excellent agreement with the analytical results is observed. For the incompressible model without shear (Euler),

the numerical solution cannot be driven by a prescribed axial displacement. Instead, the applied axial load is incremented, and the critical “strain” is evaluated as the critical load divided by the real physical stiffness  $EA$ , while the numerical simulation is performed with the axial sectional flexibility  $1/EA$  set to zero.

### 5.2. Post-buckling response in compression

Numerical simulations make it possible not only to detect the critical state, but also to trace the bifurcated solution in the post-critical range. The resulting diagrams in Fig. 11 show the evolution of the axial and lateral displacement plotted against the loading force. We consider here a column clamped at both ends, with depth-to-length ratio  $h/L = 1/6$ , rectangular cross section, and sectional stiffness ratio  $GA_s/EA = 1/3$ . The corresponding slenderness is  $s = \sqrt{3}L/h \approx 10.392$ . The simulation has been done with 2 beam elements, each divided into 100 integration segments. In the graphs, the force is normalized by the axial sectional stiffness  $EA$ , and the displacements are normalized by the beam length  $L$ . The axial displacement  $u$  is taken at the loaded section and thus represents the axial shortening of the column. The lateral displacement  $w$  is taken at the computational node in the middle of the column. Before bifurcation, the bar is compressed uniformly and the normalized axial displacement,  $|u|/L$ , is equal to the normalized force,  $P/EA$ , since both represent the strain magnitude. The transversal displacement remains equal to zero.

The theoretical value of the critical strain at which the bifurcation is expected can be calculated using formula (C.44) or (C.75), depending on which model is used. Since the considered geometry and stiffness ratio correspond to the example in Section 5.1, the values of the critical strain can be found directly in Table 5. If the simulation is run without any perturbations, the solution will follow the unstable fundamental solution. To trigger the bifurcation, the solution is perturbed by a small lateral load applied at the computational node in the middle of the column. Once the equilibrium iteration converges, the perturbation load is removed and the equilibrium iteration continues. If this is done in a subcritical state, the final solution corresponds to the fundamental one, since this is the only solution at the given load level. However, if the load is supercritical, the process typically converges to one of the stable solutions on the bifurcated branch.

In this way, the equilibrium diagrams have been constructed for the Reissner and Ziegler models (for which the critical strains are 7.89 % and 7.78 %, respectively). Only small differences in the response are observed in

Fig. 11. For comparison, the response has also been traced using the Kirchhoff model, for which the critical strain of 10.2 % is substantially larger than for the models that take into account compliance in shear. At comparable displacement levels in the post-critical range, the Kirchhoff model also requires higher applied loads.

The deformed shapes in the post-critical range are visualized in Fig. 12, which shows not only the deformed centerline but also the inclination of selected cross sections, in order to demonstrate the role of shear. All the displayed shapes correspond to the state in which the axial displacement corresponds to one half of the initial column length (i.e.,  $|u|/L = 0.5$  in Fig. 11a). The shapes of the deformed centerline are similar for all three models, but the sectional inclinations obtained with the Kirchhoff model are different from those obtained with the models that account for shear, and the corresponding axial force is also different. The diagrams in Fig. 11 cover the numerical solution of the governing equations in a wide range, but extreme states with  $|u|/L$  above 0.66 are nonphysical, because of internal contact that would occur in the folded column.

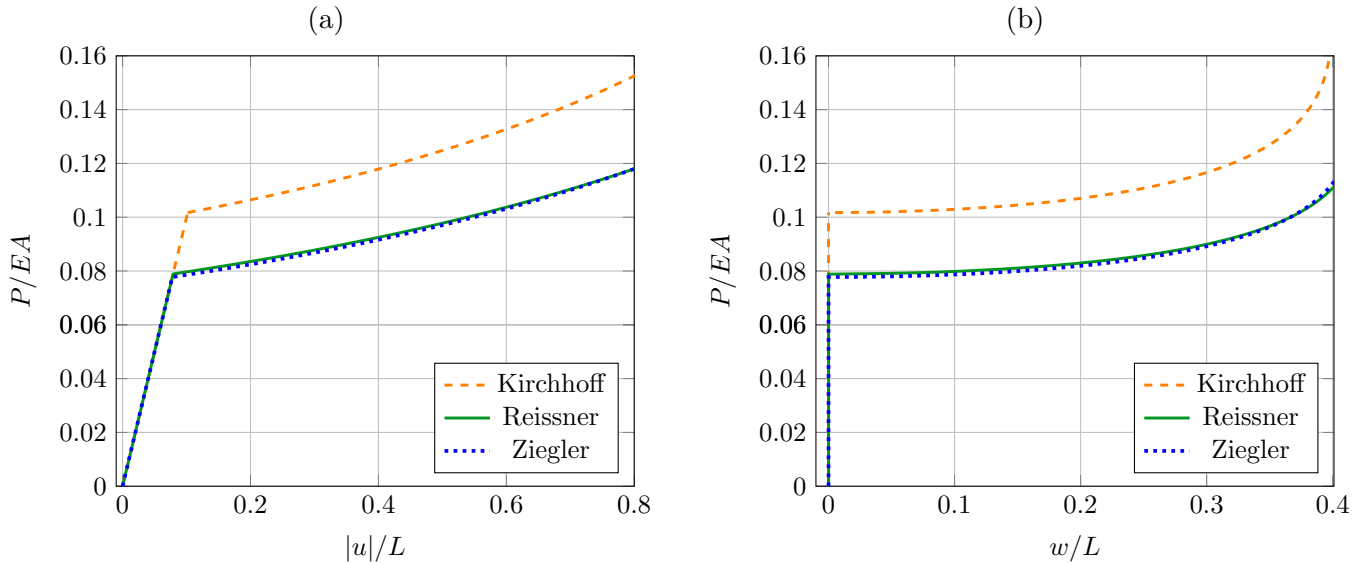


Figure 11: Load-displacement diagrams for a compressed column clamped at both ends: (a) axial displacement versus applied force, (b) lateral displacement versus applied force



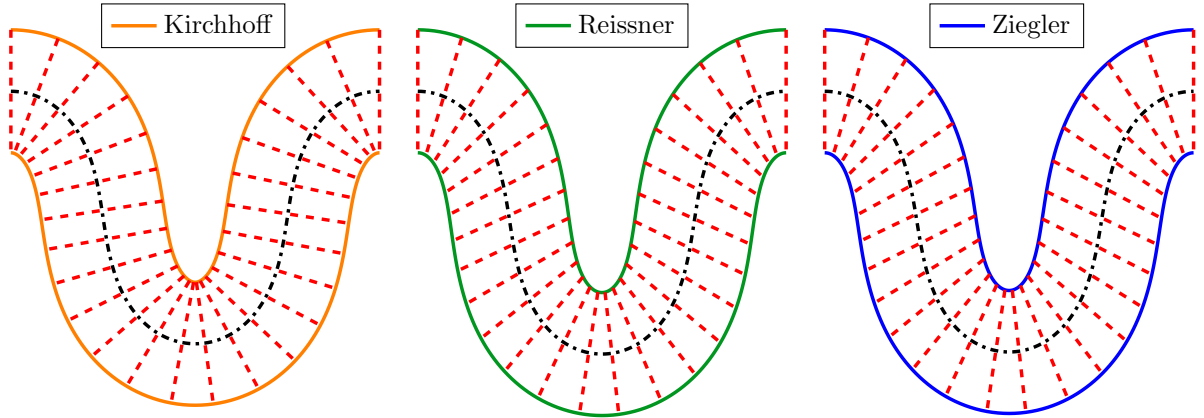


Figure 12: Deformed shapes in the post-critical state at  $|u|/L = 0.5$  obtained with various models

### 5.3. Critical state in tension

As shown in Appendix C.2.3, the Reissner model can lead to bifurcations in tension, and the analysis needs to be done separately for different types of supports. Therefore, illustrative numerical simulations of tensile bifurcations will be performed for the three combinations of boundary conditions analyzed in Appendix C.2.3.

First consider a bar of length  $L$  **clamped at one end** and loaded at the other (free) end by a force that induces axial tension. This problem always has a fundamental solution that corresponds to uniform stretching of the beam, with the axis remaining straight. According to the theoretical analysis, the fundamental solution can be expected to lose stability when a certain critical state is attained. The critical strain can be determined using formula (C.49) and its value depends on two dimensionless parameters: the sectional stiffness ratio  $\Gamma$  and the slenderness  $s$ . For a cantilever of length  $L$ , the slenderness needs to be evaluated using the buckling length  $L_b = 2L$ . If the section is rectangular, of depth  $h$ , we get

$$s = \frac{L_b}{\sqrt{I/A}} = \frac{2L}{\sqrt{h^2/12}} = 4\sqrt{3} \frac{L}{h} \quad (120)$$

Let us examine two depth-to-span ratios,  $h/L = 1/4$  and  $1/8$ , and three values of the stiffness ratio  $\Gamma$ , with  $\Gamma = 1/3$  characterizing a homogeneous rectangular section, and  $\Gamma = 0.1$  and  $0.01$  corresponding to sections with low and very low shear stiffness. The resulting analytical values of the critical

strain evaluated from (C.49) are compared with the numerically obtained values in Table 6.

The bar is modeled by 1 element with 32 integration segments. The difference between the numerical and analytical results in Table 6 is partly due to the linear interpolation of the lowest eigenvalue of the stiffness matrix over the step in which this eigenvalue changes its sign from positive to negative. The size of this step in terms of the prescribed strain increment has been fixed to 0.001. Refining the step (e.g., using the secant method for finding the root) could further reduce the error, even at a fixed number of integration segments. However, the agreement is excellent even without this improvement.

Table 6: Critical strains in tension for a bar of depth  $h$  and length  $L$  according to the Reissner model with various stiffness ratios  $\Gamma = GA_s/EA$  (numerical results are based on linear interpolation of the lowest eigenvalue over a prescribed strain increment of 0.001)

$GA_s/EA$	clamped at one end				clamped at both ends	
	$h/L = 1/4$		$h/L = 1/8$		$h/L = 1/6$	
	analytical	numerical	analytical	numerical	analytical	numerical
1/3	0.512537	0.512529	0.503192	0.503179	0.522385	0.522365
1/10	0.122744	0.122736	0.114636	0.114219	0.132805	0.132788
1/100	0.017513	0.017502	0.012664	0.012628	0.026976	0.026969

Next, let us look at a **simply supported bar**. The theoretical analysis indicates that, in this particular case, slenderness does not affect the critical strain given by formula (C.51). For  $\Gamma = 1/3, 0.1$  and  $0.01$ , the analytically evaluated critical strain  $\varepsilon_{Rt}^{(ss)}$  is  $1/2, 1/9$  and  $1/99$ , respectively. When the critical strain is imposed to the one-element numerical model of the bar, the tangent stiffness matrix has a zero eigenvalue (up to the machine precision), independently of the number of integration segments. The bifurcation is captured exactly, because the bifurcation mode is very simple (zero deflection and uniform rotation) and thus can be reproduced by the numerical approximation, no matter how many integration segments are used.

Finally, consider a **bar clamped at both ends**, this time with  $h/L = 1/6$ . Since the buckling length is now  $L_b = L/2$ , the slenderness is evaluated as  $s = \sqrt{3}L/h \approx 10.392$ . The critical strains  $\varepsilon_{Rt}^{(dc)}$  obtained by solving equation (C.53) are listed in the penultimate column of Table 6. Numerically, the bar is modeled by 2 elements, each divided into 16 integration segments (for a one-element model, no global degrees of freedom would be introduced and the tangent stiffness could not be examined). The imposed

strain is again increased in increments of 0.001 and linear interpolation of the smallest eigenvalue is used. The agreement is excellent.

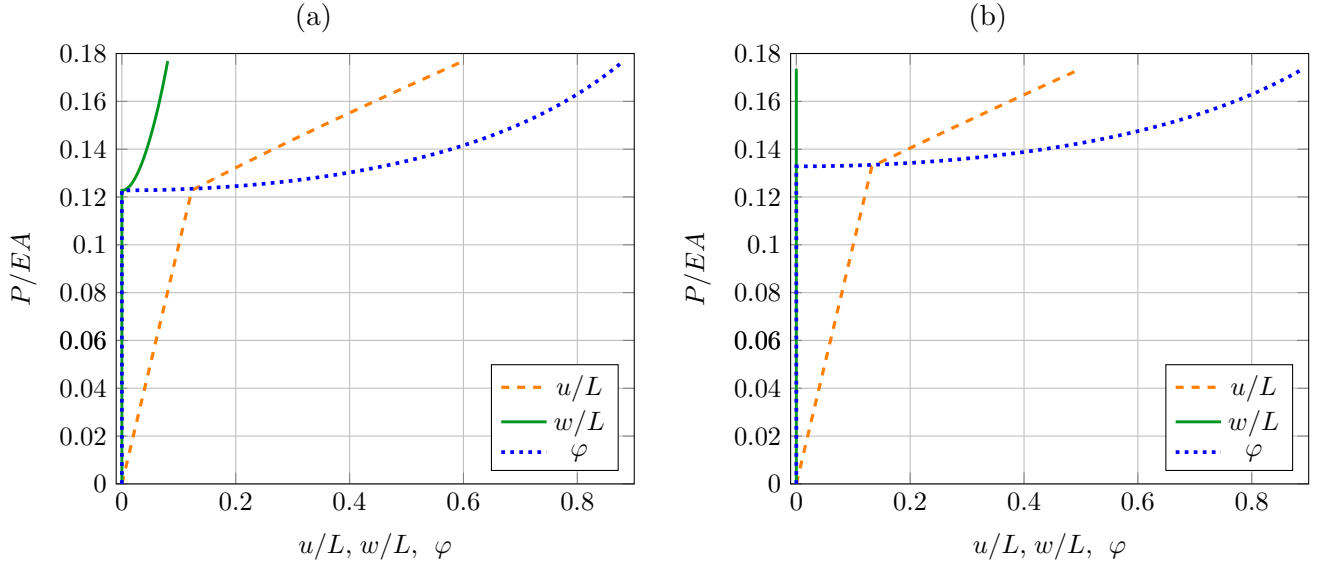


Figure 13: Load-displacement diagrams under tension obtained with the Reissner model for a bar (a) clamped at the left end,  $h/L = 1/4$ , (b) clamped at both ends,  $h/L = 1/6$

#### 5.4. Post-critical response in tension

Numerical simulations make it possible not only to detect the critical state, but also to trace the bifurcated solution in the post-critical range. The resulting diagrams in Fig. 13 show the evolution of selected degrees of freedom (nodal displacements and rotation) plotted against the applied loading force,  $P$ . By the adopted convention, negative  $P$  corresponds to tension, and thus the diagrams work with the absolute value of  $P$ , which represents the axial tensile force that would arise if the bar remained straight. On the vertical axis, the force is normalized by the sectional stiffness,  $EA$ . Before bifurcation, the bar is stretched uniformly and the normalized axial displacement,  $u/L$ , is equal to the normalized force,  $|P|/EA$ , since both represent the strain. Here,  $u$  is the axial displacement of the end section subjected to the external loading. For the bar clamped at the left end, the other quantities plotted in Fig. 13a are the transversal displacement  $w$  (also normalized by  $L$ ) and the rotation  $\varphi$  at the free right end. For the bar clamped at both ends, the transversal displacement and rotation plotted in Fig. 13b are

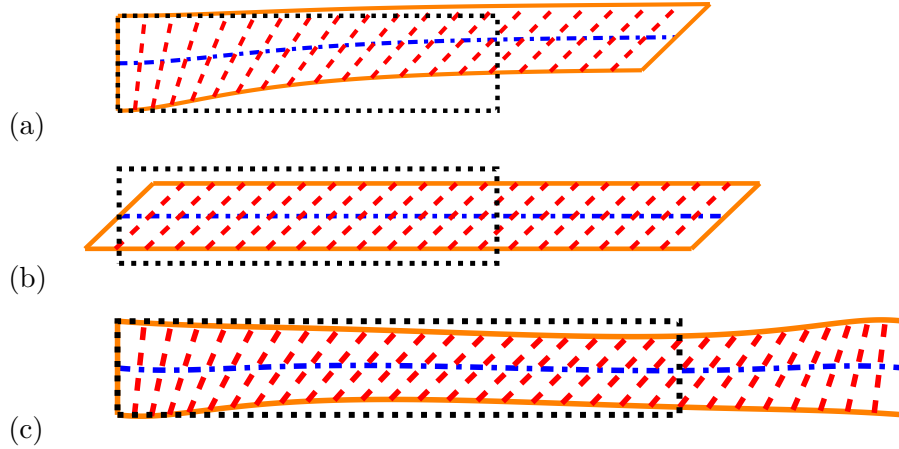


Figure 14: Deformed shapes in post-critical states under tension obtained with the Reissner model for a bar (a) clamped at the left end,  $h/L = 1/4$ , (b) simply supported,  $h/L = 1/4$ , (c) clamped at both ends,  $h/L = 1/6$  (the dotted rectangles represent the undeformed shapes)

traced at the middle section. In this case, the transversal displacement remains equal to zero even after the bifurcation, because the deformed shape is skew-symmetric. The deformed shapes in the post-critical range are visualized in Fig. 14, which shows not only the deformed centerline but also the inclination of selected cross sections, in order to demonstrate the predominant role of shear. The shapes correspond to a stage at which the maximum rotation is about 0.8. This is quite far beyond the bifurcation point, but the distribution of lateral displacement and rotation along the bar is still similar to the predicted bifurcation modes analyzed at the end of Appendix C.2.3.

The visualization of deformed shapes makes it easier to understand the nature of the tensile bifurcation. If the rotations are unconstrained, the segments exhibit uniform shear distortion (Fig. 14b). As neighboring segments slide with respect to each other, the centerline gets extended and the applied load can supply work, which is transformed into strain energy. If some constraints on rotations are imposed at one or both end sections, the region of the bar that is far from the support(s) develops a pattern that is close to uniform shear, but the boundary region(s) are affected by the constraint(s) and the load needed to drive the deformation is higher. For slender beams, the affected boundary regions are relatively small and the critical load is only slightly higher than for the uniform shear mode, while for stocky beams the boundary regions are more important and the critical load can be substantially higher, as seen in Fig. C.17.

Another interpretation of the bifurcation is that if the sections rotate while the bar axis remains straight, the applied force acting along the bar axis is according to the Reissner model decomposed into a normal force  $N$  perpendicular to the section and a shear force  $Q$  parallel to the section; these internal forces are expressed as  $N = |P| \cos \varphi$  and  $Q = |P| \sin \varphi$ , and they lead to deformation measures  $\varepsilon = N/EA$  and  $\gamma = Q/GA_s$ . Since the centerline remains straight, the rotation  $\varphi$  is equal to the shear angle  $\chi$ , which is linked to the deformation measures by

$$\tan \chi = \frac{\gamma}{1 + \varepsilon} \quad (121)$$

Making use of the relations mentioned above, we can set up the equation

$$\tan \varphi = \frac{|P| \sin \varphi / GA_s}{1 + |P| \cos \varphi / EA} \quad (122)$$

If the trivial case characterized by  $\sin \varphi = 0$  is excluded, the equation can be rewritten as

$$|P| \left( \frac{1}{GA_s} - \frac{1}{EA} \right) \cos \varphi = 1 \quad (123)$$

A non-trivial solution  $\varphi \neq 0$  exists only if

$$|P| \left( \frac{1}{GA_s} - \frac{1}{EA} \right) > 1 \quad (124)$$

which can be written as  $|P| > P_{Rt}^{(ss)}$  where

$$P_{Rt}^{(ss)} = \frac{1}{\frac{1}{GA_s} - \frac{1}{EA}} = EA \frac{1}{\frac{1}{\Gamma} - 1} = EA \frac{\Gamma}{1 - \Gamma} \quad (125)$$

This is an alternative derivation of the critical force for a simply supported bar, or of the corresponding critical tensile strain  $\varepsilon_{Rt}^{(ss)}$  given by (C.51). In addition to the bifurcation condition, we obtain an analytical description of the post-critical relation between the (normalized) applied force and the finite rotation,

$$\frac{|P|}{EA} = \frac{\Gamma}{(1 - \Gamma) \cos \varphi} \quad (126)$$

The total elongation of the bar can also be expressed analytically in the form

$$u = L \sqrt{(1 + \varepsilon)^2 + \gamma^2} = L \sqrt{\left( 1 + \frac{|P|}{EA} \cos \varphi \right)^2 + \left( \frac{|P|}{GA_s} \sin \varphi \right)^2} = \frac{|P| L}{GA_s} \quad (127)$$

## 6. Summary and conclusions

We have proposed and tested a two-dimensional beam element that can accommodate arbitrary displacements and rotations in a geometrically exact manner. The sectional equations that describe the link between internal forces and deformation variables defined at the level of an infinitesimal beam segment are considered as linear, but extensions to material nonlinearity could be incorporated. Beam segments can deform by axial stretching, shear and bending. These three modes are characterized by appropriate deformation variables and the corresponding work-conjugate internal forces. We have considered two formulations that differ in the choice of the variables that characterize axial and shear deformation.

The following particular features of our approach can be emphasized:

- For both formulations, the main advantage is that the minimum number of global degrees of freedom is dictated only by the topology of the frame structure, and the accuracy can be increased by refining the computational grid at the element level while the number of global degrees of freedom is kept fixed.
- Efficiency is also increased by directly addressing the global center-line coordinates and sectional inclination with respect to the global axes as the primary unknowns at the element level, thereby avoiding transformations between local and global coordinates.
- The algorithmic treatment has been extended to account for distributed loads and moments.
- Our model is not affected by shear locking, unlike displacement-based finite element formulations of the Reissner–Simo beam model that account for transverse shear deformation.
- Numerical simulations of both models confirm the results of the theoretical stability analysis and efficiently allow tracing the entire post-buckling response. The Reissner model can lead to bifurcations from a straight state under both compression and tension, whereas the Ziegler model, which is more suitable for sandwich-like sections and built-up columns, leads only to compressive buckling.
- The differences between the two models that arise from the choice of primary deformation variables and the reference system are reflected in the variation of internal forces along the beam.

Two main limitations that we aim to address in our future studies concern (i) the constitutive law, which is currently assumed to be linear elastic but, in general, should account for material nonlinearities to accurately describe the mechanical behaviour of materials such as rubbers and elastomers, and (ii) the two-dimensional formulation, which should be extended to 3D.

## Acknowledgments

M. Jirásek and M. Horák are grateful for the support of the Czech Science Foundation (project No. 19-26143X) received in 2023. In 2024, their work was co-funded by the European Union under the ROBOPROX project (reg. no. CZ.02.01.01/00/22 008/0004590) and by the Czech Ministry of Education, Youth and Sports (ERC CZ project No. LL2310).

A grant from the Ministry for University and Research (MUR) for PRIN 2022, project No. 2022P7PF8J\_002, LAttice STructures for Energy aB-sorption: advanced numerical analysis and optimal design (LASTEB), is gratefully acknowledged by C. Bonvissuto and E. La Malfa Ribolla.

## Appendix A. Two formulations of shear-flexible beams

### *Appendix A.1. Reissner model*

#### *Appendix A.1.1. Choice of deformation variables and strain energy density*

The sectional equations in the form originally suggested by Reissner [5] and adopted in many other studies for two-dimensional beams [35, 36, 37] as well as their extension to 3D [38, 39] are obtained if the strain energy density

$$\mathcal{E}_{int} = \frac{1}{2}EA\varepsilon^2 + \frac{1}{2}GA_s\gamma^2 + \frac{1}{2}EI\kappa^2 \quad (\text{A.1})$$

is postulated as a quadratic function of the curvature,  $\kappa$ , and of two additional strain measures,

$$\varepsilon = \lambda_s \cos \chi - 1 \quad (\text{A.2})$$

$$\gamma = \lambda_s \sin \chi \quad (\text{A.3})$$

which characterize the normal and shear deformation modes. Here,  $\lambda_s$  and  $\chi$  should be understood as intermediate variables with a clear geometric meaning, from which the “true” strain measures are derived. In the small-strain limit, the present description reduces to the classical Timoshenko-Ehrenfest beam theory [4, 40]. In the undeformed state, we have  $\lambda_s = 1$  and  $\chi = 0$ . If  $\lambda_s - 1 \ll 1$  and  $\chi \ll 1$ , the strain measures can be approximated

by  $\varepsilon \approx \lambda_s - 1 =$  relative change of length of the centerline and  $\gamma \approx \chi =$  small shear angle (understood as the effective value, since the actual shear strain would vary across the section). Therefore, factors  $EA$ ,  $GA_s$  and  $EI$  are standard sectional stiffnesses related to stretching, shear and bending that would be used by the linear Timoshenko model. Each of them is the product of an elastic modulus (Young's modulus  $E$ , or shear modulus  $G$ ) and a sectional geometry characteristic (sectional area  $A$ , shear effective sectional area[30]  $A_s$ , or sectional moment of inertia  $I$ ).

In the variational approach, the potential energy of the whole beam is considered as a functional dependent on the primary independent kinematic fields, i.e., on the centerline displacement components and the sectional rotation. For the centerline stretch, we can directly use relation (2). To express the shear angle  $\chi$ , we get back to the triangle in Fig. 1b and write

$$\sin(\varphi - \chi) = -\frac{z'_s}{\lambda_s} \quad (\text{A.4})$$

$$\cos(\varphi - \chi) = \frac{x'_s}{\lambda_s} \quad (\text{A.5})$$

For substitution into (A.2)–(A.3), we do not really need  $\chi$  itself but rather its sine and cosine. Rewriting the left-hand sides of (A.4)–(A.5) in terms of sine and cosine of  $\varphi$  and  $\chi$  and solving the resulting set of equations with the sine and cosine of  $\chi$  considered as unknowns, we obtain

$$\cos \chi = \frac{x'_s}{\lambda_s} \cos \varphi - \frac{z'_s}{\lambda_s} \sin \varphi \quad (\text{A.6})$$

$$\sin \chi = \frac{x'_s}{\lambda_s} \sin \varphi + \frac{z'_s}{\lambda_s} \cos \varphi \quad (\text{A.7})$$

Using this in (A.2)–(A.3), we finally arrive at the strain-displacement equations

$$\varepsilon = x'_s \cos \varphi - z'_s \sin \varphi - 1 \quad (\text{A.8})$$

$$\gamma = x'_s \sin \varphi + z'_s \cos \varphi \quad (\text{A.9})$$

#### *Appendix A.1.2. Variational derivation of differential equilibrium equations*

Let us now focus on the potential energy and its variation. The potential energy stored in the elastic deformation of the whole beam is given by

$$E_{int} = \int_0^L \mathcal{E}_{int} d\xi = \int_0^L \left( \frac{1}{2}EA\varepsilon^2 + \frac{1}{2}GA_s\gamma^2 + \frac{1}{2}EI\kappa^2 \right) d\xi \quad (\text{A.10})$$



and its first variation

$$\begin{aligned}
\delta E_{int} &= \int_0^L \left( \frac{\partial \mathcal{E}_{int}}{\partial \varepsilon} \delta \varepsilon + \frac{\partial \mathcal{E}_{int}}{\partial \gamma} \delta \gamma + \frac{\partial \mathcal{E}_{int}}{\partial \kappa} \delta \kappa \right) d\xi = \\
&= \int_0^L (EA\varepsilon \delta \varepsilon + GA_s \gamma \delta \gamma + EI\kappa \delta \kappa) d\xi = \\
&= \int_0^L (N \delta \varepsilon + Q \delta \gamma + M \delta \kappa) d\xi \tag{A.11}
\end{aligned}$$

can be interpreted as the internal virtual work done by the internal forces

$$N = \frac{\partial \mathcal{E}_{int}}{\partial \varepsilon} = EA\varepsilon \tag{A.12}$$

$$Q = \frac{\partial \mathcal{E}_{int}}{\partial \gamma} = GA_s \gamma \tag{A.13}$$

$$M = \frac{\partial \mathcal{E}_{int}}{\partial \kappa} = EI\kappa \tag{A.14}$$

on the virtual generalized strains  $\delta \varepsilon$ ,  $\delta \gamma$  and  $\delta \kappa$ . Based on (A.8)–(A.9) and (3), the virtual strains can be related to the virtual displacements and rotation:

$$\delta \varepsilon = \cos \varphi \delta x'_s - \sin \varphi \delta z'_s - \lambda_s \sin \chi \delta \varphi \tag{A.15}$$

$$\delta \gamma = \sin \varphi \delta x'_s + \cos \varphi \delta z'_s + \lambda_s \cos \chi \delta \varphi \tag{A.16}$$

$$\delta \kappa = \delta \varphi' \tag{A.17}$$

In (A.15)–(A.16), the factors multiplying  $\delta \varphi$  have been rewritten in terms of auxiliary variables  $\lambda_s$  and  $\chi$  based on relations (A.4)–(A.5), which will later facilitate the interpretation of equilibrium equation (A.23). Substitution of (A.15)–(A.17) into (A.11) followed by integration by parts leads to

$$\begin{aligned}
\delta E_{int} &= [(N \cos \varphi + Q \sin \varphi) \delta x_s + (-N \sin \varphi + Q \cos \varphi) \delta z_s + M \delta \varphi]_0^L + \\
&+ \int_0^L ((-N \cos \varphi - Q \sin \varphi)' \delta x_s + (N \sin \varphi - Q \cos \varphi)' \delta z_s) d\xi + \\
&+ \int_0^L (-N \lambda_s \sin \chi + Q \lambda_s \cos \chi - M') \delta \varphi d\xi \tag{A.18}
\end{aligned}$$

Suppose that the beam is loaded by distributed external forces described by global components  $p_x$  and  $p_z$ , and by a distributed external moment,  $m$ , all taken per unit length of the centerline in the undeformed state. The corresponding contribution to the potential energy is given by

$$E_{ext} = - \int_0^L (p_x x_s + p_z z_s + m \varphi) d\xi \tag{A.19}$$

and its variation is

$$\delta E_{ext} = - \int_0^L (p_x \delta x_s + p_z \delta z_s + m \delta \varphi) d\xi \quad (\text{A.20})$$

Stationarity requirements for the total potential energy  $E = E_{int} + E_{ext}$  correspond to a vanishing variation. Since the variations of centerline coordinates and sectional rotation are independent, condition  $\delta E = \delta E_{int} + \delta E_{ext} = 0$  leads to equations

$$-(N \cos \varphi + Q \sin \varphi)' = p_x \quad (\text{A.21})$$

$$(N \sin \varphi - Q \cos \varphi)' = p_z \quad (\text{A.22})$$

$$-N \lambda_s \sin \chi + Q \lambda_s \cos \chi - M' = m \quad (\text{A.23})$$

which can be interpreted as the equilibrium equations. Based on (A.6)–(A.7), equation (A.23) could be rewritten in terms of the primary kinematic fields and the internal forces as

$$-(x'_s \sin \varphi + z'_s \cos \varphi) N + (x'_s \cos \varphi - z'_s \sin \varphi) Q - M' = m \quad (\text{A.24})$$

### *Appendix A.1.3. Static boundary conditions*

Using the boundary terms in (A.18), we could also derive static (natural) boundary conditions at the beam ends. In the present context, the objective is not to solve a separate beam problem, but to develop the description of beam elements that will be assembled into a frame structure. The coordinates and inclination of the beam ends will be determined by the joint displacements and rotations, which represent the global degrees of freedom, i.e., the basic unknowns of the discretized frame model. In a typical incremental-iterative structural analysis, the basic tasks on the beam element level are to evaluate the end forces and moments generated by a given increment of joint displacements and rotations, and to evaluate the corresponding tangent element stiffness matrix. Therefore, when a beam element is processed, the coordinates and inclinations of the beam ends can be considered as given. The corresponding variations  $\delta x_s$ ,  $\delta z_s$  and  $\delta \varphi$  at the beam ends are then zero, and the boundary terms in (A.18) vanish. Nevertheless, for easier physical interpretation of the internal forces it is useful to look at the static boundary conditions that would arise if the end variations are considered as arbitrary. For instance, if the right beam end is considered as free and is loaded by a given horizontal force  $X_{ba}$ , vertical force  $Z_{ba}$  and moment  $M_{ba}$ , then the contribution of external forces to the potential energy should be enriched by the expression  $E_{ext,L} = -X_{ba}x_s(L) - Z_{ba}z_s(L) - M_{ba}\varphi(L)$ ,

and the stationarity conditions deduced from the terms that contain variations  $\delta x_s(L)$ ,  $\delta z_s(L)$  and  $\delta\varphi(L)$  read

$$N(L) \cos \varphi(L) + Q(L) \sin \varphi(L) = X_{ba} \quad (\text{A.25})$$

$$-N(L) \sin \varphi(L) + Q(L) \cos \varphi(L) = Z_{ba} \quad (\text{A.26})$$

$$M(L) = M_{ba} \quad (\text{A.27})$$

Since  $\varphi(L)$  is the inclination of the right end section with respect to the vertical global axis, it is clear that the internal forces  $N$  and  $Q$  have their standard meaning of the normal force, perpendicular to the section, and the shear force, parallel to the section, and  $M$  is the bending moment. This conclusion may look trivial, but in Section Appendix A.2 it will be shown that, for a model based on another set of deformation variables, the meaning of the work-conjugate quantities may be different.

In a completely analogous way, boundary conditions

$$-N(0) \cos \varphi(0) - Q(0) \sin \varphi(0) = X_{ab} \quad (\text{A.28})$$

$$N(0) \sin \varphi(0) - Q(0) \cos \varphi(0) = Z_{ab} \quad (\text{A.29})$$

$$-M(0) = M_{ab} \quad (\text{A.30})$$

valid at the left end can be derived. They differ only by the signs of the terms on the left-hand side. Of course, the terms on the right-hand side are the forces and the moment acting on the left end.

#### *Appendix A.1.4. Conversion to a set of first-order equations*

The complete Reissner beam model consists of equilibrium equations (A.21)–(A.22) and (A.24), sectional equations (A.12)–(A.14), and kinematic (strain-displacement) equations (A.8)–(A.9) and (3), supplemented by appropriate boundary conditions. Substituting the kinematic and sectional equations into the equilibrium equations, we could construct a set of three second-order differential equations for unknown functions  $x_s$ ,  $z_s$  and  $\varphi$ . Instead of that, let us first integrate the equilibrium equations analytically. Equations (A.21)–(A.22) with boundary conditions (A.28)–(A.29) have a closed-form solution

$$N = -(X_{ab} + P_x) \cos \varphi + (Z_{ab} + P_z) \sin \varphi \quad (\text{A.31})$$

$$Q = -(X_{ab} + P_x) \sin \varphi - (Z_{ab} + P_z) \cos \varphi \quad (\text{A.32})$$

where

$$P_x(\xi) = \int_0^\xi p_x(s) ds \quad (\text{A.33})$$

$$P_z(\xi) = \int_0^\xi p_z(s) ds \quad (\text{A.34})$$

are functions that can be deduced from the prescribed distributed load intensities  $p_x$  and  $p_z$ . Recall that  $X_{ab}$  and  $Z_{ab}$  are constants that represent the global components of the force between the left end of the beam and the joint to which it is attached. The values of functions  $P_x$  and  $P_z$  at  $\xi$  correspond to the resultants of the distributed loads between the left end and the section at distance  $\xi$  from the left end in the undeformed state. Clearly, equations (A.31)–(A.32) are force equilibrium equations for the part of the beam between the left end and the section characterized by  $\xi$ , written for the directions perpendicular to this section and parallel to this section.

An analogous formula can be constructed for the bending moment. Substituting (A.31)–(A.32) into (A.24) and rearranging the terms, we get

$$M' = -m + (X_{ab} + P_x)z'_s - (Z_{ab} + P_z)x'_s \quad (\text{A.35})$$

and, after integration,

$$M = -M_{ab} + X_{ab}(z_s - z_a) - Z_{ab}(x_s - x_a) + M_p \quad (\text{A.36})$$

where

$$M_p(\xi) = - \int_0^\xi m(s) ds + \int_0^\xi P_x(s) z'_s(s) ds - \int_0^\xi P_z(s) x'_s(s) ds \quad (\text{A.37})$$

and symbols  $x_a$  and  $z_a$  denote the current coordinates of the centroid of the left end section, i.e.,  $x_a = x_s(0)$  and  $z_a = z_s(0)$ . We have also exploited the static boundary condition (A.30).

The foregoing derivation may look somewhat complicated, but the result has a direct physical meaning. The first three terms on the right-hand side of (A.36) represent the contributions of a concentrated moment  $M_{ab}$  and forces  $X_{ab}$  and  $Z_{ab}$  applied at the left beam end to the bending moment at cross section  $x$ , taking into account the deformed state of the beam, and the last term,  $M_p$ , represents the contribution of the distributed loads to the same bending moment.

In summary, equations (A.31)–(A.32) and (A.36) are equilibrium equations in their integrated form, as opposed to the differential equations (A.21)–(A.22) and (A.24), which describe equilibrium of an infinitesimal beam segment. The internal forces are easily transformed into deformation variables

using the inverted form of sectional equations (A.12)–(A.14):

$$\varepsilon = \frac{N}{EA} \quad (\text{A.38})$$

$$\gamma = \frac{Q}{GA_s} \quad (\text{A.39})$$

$$\kappa = \frac{M}{EI} \quad (\text{A.40})$$

Kinematic equations (A.8)–(A.9) link deformation variables  $\varepsilon$  and  $\gamma$  to the derivatives of the displacement functions, and their inversion leads to

$$x'_s = (1 + \varepsilon) \cos \varphi + \gamma \sin \varphi \quad (\text{A.41})$$

$$z'_s = \gamma \cos \varphi - (1 + \varepsilon) \sin \varphi \quad (\text{A.42})$$

Substituting from (A.38)–(A.39) and (A.31)–(A.32) into (A.41)–(A.42), we end up with two first-order differential equations

$$x'_s = \left( 1 + \frac{-(X_{ab} + P_x) \cos \varphi + (Z_{ab} + P_z) \sin \varphi}{EA} \right) \cos \varphi - \frac{(X_{ab} + P_x) \sin \varphi + (Z_{ab} + P_z) \cos \varphi}{GA_s} \sin \varphi \quad (\text{A.43})$$

$$z'_s = -\frac{(X_{ab} + P_x) \sin \varphi + (Z_{ab} + P_z) \cos \varphi}{GA_s} \cos \varphi - \left( 1 + \frac{-(X_{ab} + P_x) \cos \varphi + (Z_{ab} + P_z) \sin \varphi}{EA} \right) \sin \varphi \quad (\text{A.44})$$

that contain three primary unknown functions,  $x_s$ ,  $z_s$  and  $\varphi$ . The third equation of a similar kind,

$$\varphi' = \frac{-M_{ab} + X_{ab}(z_s - z_a) - Z_{ab}(x_s - x_a) + M_p}{EI} \quad (\text{A.45})$$

is obtained simply by combining (3) with (A.40) and (A.36). Equations (A.43)–(A.45) form the theoretical basis of the numerical procedure developed in this paper. These first-order differential equations will be approximated using a finite difference scheme; see Section 3.3.1.

Similar, yet simpler equations were derived in [24] for the Kirchhoff beam in a somewhat different setting—the deformed shape of the centerline was described by the displacements (instead of current coordinates) with respect to a local coordinate system aligned with the beam. The present equations reduce to the formulation in [24] if the current coordinates are expressed as

$x_s = \xi + u_s$  and  $z_s = w_s$ , and the left-end coordinates  $x_a$  and  $z_a$  are set to  $u_a$  and  $w_a$ . Moreover, fractions with  $GA_s$  in the denominator are deleted, because the shear stiffness is considered as infinite (no shear distortion is taken into account), and functions  $P_x$ ,  $P_z$  and  $M_p$  that reflect the loads distributed along the beam are set to zero. After these modifications, equations (A.43)–(A.45) reduce to

$$u'_s = \left(1 + \frac{-X_{ab} \cos \varphi + Z_{ab} \sin \varphi}{EA}\right) \cos \varphi - 1 \quad (\text{A.46})$$

$$w'_s = -\left(1 + \frac{-X_{ab} \cos \varphi + Z_{ab} \sin \varphi}{EA}\right) \sin \varphi \quad (\text{A.47})$$

$$\varphi' = \frac{-M_{ab} + X_{ab}(w_s - w_a) - Z_{ab}(\xi + u_s - u_a)}{EI} \quad (\text{A.48})$$

This exactly corresponds to equations (37)–(39) from [24], with only a formal difference—coordinate  $\xi$  was replaced by  $x$ , because the coordinate system  $(x, y, z)$  used in [24] was local, aligned with the beam.

## *Appendix A.2. Ziegler model*

### *Appendix A.2.1. Choice of deformation variables*

The standard Reissner model, presented in Section Appendix A.1, characterizes the normal mode by the deformation variable  $\varepsilon$  defined in (A.2) and the shear mode by the deformation variable  $\gamma$  defined in (A.3). The work-conjugate quantities are then the normal force  $N$  perpendicular to the deformed section, and the shear force  $Q$  parallel to the deformed section. This choice conceptually corresponds to the work of Haringx [25], who studied the stability of helical springs and modified the previously used stability approach of Engesser [26]. Due to the particular definition of  $\varepsilon$ , the axial stiffness  $EA$  is activated by the change of distance between the neighboring sections. If the sections slide while keeping their distance constant, only the shear stiffness  $GA_s$  is activated. As will be shown in Section Appendix C.2, such a model predicts a certain finite critical load even in uniaxial tension, because the sliding mechanism can lead to an extension of the beam length measured along the centerline even at vanishing “normal strain”  $\varepsilon$ . On the other hand, in compression, the critical stress tends to infinity as the slenderness approaches zero.

Alternatively, the variable characterizing the normal mode can be derived from the change of length of the centerline, which can occur as a second-order effect also during parallel sliding of the sections. This point of view could be more appropriate for sandwich-like sections with top and bottom hard layers connected by a soft core, or for built-up columns modeled as

one single rod with equivalent sectional properties. Such an approach corresponds to the original Engesser model for stability of a shear-deformable column[26], which does not give any bifurcation in tension while in compression it yields a finite critical stress even in the limit of zero slenderness. In this extreme case, the buckling mode corresponds to a compressed layer in which individual fibers start rotating at a constant length, and the second-order work of the normal stress provides enough energy needed to induce shear deformation. In his simple stability analysis, Engesser[26] took into account the effect of shear distortion, but he still treated the beam axis as inextensible and incompressible. The effect of axial deformation was added by Ziegler[27], who demonstrated that it is of the same order of magnitude as the effect of shear. Ziegler's analysis was focused on stability of an initially straight column, and his basic equations contain some approximations based on the assumption of small rotations and small shear angles. Therefore, his approach was not geometrically exact, but his sectional equations can be combined with kinematic equations (A.8)–(A.9) and (3), leading to a model that can be considered as an alternative formulation of a geometrically exact beam. Adopting the terminology used in [22], we will refer to this formulation as the Ziegler model, even though it does not precisely correspond to the equations originally used in [27].

The foregoing considerations motivate a modified choice of deformation variables. Instead of  $\varepsilon$  defined in (A.2) and related to the change in distance between sections, let us use, as the deformation variable characterizing the normal mode, the axial strain

$$\varepsilon_s = \lambda_s - 1 = \sqrt{x_s'^2 + z_s'^2} - 1 \quad (\text{A.49})$$

This variable corresponds to the Biot (engineering) strain and represents the relative change of length of the centerline. For the shear deformation variable characterizing the shear mode, a natural choice is the shear angle  $\chi$ . Based on (A.4)–(A.5), the shear angle can be expressed as

$$\chi = \varphi + \arctan \frac{z_s'}{x_s'} \quad (\text{A.50})$$

The flexural deformation is still described by the curvature  $\kappa$  defined in (3).

#### *Appendix A.2.2. Variational derivation of differential equilibrium equations and static boundary conditions*

The elastic energy density can be again considered in the simple quadratic and decoupled form

$$\mathcal{E}_{int} = \frac{1}{2}EA\varepsilon_s^2 + \frac{1}{2}GA_s\chi^2 + \frac{1}{2}EI\kappa^2 \quad (\text{A.51})$$

which leads to linear sectional equations

$$\tilde{N} = \frac{\partial \mathcal{E}_{int}}{\partial \varepsilon_s} = EA\varepsilon_s \quad (\text{A.52})$$

$$\tilde{Q} = \frac{\partial \mathcal{E}_{int}}{\partial \chi} = GA_s\chi \quad (\text{A.53})$$

$$M = \frac{\partial \mathcal{E}_{int}}{\partial \kappa} = EI\kappa \quad (\text{A.54})$$

The physical meaning of internal forces  $\tilde{N}$  and  $\tilde{Q}$  is different from the previously used normal force  $N$  and shear force  $Q$ , and this is why they are denoted here by modified symbols with a tilde. This alternative form of the sectional equations has been debated and compared to the Reissner formulation by various authors[22, 41, 42]. It will be shown that  $\tilde{N}$  is the force tangent to the centerline and  $\tilde{Q}$  is the force perpendicular to the centerline multiplied by  $\lambda_s$ . On the other hand, the bending moment  $M$  keeps the same meaning as before.

For the Ziegler model, a variational procedure analogous to Section Appendix A.1.2 leads to the variation of stored elastic energy in the form

$$\delta E_{int} = \int_0^L \left( \tilde{N} \delta \varepsilon_s + \tilde{Q} \delta \chi + M \delta \kappa \right) d\xi \quad (\text{A.55})$$

After the substitution of the variations

$$\delta \varepsilon_s = \frac{x'_s \delta x'_s + z'_s \delta z'_s}{\lambda_s} = \cos(\varphi - \chi) \delta x'_s - \sin(\varphi - \chi) \delta z'_s \quad (\text{A.56})$$

$$\delta \chi = \delta \varphi + \frac{x'_s \delta z'_s - z'_s \delta x'_s}{\lambda_s^2} = \delta \varphi + \frac{\cos(\varphi - \chi) \delta z'_s + \sin(\varphi - \chi) \delta x'_s}{\lambda_s} \quad (\text{A.57})$$

$$\delta \kappa = \delta \varphi' \quad (\text{A.58})$$



and integration by parts, the expression for the variation is converted into

$$\begin{aligned}
\delta E_{int} = & \left[ \left( \tilde{N} \cos(\varphi - \chi) + \frac{\tilde{Q}}{\lambda_s} \sin(\varphi - \chi) \right) \delta x_s + \right. \\
& \left. + \left( -\tilde{N} \sin(\varphi - \chi) + \frac{\tilde{Q}}{\lambda_s} \cos(\varphi - \chi) \right) \delta z_s + M \delta \varphi \right]_0^L + \\
& + \int_0^L \left( -\tilde{N} \cos(\varphi - \chi) - \frac{\tilde{Q}}{\lambda_s} \sin(\varphi - \chi) \right)' \delta x_s \, d\xi + \\
& + \int_0^L \left( \left( \tilde{N} \sin(\varphi - \chi) - \frac{\tilde{Q}}{\lambda_s} \cos(\varphi - \chi) \right)' \delta z_s + (\tilde{Q} - M') \delta \varphi \right) d\xi
\end{aligned} \tag{A.59}$$

The variation of the energy of external forces  $\delta E_{ext}$  is still given by (A.20), with possible enhancements by boundary terms, and the resulting stationarity conditions derived from  $\delta E_{int} + \delta E_{ext} = 0$  read

$$-\left( \tilde{N} \cos(\varphi - \chi) + \frac{\tilde{Q}}{\lambda_s} \sin(\varphi - \chi) \right)' = p_x \tag{A.60}$$

$$\left( \tilde{N} \sin(\varphi - \chi) - \frac{\tilde{Q}}{\lambda_s} \cos(\varphi - \chi) \right)' = p_z \tag{A.61}$$

$$\tilde{Q} - M' = m \tag{A.62}$$

A comparison with equilibrium equations (A.21)–(A.23) previously derived for the Reissner model shows that, in the force equilibrium equations (A.60)–(A.61), the internal forces  $\tilde{N}$  and  $\tilde{Q}$  are now rotated by  $\varphi - \chi$ , which is the rotation of the tangent to the deformed centerline, while for the Reissner model the analogous forces  $N$  and  $Q$  were rotated by the sectional inclination angle,  $\varphi$ . Furthermore, force  $\tilde{Q}$  work-conjugate with the shear angle  $\chi$  is in the force equilibrium equations (A.60)–(A.61) divided by the centerline stretch,  $\lambda_s$ . To work with quantities that have a direct physical meaning, it is preferable to introduce the “true” force acting in the direction perpendicular to the deformed centerline, defined as  $Q^* = \tilde{Q}/\lambda_s$ . The equilibrium

equations then have the form

$$-\left(\tilde{N} \cos(\varphi - \chi) + Q^* \sin(\varphi - \chi)\right)' = p_x \quad (\text{A.63})$$

$$\left(\tilde{N} \sin(\varphi - \chi) - Q^* \cos(\varphi - \chi)\right)' = p_z \quad (\text{A.64})$$

$$\lambda_s Q^* - M' = m \quad (\text{A.65})$$

and the static boundary conditions, derived using the boundary terms in (A.59) combined with appropriate boundary terms in the variation of the external potential energy, read

$$-\tilde{N}(0) \cos(\varphi(0) - \chi(0)) - Q^*(0) \sin(\varphi(0) - \chi(0)) = X_{ab} \quad (\text{A.66})$$

$$\tilde{N}(0) \sin(\varphi(0) - \chi(0)) - Q^*(0) \cos(\varphi(0) - \chi(0)) = Z_{ab} \quad (\text{A.67})$$

$$-M(0) = M_{ab} \quad (\text{A.68})$$

$$\tilde{N}(L) \cos(\varphi(L) - \chi(L)) + Q^*(L) \sin(\varphi(L) - \chi(L)) = X_{ba} \quad (\text{A.69})$$

$$-\tilde{N}(L) \sin(\varphi(L) - \chi(L)) + Q^*(L) \cos(\varphi(L) - \chi(L)) = Z_{ba} \quad (\text{A.70})$$

$$M(L) = M_{ba} \quad (\text{A.71})$$

Notice that, if  $Q^*$  is used as one of the internal forces, sectional equation (A.53) needs to be rewritten as

$$Q^* = GA_s \frac{\chi}{\lambda_s} \quad (\text{A.72})$$

### *Appendix A.2.3. Conversion to a set of first-order equations*

The subsequent derivation proceeds in a similar way as in Section Appendix A.1.4 for the Reissner model, but it is somewhat more complicated. First, equilibrium equations in the differential form (A.63)–(A.65) are integrated and boundary conditions (A.66)–(A.68) are exploited. The resulting expressions for the internal forces are

$$\tilde{N} = -(X_{ab} + P_x) \cos(\varphi - \chi) + (Z_{ab} + P_z) \sin(\varphi - \chi) \quad (\text{A.73})$$

$$Q^* = -(X_{ab} + P_x) \sin(\varphi - \chi) - (Z_{ab} + P_z) \cos(\varphi - \chi) \quad (\text{A.74})$$

$$M = -M_{ab} + X_{ab}(z_s - z_a) - Z_{ab}(x_s - x_a) + M_p \quad (\text{A.75})$$

Equation (A.75) for the bending moment is exactly the same as equation (A.36) derived for the Reissner model. However, equations (A.73)–(A.74) for internal force components  $\tilde{N}$  and  $Q^*$  are different from equations (A.31)–(A.32) valid for the Reissner model, since the expressions on their right-hand sides contain not only the external forces and the primary kinematic

variables  $x_s$ ,  $z_s$  and  $\varphi$ , but also the shear angle  $\chi$ , which is one of the deformation variables. Therefore, when these expressions for internal forces are substituted into the inverted sectional equations

$$\varepsilon_s = \frac{\tilde{N}}{EA} \quad (\text{A.76})$$

$$\chi = \frac{\tilde{Q}}{GA_s} = \frac{\lambda_s Q^*}{GA_s} = \frac{(1 + \varepsilon_s) Q^*}{GA_s} \quad (\text{A.77})$$

$$\kappa = \frac{M}{EI} \quad (\text{A.78})$$

we find the deformation variables not only on the left-hand side, but two of them, namely  $\varepsilon_s$  and  $\chi$ , affect also the right-hand side. In particular, the relation obtained by substituting (A.74) into (A.77) is not an explicit formula for the evaluation of  $\chi$  from other variables, but an implicit definition of  $\chi$  as the solution of the nonlinear algebraic equation

$$\chi = -\frac{1 + \varepsilon_s}{GA_s} ((X_{ab} + P_x) \sin(\varphi - \chi) + (Z_{ab} + P_z) \cos(\varphi - \chi)) \quad (\text{A.79})$$

in which  $\varepsilon_s$  is given by (A.76) combined with (A.73) and thus also depends on  $\chi$ . This equation does not have a closed-form solution, but in practical computations can be treated numerically. Formally, we can define function  $f_\chi(\varphi, P_1, P_2)$  such that its value  $\chi$  for given arguments  $\varphi$ ,  $P_1$  and  $P_2$  is the solution of the equation

$$GA_s \chi + \left( 1 - \frac{P_1 \cos(\varphi - \chi) + P_2 \sin(\varphi - \chi)}{EA} \right) (P_1 \sin(\varphi - \chi) + P_2 \cos(\varphi - \chi)) = 0 \quad (\text{A.80})$$

that satisfies the constraint  $-\pi/2 < \chi < \pi/2$ . For an arbitrary  $\varphi$ , we have  $f_\chi(\varphi, 0, 0) = 0$ . This can be a starting point of an iterative scheme computing an approximation of  $f_\chi(\varphi, P_1, P_2)$  for general arguments  $P_1 = X_{ab} + P_x$  and  $P_2 = Z_{ab} + P_z$ , e.g., by the Newton method.

The last step of the derivation exploits kinematic equations (A.4)–(A.5), which provide expressions for the coordinate derivatives

$$x'_s = \lambda_s \cos(\varphi - \chi) = (1 + \varepsilon_s) \cos(\varphi - \chi) \quad (\text{A.81})$$

$$z'_s = -\lambda_s \sin(\varphi - \chi) = -(1 + \varepsilon_s) \sin(\varphi - \chi) \quad (\text{A.82})$$

Replacing  $\varepsilon_s$  by the expression obtained from (A.76) and (A.73), and replacing  $\chi$  by  $f_\chi(\varphi, X_{ab} + P_x, Z_{ab} + P_z)$ , we construct two first-order differential

equations

$$x'_s = \left( 1 - \frac{(X_{ab} + P_x) c_\varphi(\varphi, X_{ab} + P_x, Z_{ab} + P_z) - (Z_{ab} + P_z) s_\varphi(\varphi, X_{ab} + P_x, Z_{ab} + P_z)}{EA} \right) c_\varphi(\varphi, X_{ab} + P_x, Z_{ab} + P_z) \quad (\text{A.83})$$

$$z'_s = \left( -1 + \frac{(X_{ab} + P_x) c_\varphi(\varphi, X_{ab} + P_x, Z_{ab} + P_z) - (Z_{ab} + P_z) s_\varphi(\varphi, X_{ab} + P_x, Z_{ab} + P_z)}{EA} \right) s_\varphi(\varphi, X_{ab} + P_x, Z_{ab} + P_z) \quad (\text{A.84})$$

with unknown functions  $x_s$ ,  $z_s$  and  $\varphi$ . To simplify the notation, we have introduced auxiliary functions

$$c_\varphi(\varphi, P_1, P_2) = \cos(\varphi - f_\chi(\varphi, P_1, P_2)) \quad (\text{A.85})$$

$$s_\varphi(\varphi, P_1, P_2) = \sin(\varphi - f_\chi(\varphi, P_1, P_2)) \quad (\text{A.86})$$

The third differential equation,

$$\varphi' = \frac{-M_{ab} + X_{ab}(z_s - z_a) - Z_{ab}(x_s - x_a) + M_p}{EI} \quad (\text{A.87})$$

is then obtained from the kinematic equation  $\varphi' = \kappa$  combined with (A.78) and (A.75). This equation is exactly the same as equation (A.45) for the Reissner model, but equations (A.83)–(A.84) are different. They look more complicated than the corresponding equations (A.43)–(A.44) obtained for the Reissner model, but in Section 3.4 it will be shown that the numerical implementation is not much more demanding.

## Appendix B. Analytical solution for a cantilever subjected to uniformly distributed external moment

This derivation leads to a reference solution for the numerical simulations in Section 4.3. An initially straight cantilever of length  $L$  is loaded by an externally applied distributed moment of uniform intensity  $m$ . If we consider the left end as fixed and the right end as free, the fundamental equations (A.43)–(A.45), with  $M_{ab} = -mL$  and  $M_p(\xi) = -m\xi$  evaluated from (A.37), reduce to

$$x'_s = \cos \varphi \quad (\text{B.1})$$

$$z'_s = -\sin \varphi \quad (\text{B.2})$$

$$\varphi' = \frac{m}{EI}(L - \xi) \quad (\text{B.3})$$

Equation (B.3) with initial condition  $\varphi(0) = 0$  leads to

$$\varphi(\xi) = \frac{m}{2EI}(2L\xi - \xi^2) \quad (\text{B.4})$$

Substituting this into (B.1)–(B.2) and integrating, we obtain

$$\begin{aligned} x_s(\xi) &= \int_0^\xi \cos\left(\frac{m}{2EI}(2Ls - s^2)\right) ds = \\ &= \frac{L}{\mu} \left( \cos \frac{\pi\mu^2}{2} \left( C(\mu) - C\left(\mu - \frac{\mu\xi}{L}\right) \right) + \sin \frac{\pi\mu^2}{2} \left( S(\mu) - S\left(\mu - \frac{\mu\xi}{L}\right) \right) \right) \end{aligned} \quad (\text{B.5})$$

$$\begin{aligned} z_s(\xi) &= - \int_0^\xi \sin\left(\frac{m}{2EI}(2Ls - s^2)\right) ds = \\ &= \frac{L}{\mu} \left( \sin \frac{\pi\mu^2}{2} \left( C(\mu) - C\left(\mu - \frac{\mu\xi}{L}\right) \right) - \cos \frac{\pi\mu^2}{2} \left( S(\mu) - S\left(\mu - \frac{\mu\xi}{L}\right) \right) \right) \end{aligned} \quad (\text{B.6})$$

where

$$\mu = L\sqrt{\frac{m}{\pi EI}} \quad (\text{B.7})$$

is a dimensionless parameter introduced for convenience, and  $C$  and  $S$  are Fresnel integrals defined as

$$C(x) = \int_0^x \cos s^2 ds, \quad S(x) = \int_0^x \sin s^2 ds \quad (\text{B.8})$$

In particular, the coordinates of the cantilever tip in the deformed state are given by

$$x_b = x_s(L) = \frac{L}{\mu} \left( \cos \frac{\pi\mu^2}{2} C(\mu) + \sin \frac{\pi\mu^2}{2} S(\mu) \right) \quad (\text{B.9})$$

$$z_b = z_s(L) = \frac{L}{\mu} \left( \sin \frac{\pi\mu^2}{2} C(\mu) - \cos \frac{\pi\mu^2}{2} S(\mu) \right) \quad (\text{B.10})$$

### Appendix C. Bifurcation analysis

This appendix investigates how the choice of a specific formulation of the sectional equations affects bifurcations from a straight state of an axially loaded column. Analytical expressions for the critical load and buckling modes are derived for the Reissner and Ziegler models, and it is shown that the Reissner formulation can lead to bifurcations not only in compression but also in tension.

*Appendix C.1. General setting*

Let us first recall that the adopted flexibility-based approach to the description of a geometrically exact beam leads to a set of three first-order differential equations, which have the form (A.43)–(A.45) if the Reissner sectional equations are selected, or (A.83)–(A.84) and (A.87) if the Ziegler sectional equations are used. If an initially straight prismatic column of length  $L$  is loaded axially by a force  $P$  oriented such that  $P > 0$  leads to compression, and if no other loading is present, there exists a fundamental solution that corresponds to uniform compression, without any bending or shear. This solution is characterized by kinematic variables

$$x_{s0}(\xi) = \left(1 - \frac{P}{EA}\right) \xi \quad (\text{C.1})$$

$$z_{s0}(\xi) = 0 \quad (\text{C.2})$$

$$\varphi_0(\xi) = 0 \quad (\text{C.3})$$

which describe the centerline coordinates in the deformed state and the sectional inclination. Here we assume that the origin of the coordinate system is placed at the centroid of one end section, and that the  $x$ -axis passes through the centroid of the other end section and coincides with the local  $\xi$ -axis.

Functions (C.1)–(C.3) satisfy the governing differential equations and also the appropriate boundary conditions that correspond to various combinations of the end supports. For the axial direction, we always consider a blocked displacement at  $\xi = 0$  and a free displacement at  $\xi = L$ , where the external force  $P$  is applied. This means that the kinematic boundary condition

$$x_s(0) = 0 \quad (\text{C.4})$$

is imposed at the fixed end, while the free end is characterized by the static boundary condition  $X_{ba} = -P$ . Using global equilibrium, the latter condition can be transformed into

$$X_{ab} = P \quad (\text{C.5})$$

which is more handy for our purpose, since the governing differential equations contain the left-end forces  $X_{ab}$ ,  $Z_{ab}$  and  $M_{ab}$ .

For constraints imposed on the lateral displacement and sectional rotation, let us consider the following three options (Fig. C.15):

1. **A column clamped at one end**, with kinematic boundary conditions

$$z_s(0) = 0 \quad (\text{C.6})$$

$$\varphi(0) = 0 \quad (\text{C.7})$$

and static boundary conditions  $Z_{ba} = 0$  and  $M_{ba} = 0$ , which can be transformed via global equilibrium equations into

$$Z_{ab} = 0 \quad (\text{C.8})$$

$$M_{ab} = P z_s(L) \quad (\text{C.9})$$

2. **A simply supported column**, with kinematic boundary conditions

$$z_s(0) = 0 \quad (\text{C.10})$$

$$z_s(L) = 0 \quad (\text{C.11})$$

and static boundary conditions  $M_{ab} = 0$  and  $M_{ba} = 0$ , which can be transformed via global equilibrium equations into

$$Z_{ab} = 0 \quad (\text{C.12})$$

$$M_{ab} = 0 \quad (\text{C.13})$$

3. **A column clamped at both ends**, with kinematic boundary conditions

$$z_s(0) = 0 \quad (\text{C.14})$$

$$\varphi(0) = 0 \quad (\text{C.15})$$

$$z_s(L) = 0 \quad (\text{C.16})$$

$$\varphi(L) = 0 \quad (\text{C.17})$$

Let us now examine whether, for a given force  $P$ , there exists a slightly perturbed solution that differs from the fundamental one but also satisfies the governing equations and boundary conditions. The perturbations are denoted by  $\delta$  preceding the original symbol, and they are considered as infinitely small, which makes it possible to linearize the governing equations around the fundamental solution. The fully general form of the linearized equations would be quite lengthy, but it is greatly simplified when the fundamental solution is substituted. For instance, since  $\varphi(\xi) = 0$ , all terms with  $\sin \varphi$  vanish and  $\cos \varphi$  can be replaced by 1. For the fundamental solution,  $X_{ab} = P$ ,  $Z_{ab} = 0$  and  $M_{ab} = 0$ , but the perturbations  $\delta Z_{ab}$  and  $\delta M_{ab}$  can be nonzero while  $\delta X_{ab} = 0$ . No distributed loads are considered, and so functions  $P_x$ ,  $P_z$  and  $M_p$  vanish and their perturbations as well.

It should be emphasized that the mathematical analysis to be presented next is focused on the possible bifurcation from the fundamental solution. The lowest load at which such a bifurcation is detected will be considered as

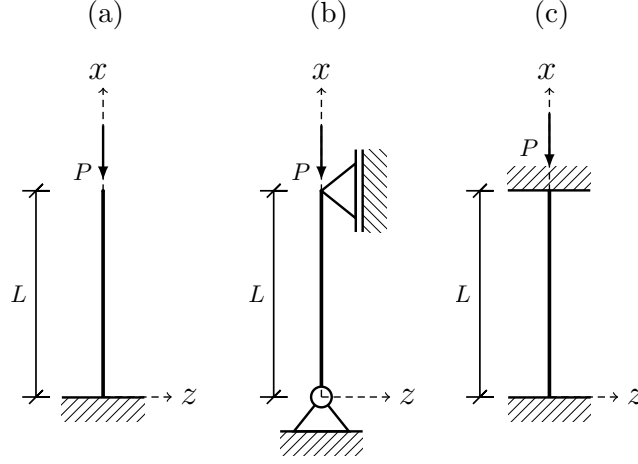


Figure C.15: Types of supports considered in the analysis: (a) a column clamped at one end, (b) a simply supported column, (c) a column clamped at both ends

the critical load. Before the critical load is attained, the solution is unique and it could be shown that it is stable in the sense that an arbitrary infinitesimal perturbation would lead to a (second-order) increase of the potential energy. When the critical load is exceeded, the fundamental solution typically loses stability and the physical system follows a bifurcated branch of the equilibrium diagram.

### Appendix C.2. Critical load – Reissner model

#### Appendix C.2.1. General analysis

For the Reissner model, linearization of the governing equations (A.43)–(A.45) around the fundamental solution (C.1)–(C.3) yields

$$\delta x'_s = 0 \quad (\text{C.18})$$

$$\delta z'_s = -\frac{1}{GA_s} (P \delta \varphi + \delta Z_{ab}) - \left(1 - \frac{P}{EA}\right) \delta \varphi \quad (\text{C.19})$$

$$\delta \varphi' = \frac{1}{EI} \left( -\delta M_{ab} + P \delta z_s - \delta Z_{ab} \left(1 - \frac{P}{EA}\right) \xi \right) \quad (\text{C.20})$$

Equation (C.18) with boundary condition (C.4) leads to  $\delta x_s(\xi) = 0$ . Equations (C.19)–(C.20) with unknown functions  $\delta z_s$  and  $\delta \varphi$  can be combined into a single second-order differential equation with one unknown function. Differentiating (C.20) and replacing  $\delta z'_s$  by the right-hand side of (C.19), we obtain, after a rearrangement,

$$EI \delta \varphi'' + (1 + \beta P) P \delta \varphi = -(1 + \beta P) \delta Z_{ab} \quad (\text{C.21})$$



where

$$\beta = \frac{1}{GA_s} - \frac{1}{EA} \quad (\text{C.22})$$

is a newly introduced constant, which can be evaluated from the given sectional stiffnesses.

In cases when  $(1 + \beta P)P > 0$ , the general solution of equation (C.21) has the form

$$\delta\varphi(\xi) = -\frac{\delta Z_{ab}}{P} + C_1 \cos k\xi + C_2 \sin k\xi \quad (\text{C.23})$$

where

$$k = \sqrt{\frac{(1 + \beta P)P}{EI}} \quad (\text{C.24})$$

and  $C_1$  and  $C_2$  are arbitrary integration constants. The subsequent analysis depends on the chosen type of supports.

1. For a **column with one clamped end**, the solution of (C.19)–(C.20) must satisfy conditions  $\delta z_s(0) = 0$ ,  $\delta\varphi(0) = 0$ ,  $\delta Z_{ab} = 0$  and  $\delta M_{ab} = P \delta z_s(L)$ , which follow directly from (C.6)–(C.9). Equation (C.20) evaluated at  $\xi = L$  is then exploited to construct a second condition written in terms of the primary unknown  $\delta\varphi$ , namely  $\delta\varphi'(L) = 0$ , which complements the kinematic boundary condition  $\delta\varphi(0) = 0$ . Substitution of the general solution (C.23) with  $\delta Z_{ab}$  set to zero into these two conditions then gives

$$C_1 = 0 \quad (\text{C.25})$$

$$-C_1 k \sin kL + C_2 k \cos kL = 0 \quad (\text{C.26})$$

A non-trivial solution exists only if  $\cos kL = 0$ . Since  $k > 0$ , this condition is satisfied for  $kL = (n - 1/2)\pi$  where  $n$  is a positive integer. For  $n = 1$ , condition  $kL = \pi/2$  can be rewritten in terms of force  $P$  as

$$(1 + \beta P)P = P_E \quad (\text{C.27})$$

where

$$P_E = \frac{EI\pi^2}{4L^2} \quad (\text{C.28})$$

is the Euler critical load for a column of buckling length  $L_b = 2L$ . The solution of our problem would be equal to the Euler critical load only if  $\beta = 0$ , which happens for  $GA_s = EA$ . For nonzero values of  $\beta$ , it is necessary to solve a quadratic equation, which has two roots,

$$P_{1,2} = \frac{-1 \pm \sqrt{1 + 4\beta P_E}}{2\beta} \quad (\text{C.29})$$

2. For a **simply supported column**, the perturbations  $\delta Z_{ab}$  and  $\delta M_{ab}$  vanish by virtue of (C.12)–(C.13), and so the general solution (C.23) reduces again to  $\delta\varphi(\xi) = C_1 \cos k\xi + C_2 \sin k\xi$ . Boundary conditions (C.10)–(C.11) lead to analogous conditions for  $\delta z_s(0)$  and  $\delta z_s(L)$ , which can be substituted into (C.20) to obtain conditions  $\delta\varphi'(0) = 0$  and  $\delta\varphi'(L) = 0$  written in terms of the primary unknown function. Substituting the general solution, we get linear equations for the integration constants,

$$C_2 k = 0 \quad (\text{C.30})$$

$$-C_1 k \sin kL + C_2 k \cos kL = 0 \quad (\text{C.31})$$

A non-trivial solutions exists only if  $\sin kL = 0$ , which holds for  $k = n\pi/L$  where  $n$  is a positive integer. In terms of the loading force  $P$ , this leads again to equation (C.27), in which

$$P_E = \frac{EI\pi^2}{L^2} \quad (\text{C.32})$$

is the Euler critical load for a column of buckling length  $L_b = L$ . For  $\beta \neq 0$ , the roots are again given by (C.29), just the meaning of  $P_E$  is different as compared to the column clamped at one end.

3. Finally, for a **column clamped at both ends**, the values of  $\delta Z_{ab}$  and  $\delta M_{ab}$  are not deducible from global equilibrium (since this case is statically indeterminate), but we can use four kinematic boundary conditions (C.14)–(C.17), rewritten in terms of the perturbations. Conditions (C.15) and (C.17) applied to the general solution (C.23) lead to

$$-\frac{\delta Z_{ab}}{P} + C_1 = 0 \quad (\text{C.33})$$

$$-\frac{\delta Z_{ab}}{P} + C_1 \cos kL + C_2 \sin kL = 0 \quad (\text{C.34})$$

while conditions (C.14) and (C.16) need to be combined with (C.20) written at  $\xi = 0$  and  $\xi = L$ , in order to construct conditions for the primary unknown function  $\varphi$ . The resulting equations read

$$C_2 k = -\frac{\delta M_{ab}}{EI} \quad (\text{C.35})$$

$$-C_1 k \sin kL + C_2 k \cos kL = -\frac{\delta M_{ab}}{EI} - \frac{\delta Z_{ab}}{EI} \left(1 - \frac{P}{EA}\right) \quad (\text{C.36})$$

Elimination of the static unknowns  $\delta Z_{ab}$  and  $\delta M_{ab}$  based on (C.33) and (C.35) then yields a set of two homogeneous linear equations for the integration constants:

$$\begin{pmatrix} \cos kL - 1 & \sin kL \\ \left(1 - \frac{P}{EA}\right) \frac{PL}{EI} - k \sin kL & k(\cos kL - 1) \end{pmatrix} \begin{pmatrix} C_1 \\ C_2 \end{pmatrix} = \begin{pmatrix} 0 \\ 0 \end{pmatrix} \quad (\text{C.37})$$

A non-trivial solution exists only if the determinant of the square matrix vanishes. After simple rearrangements, we obtain a nonlinear equation

$$2k \sin^2 \frac{kL}{2} - \left(1 - \frac{P}{EA}\right) \frac{PL}{EI} \sin \frac{kL}{2} \cos \frac{kL}{2} = 0 \quad (\text{C.38})$$

which is satisfied if

$$\sin \frac{kL}{2} = 0 \quad (\text{C.39})$$

or if

$$\tan \frac{kL}{2} = \left(1 - \frac{P}{EA}\right) \frac{PL}{2kEI} \quad (\text{C.40})$$

The first case is easy to handle and leads to  $k = 2n\pi/L$ , which for  $n = 1$  yields once again equation (C.27), in which

$$P_E = \frac{4EI\pi^2}{L^2} \quad (\text{C.41})$$

is the Euler critical load for a column of buckling length  $L_b = L/2$ . Analysis of condition (C.40) is postponed to the detained discussion of compressive and tensile bifurcations, because its relevance is affected by the sign of  $P$ .

The analysis has confirmed that the compressive critical load that corresponds to various types of support arrangements can be evaluated from a quadratic equation in a unified form (C.27), in which the constant  $P_E$  on the right-hand side has the meaning of the classical Euler buckling load  $P_E = EI\pi^2/L_b^2$ , where  $L_b$  is the buckling length with the same meaning as in the classical analysis, i.e.,  $L_b = 2L$  for a column clamped at one end,  $L_b = L$  for a simply supported (pin-ended) column, and  $L_b = L/2$  for a column clamped at both ends. Equation (C.27) is equivalent with a condition derived, in a somewhat different notation, by Haringx in his paper on helical springs (see the unnumbered equation between equations (11) and (12) in Haringx[25], in which  $\xi$  corresponds to our  $P_0/EA$ ,  $l_0$  to our  $L$ , and  $\alpha_0$ ,  $\beta_0$  and  $\gamma_0$  to our  $EI$ ,  $GA_s$  and  $EA$ , respectively).

For standard beams, the shear sectional stiffness,  $GA_s$ , can be expected to be smaller than the axial sectional stiffness,  $EA$ , unless the material and section have very unusual properties (e.g., a strongly auxetic material with  $\nu < -0.5$  and thus  $G > E$ ). For  $GA_s < EA$ , parameter  $\beta$  given by (C.22) is positive, both roots are real, and it is interesting to see that one is positive and the other negative, indicating a potential bifurcation in tension. Haringx[25] focused exclusively on the root that corresponds to compression. It is also worth noting that he provided closed-form expressions for the equivalent sectional stiffnesses of a helical spring modeled as a straight beam. If these expressions are adopted, the resulting dimensionless ratio  $GA_s/EA$  is  $2(1+m)/m$ , where  $m$  was referred to as the Poisson ratio by Haringx, but its value was substituted as  $10/3$  and in today's terminology it represents the reciprocal value  $1/\nu$  of the actual Poisson ratio  $\nu$ . This leads, for springs, to  $GA_s/EA = 2(1 + \nu)$ , which is typically somewhere near 2.5. From this point of view, it makes sense to consider cases with  $GA_s > EA$  as well.

#### *Appendix C.2.2. Compressive buckling*

For easier interpretation of the results, it is useful to work with a dimensionless stiffness ratio  $\Gamma = GA_s/EA$ , which is usually smaller than 1 but for springs can be larger. For a typical material and section, we can set for instance  $E/G = 2(1+\nu) = 2.5$  (isotropic material with Poisson ratio 0.25) and  $A/A_s = 1.2$  (rectangular section), which gives  $\Gamma = 1/3$ , as used in several examples in Section 4. According to the analysis presented in Section Appendix C.2.1, the critical load in compression is for the Reissner model given by the positive root of equation (C.27), in which  $P_E$  corresponds to the standard Euler critical load for the given type of supports. The positive root is obtained if the sign before the square root in formula (C.29) is taken as positive. Since parameter  $\beta$  is given by (C.22), the resulting formula for the critical load in compression can be written as

$$P_{Rc} = \frac{\sqrt{1 + 4 \left( \frac{1}{GA_s} - \frac{1}{EA} \right) P_E} - 1}{2 \left( \frac{1}{GA_s} - \frac{1}{EA} \right)} = \frac{EA}{2} \frac{\Gamma}{1 - \Gamma} \left( \sqrt{1 + \frac{4(1 - \Gamma) P_E}{\Gamma EA}} - 1 \right) \quad (\text{C.42})$$

For slender columns, the Euler critical load  $P_E$  is much smaller than the sectional stiffness  $EA$ . It is then possible to use the approximation

$$P_{Rc} \approx \frac{EA}{2} \frac{\Gamma}{1 - \Gamma} \left( 1 + \frac{1}{2} \cdot \frac{4(1 - \Gamma) P_E}{\Gamma EA} - 1 \right) = P_E = \frac{EI\pi^2}{L^2} \quad (\text{C.43})$$

Without the approximation, the exactly evaluated critical load will be somewhat smaller than the Euler load (provided that  $\Gamma < 1$ , i.e.,  $GA_s < EA$ ). Let us explore how the slenderness affects the critical stress, defined as  $\sigma_{Rc} = P_{Rc}/A$  (actually representing the magnitude of the compressive stress at the onset of buckling). Introducing the radius of inertia  $i_y = \sqrt{I/A}$  and the slenderness ratio  $s = L_b/i_y$ , we can express  $P_E/EA = \pi^2/s^2$  and

$$\sigma_{Rc} = \frac{P_{Rc}}{A} = \frac{E}{2} \frac{\Gamma}{1-\Gamma} \left( \sqrt{1 + \frac{4\pi^2(1-\Gamma)}{\Gamma s^2}} - 1 \right) \quad (\text{C.44})$$

For large slenderness,  $s \rightarrow \infty$ , this gives  $\sigma_{Rc} \approx E\pi^2/s^2$ , which corresponds to the Euler hyperbola. For small slenderness,  $s \rightarrow 0^+$ , we get

$$\sigma_{Rc} \approx \frac{E\pi}{s} \sqrt{\frac{\Gamma}{1-\Gamma}} \quad (\text{C.45})$$

So the critical stress tends to infinity, in inverse proportion to the slenderness. Of course, this is just theoretical description of the asymptotic behavior of the solution. In reality, the solution becomes physically meaningless for  $\lambda_{s0} \leq 0$ , i.e., for a critical stress that attains or exceeds  $E$ . For the already mentioned typical material and section characterized by  $\Gamma = 1/3$ , formula (C.45) would give  $\sigma_{Rc} \approx E$  for slenderness  $s = \pi/\sqrt{2} \approx 2.22$ . The sectional equation that postulates proportionality between the normal force and the engineering strain is certainly not realistic if the strain becomes truly large. Nevertheless, the analysis of asymptotic properties is useful for comparison of the main features of various models.

For illustration, the dependence of the normalized critical stress  $\sigma_{Rc}/E$  on the slenderness  $s$  is plotted in Fig. C.16 for various values of parameter  $\Gamma$ . The ratio  $\sigma_{Rc}/E = \varepsilon_{Rc}$  can be interpreted as the critical strain (in compression, but with a positive sign). For comparison, the graph also contains curves that are obtained if the shear compliance is neglected (Kirchhoff model), or if both the shear and the normal compliance are neglected (Euler model). In these extreme cases, it is not possible to use formula (C.42), which is valid only as long as  $\Gamma < 1$ , i.e.,  $GA_s < EA$ . For the limit cases, we need to go back to condition (C.27). If  $GA_s \rightarrow \infty$  while  $EA$  is finite, the equation remains quadratic and its solutions are still given by (C.29), in which  $\beta = -1/(EA)$  is negative. The denominator is then negative and both roots are positive, the smallest one being given by

$$P_K = \frac{EA}{2} \left( 1 - \sqrt{1 - \frac{4P_E}{EA}} \right) \quad (\text{C.46})$$

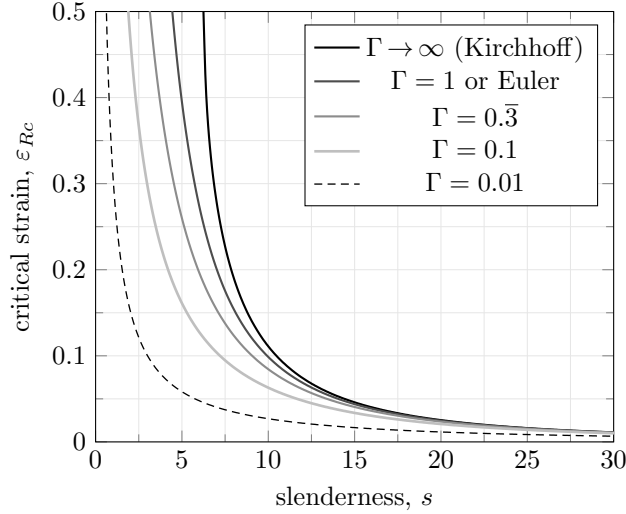


Figure C.16: Reissner model: dependence of the critical compressive strain (i.e., normalized critical stress)  $\varepsilon_{Rc} = \sigma_{Rc}/E$  on the slenderness  $s$  for selected values of parameter  $\Gamma = GA_s/EA$ . The Euler hyperbola described by  $\varepsilon_E = \pi^2/s^2$  is obtained as a special case with  $GA_s \rightarrow \infty$  and  $EA \rightarrow \infty$ , and it also corresponds to the case when  $\Gamma = 1$ .

from which

$$\sigma_K = \frac{P_K}{A} = \frac{E}{2} \left( 1 - \sqrt{1 - \frac{4\pi^2}{s^2}} \right) \quad (\text{C.47})$$

On the other hand, if both  $GA_s$  and  $EA$  are considered infinite, condition (C.27) reduces to a linear equation with only one solution,  $P = P_E$ . The critical load is then the classical Euler buckling load,  $P_E = EI\pi^2/L_b^2$ , and the corresponding graphical representation of the critical strain (or rather normalized critical stress)  $\varepsilon_E = \pi^2/s^2$  is the Euler hyperbola. Interestingly, exactly the same dependence would be obtained for finite stiffnesses if  $GA_s = EA$ , i.e.  $\Gamma = 1$  and  $\beta = 0$ . For  $\Gamma > 1$ , the corresponding curve is above the Euler hyperbola, which means that the properly evaluated critical load would be larger than the Euler load. This is caused by the stabilizing effect of the shortening of the column due to compressive axial deformation. The Euler solution refers to the buckling length evaluated from the initial undeformed length,  $L$ , but the buckling load of an axially compressible column with zero shear flexibility is  $EI\pi^2/(\lambda_{crit}L_b)^2$  where  $\lambda_{crit}$  is the stretch at the onset of buckling. Added shear flexibility has a destabilizing effect, but as long as  $GA_s > EA$ , the stabilizing effect of the axial shortening prevails. However, this is rather an artificial case. As already mentioned,

the shear stiffness is typically smaller than the axial stiffness, and then the critical load is below the Euler load. For low shear stiffness, the difference can be dramatic.

*Appendix C.2.3. Tensile bifurcation*

In addition to the positive root, equation (C.27) has also a negative root, which indicates a bifurcation in tension (in cases when  $\Gamma < 1$ ). The critical load for tension is evaluated as

$$|P_{Rt}| = \frac{1 + \sqrt{1 + 4P_E \left( \frac{1}{GA_s} - \frac{1}{EA} \right)}}{2 \left( \frac{1}{GA_s} - \frac{1}{EA} \right)} \quad (\text{C.48})$$

and the corresponding critical strain in tension is

$$\varepsilon_{Rt} = \frac{|P_{Rt}|}{EA} = \frac{\Gamma}{2(1 - \Gamma)} \left( 1 + \sqrt{1 + \frac{4(1 - \Gamma)\pi^2}{\Gamma s^2}} \right) \quad (\text{C.49})$$

For selected values of  $\Gamma = 1/3$  (homogeneous bar with  $\nu = 0.25$  and rectangular section),  $\Gamma = 0.1$  and  $0.01$  (sandwich bars with relatively low and extremely low shear stiffness), the dependence of the critical strain on slenderness given by (C.49) is visualized by the dashed curves in Fig. C.17 (labeled as 'clamped', which will be explained later). Since the analyzed member is loaded by axial tension, we refer in this section to a bar instead of a column, but this is just a formal difference. If the critical strain is too high, the loss of stability would be predicted for a state in which the simple linear model is not realistic, and refined analysis would be needed. For increasing slenderness, the critical strain approaches (from above) a finite limit, given by  $\Gamma/(1 - \Gamma)$ . For our typical case with  $\Gamma = 1/3$ , the limit value would be 0.5, i.e., 50% strain. Physically, the solution is not totally meaningless, but the range in which the relation between the nominal stress and engineering strain is approximately linear would most likely be exceeded. However, for sections with a low shear stiffness (compared to the axial stiffness), the critical strain in tension could easily fall into the almost linear range. Therefore, the model is in principle capable of describing a certain type of bifurcation under axial tension, caused by a sliding-type mechanism similar to those observed in [43].

Interestingly, it turns out that the tensile bifurcation cannot be described in a unified format, covering various combinations of supports by a single

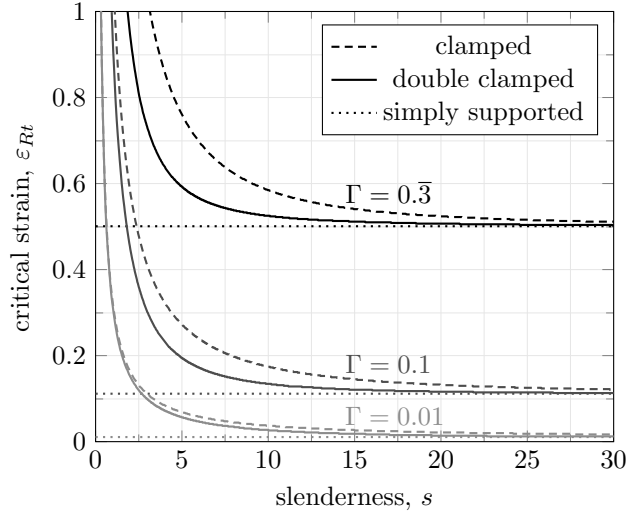


Figure C.17: Reissner model: dependence of the critical tensile strain on the slenderness for three selected values of parameter  $\Gamma = GA_s/EA$ , evaluated for a bar clamped at one end (dashed curves), a bar clamped at both ends (solid curves), and a simply supported bar (dotted straight lines)

formula. If the loading leads to tension, which means that the force  $P$  introduced in Fig. C.15 is considered as negative, the analysis of the critical state presented in Section Appendix C.2.1 needs to be refined. The first assumption that needs attention is that the general solution (C.23) of differential equation (C.21) was written only for the case when  $(1 + \beta P)P > 0$ . This is guaranteed if compression is applied ( $P > 0$ ) and parameter  $\beta$  is positive ( $GA_s < EA$ ). However, in general, one should also investigate cases when  $(1 + \beta P)P$  is zero or negative.

For  $(1 + \beta P)P < 0$ , functions sine and cosine in the general solution are replaced by their hyperbolic counterparts. Detailed analysis of various combinations of boundary conditions leads to the conclusion that the only solution is the trivial one, which means that the bifurcation is excluded. On the other hand, the assumption that  $(1 + \beta P)P = 0$ , which effectively means that  $1 + \beta P = 0$ , reduces equation (C.21) to  $EI \delta\varphi'' = 0$  and the general solution is an arbitrary linear function  $\delta\varphi(\xi) = C_1 + C_2\xi$ . For bars clamped at one or at both ends, the boundary conditions do not allow for any nontrivial solution of this kind, but for a **simply supported bar** (pinned at both ends), a constant function  $\delta\varphi(\xi) = C_1$  satisfies conditions  $\delta\varphi'(0) = 0$  and well as  $\delta\varphi'(L) = 0$ , and a non-trivial solution exists. A



constant rotation function combined with zero displacement functions is a possible bifurcation mode. The corresponding critical force is determined from condition  $1 + \beta P = 0$ , which gives

$$P_{crit} = -\frac{1}{\beta} = \frac{GA_s \cdot EA}{GA_s - EA} = \frac{\Gamma}{\Gamma - 1} EA \quad (\text{C.50})$$

For  $\Gamma > 1$  (i.e.,  $GA_s > EA$ ), this force is positive and larger than  $EA$ , which is not admissible because the column length in such a critical state would be negative. However, for  $\Gamma < 1$ , this critical force is negative and corresponds to a bar under tension, with the critical strain equal to  $\Gamma/(1-\Gamma)$ , which is always lower than the critical strain from (C.49). Consequently, the simply supported bar under tension (described by the Reissner model with  $GA_s < EA$ ) can bifurcate into a special uniform mode with constant rotation and zero displacements, and this happens at critical strain

$$\varepsilon_{Rt}^{(ss)} = \frac{\Gamma}{1 - \Gamma} = \frac{GA_s}{EA - GA_s} \quad (\text{C.51})$$

Superscript 'ss' refers to 'simply supported'. It is remarkable that this critical strain is independent of the slenderness, and it is equal to  $1/2$  for  $\Gamma = 1/3$ , to  $1/9$  for  $\Gamma = 0.1$ , and to  $1/99$  for  $\Gamma = 0.01$ ; see the dotted horizontal lines in Fig. C.17.

Yet another refinement of the bifurcation analysis under tension is needed for a **bar clamped at both ends**. The reason is that condition (C.38) derived in Section Appendix C.2.1 can be satisfied in two ways, described by (C.39) and (C.40), respectively. We have tacitly assumed that (C.39) is satisfied for a lower load level than (C.40) and thus determines the critical load. This is true for compression, when  $P > 0$  and the right-hand side of (C.40) is positive. The smallest positive root of (C.39) is  $kL/2 = \pi$ , while (C.40) with a positive right-hand side cannot be satisfied by any positive value of  $kL/2$  between 0 and  $\pi$ . This is why it was correct to describe the critical load in compression by equation (C.27), with  $P_E$  set to the standard Euler critical load. However, when we focus on tensile bifurcations, the load  $P$  is assumed to be negative, which leads to a negative right-hand side of (C.40), and the condition is satisfied by a certain value of  $kL/2$  smaller than  $\pi$ . The corresponding critical load in tension needs to be determined numerically and it is different from the negative root of quadratic equation (C.27).

It is important to realize that  $k$  and  $P$  are not two independent variables, since they are linked by (C.24). Therefore, if  $P$  is considered as the primary

unknown, equation (C.40) should be written in its fully explicit form as

$$\tan\left(\frac{L}{2}\sqrt{\frac{(1+\beta P)P}{EI}}\right) = \left(1 - \frac{P}{EA}\right) \frac{PL}{2EI} \sqrt{\frac{EI}{(1+\beta P)P}} \quad (\text{C.52})$$

We are looking for the negative root  $P$  with the smallest absolute value. To facilitate the analysis, let us convert the problem into the dimensionless format by substituting  $P = -EA\varepsilon$ ,  $EI = EAL^2/(4s^2)$  and  $\beta = (1-\Gamma)/(\Gamma EA)$  where  $\varepsilon > 0$  is the tensile strain, playing the role of the primary unknown,  $s$  is the slenderness derived from the buckling length  $L_b = L/2$ , and  $\Gamma = GA_s/(EA)$  is the sectional stiffness ratio. The resulting dimensionless equation reads

$$F(\varepsilon) \equiv \sqrt{\frac{1-\Gamma}{\Gamma} - \frac{1}{\varepsilon}} \tan\left(s\sqrt{\left(\frac{1-\Gamma}{\Gamma}\varepsilon - 1\right)\varepsilon}\right) + s(1+\varepsilon) = 0 \quad (\text{C.53})$$

The expressions under the square root must be non-negative, which is possible only if  $\Gamma < 1$  and  $\varepsilon > \Gamma/(1-\Gamma) \equiv \varepsilon_{Rt}^{(ss)}$  where  $\varepsilon_{Rt}^{(ss)}$  is the strain defined in (C.51). In terms of the sectional stiffness, the first constraint is equivalent to  $GA_s < EA$ .

For  $s > 0$  and  $\Gamma < 1$ , function  $F$  on the left-hand side of (C.53) is increasing at all points  $\varepsilon \in [\Gamma/(1-\Gamma), \infty)$  at which it is defined (remains finite). It is not defined for values of  $\varepsilon$  for which the argument of the tangent function is equal to an odd multiple of  $\pi/2$ . The first of these special points is

$$\varepsilon_1 = \frac{\Gamma}{2(1-\Gamma)} \left( \sqrt{1 + \frac{(1-\Gamma)\pi^2}{\Gamma s^2}} + 1 \right) \quad (\text{C.54})$$

It is easy to show that  $F(\Gamma/(1-\Gamma)) > 0$  (because the first term in (C.53) vanishes and the second term is positive), and since  $F$  is increasing on the interval  $[\Gamma/(1-\Gamma), \varepsilon_1)$ , equation (C.53) has no solution in this interval. As  $\varepsilon_1$  is crossed, the value of  $F$  jumps “from plus infinity to minus infinity”, and then it increases continuously. At  $\varepsilon = \varepsilon_{Rt}$ , the argument of the tangent function is  $\pi$ , and so the first term vanishes while the second term is positive. Consequently,  $F(\varepsilon_{Rt}) > 0$ , and the interval  $(\Gamma/(1-\Gamma), \varepsilon_{Rt})$  must contain exactly one solution of equation (C.53). Since this solution is smaller than  $\varepsilon_{Rt}$ , the bifurcation occurs at a lower strain level (and lower load level) than predicted by formula (C.49), which was derived from condition (C.39) instead of (C.40). The dependence of the critical strain  $\varepsilon_{Rt}^{(dc)}$  that represents the smallest positive solution of equation (C.53) on the slenderness is indicated in Fig. C.17 by the solid curves. They were constructed numerically

by solving equation (C.53) on the interval  $(\Gamma/(1-\Gamma), \varepsilon_{Rt}(s))$  using the Newton method. Superscript 'dc' refers to a 'double clamped' bar. For a given slenderness, the critical strain evaluated for a bar clamped at both ends is always between the critical strain  $\varepsilon_{Rt}^{(ss)}$  for a simply supported bar and the critical strain  $\varepsilon_{Rt}$  evaluated from formula (C.49), which turns out to be valid only for a **bar clamped at one end**. Let us recall that the slenderness is understood as the ratio  $s = L_b/i_y$  where  $i_y = \sqrt{I/A}$  is the sectional radius of inertia and  $L_b$  is the buckling length, which is still taken as  $L_b = 2L$  for a bar clamped at one end and  $L_b = L/2$  for a bar clamped at both ends, even though these standard expressions lose their physical meaning—they do not represent here the distance between the inflexion points of the bifurcated centerline.

The foregoing observation motivates a deeper investigation of the “buckling mode” that corresponds to the tensile bifurcation.

1. For a **bar clamped at one end**, the buckling mode is described by functions

$$\delta\varphi(\xi) = \widehat{\delta\varphi} \sin \frac{\pi\xi}{2L} \quad (\text{C.55})$$

$$\delta z_s(\xi) = \left( \sqrt{1 + \frac{(1-\Gamma)\pi^2}{\Gamma s^2}} - 1 \right) \frac{L\widehat{\delta\varphi}}{\pi} \left( 1 - \cos \frac{\pi\xi}{2L} \right) \quad (\text{C.56})$$

The rotation function is obtained from the general solution (C.23) by substituting  $\delta Z_{ab} = 0$  and  $C_1 = 0$  and by formally replacing the arbitrary constant  $C_2$  by  $\widehat{\delta\varphi}$ , interpreted as the maximum rotation found at the free end. The lateral displacement function is then constructed by integrating the right-hand side of (C.19) and imposing boundary condition  $\delta z_s(0) = 0$ .

Recall that the tensile bifurcation occurs only if  $GA_s < EA$ , i.e.,  $\Gamma < 1$ . Therefore, if constant  $\widehat{\delta\varphi}$  is positive and all sections rotate counterclockwise, then the deflection is also positive along the bar and the centerline moves downward. For an Euler or Kirchhoff beam with the same deformed shape of the centerline, the sign of the rotation would be negative. This means that the sections rotate in the opposite direction than the centerline, which amplifies the shear strains.

As an example, consider the stiffness ratio  $\Gamma = 1/3$  and slenderness  $s = 20$ . The corresponding critical strain is 0.5236, and the ratio between the magnitudes of the shear angle  $\delta\chi = \delta\varphi + \delta z'_s/(1 + \varepsilon_{crit}^{ten})$  and of the angle  $\delta\varphi_{Euler} = -\delta z'_s/(1 + \varepsilon_{crit}^{ten})$  by which the centerline deviates from the undeformed axis is 33.3. Therefore, after the bifurcation, the

centerline remains “almost straight” and the rotation of the sections is mainly due to shear distortion, as will be illustrated by a numerically simulated post-critical deformed shape in Fig. 14a.

2. For a **simply supported bar**, the buckling mode is characterized by a constant rotation function and zero displacement function, which can be formally described by

$$\delta\varphi(\xi) = \widehat{\delta\varphi} \quad (\text{C.57})$$

$$\delta z_s(\xi) = 0 \quad (\text{C.58})$$

This special case was mentioned in the discussion leading to formula (C.51). Here, the centerline remains straight while all sections rotate by the same angle; see Fig. 14b.

3. For a **bar clamped at both ends**, the buckling mode is described by functions

$$\delta\varphi(\tilde{\xi}) = \frac{\widehat{\delta\varphi}}{1 - \cos \kappa} \left( \cos \kappa \tilde{\xi} - \cos \kappa \right) \quad (\text{C.59})$$

$$\delta z_s(\tilde{\xi}) = \frac{L \widehat{\delta\varphi}}{1 - \cos \kappa} \left( \frac{2\kappa}{s^2 \varepsilon_{Rt}^{(dc)}} \left( \sin \kappa + \sin \kappa \tilde{\xi} \right) + \left( 1 + \varepsilon_{Rt}^{(dc)} \right) \frac{1 + \tilde{\xi}}{2} \cos \kappa \right) \quad (\text{C.60})$$

where

$$\tilde{\xi} = \frac{2\xi}{L} - 1 \quad (\text{C.61})$$

is a normalized coordinate that varies from  $-1$  at the left end to  $1$  at the right end,

$$\kappa = \frac{s}{2} \sqrt{\left( \frac{1 - \Gamma}{\Gamma} \varepsilon_{Rt}^{(dc)} - 1 \right) \varepsilon_{Rt}^{(dc)}} \quad (\text{C.62})$$

is an auxiliary variable introduced for convenience, and  $\varepsilon_{Rt}^{(dc)}$  is the smallest positive solution of equation (C.53). Constant  $\widehat{\delta\varphi}$  represents the rotation in the middle of the bar (at  $\tilde{\xi} = 0$ ). An example of a deformed shape in a post-critical state will be shown in Fig. 14c.

### Appendix C.3. Critical load – Ziegler model

The fundamental solution (C.1)–(C.3) satisfies not only the governing equations of the Reissner model, but also equations (A.83)–(A.84) and (A.87), which describe the Ziegler model. However, if the state is perturbed,

the linear equations that link the infinitesimal perturbations are different. For the Ziegler model, we obtain

$$\delta x'_s = 0 \quad (\text{C.63})$$

$$\delta z'_s = \left(1 - \frac{P}{EA}\right) \frac{\left(1 - \frac{P}{EA}\right) \delta Z_{ab} + GA_s \delta \varphi}{\left(1 - \frac{P}{EA}\right) P - GA_s} \quad (\text{C.64})$$

$$\delta \varphi' = \frac{1}{EI} \left( P \delta z_s - \delta M_{ab} - \delta Z_{ab} \left(1 - \frac{P}{EA}\right) \xi \right) \quad (\text{C.65})$$

Similar to the procedure used for the Reissner model, the second and third equations can be combined into a second-order differential equation

$$EI \left( \left(1 - \frac{P}{EA}\right) P - GA_s \right) \delta \varphi'' - \left(1 - \frac{P}{EA}\right) P GA_s \delta \varphi = \left(1 - \frac{P}{EA}\right) GA_s \delta Z_{ab} \quad (\text{C.66})$$

with a single unknown function,  $\delta \varphi$ . The general solution has the form

$$\delta \varphi(\xi) = -\frac{\delta Z_{ab}}{P} + C_1 \cos k\xi + C_2 \sin k\xi \quad (\text{C.67})$$

where

$$k = \sqrt{\frac{P}{EI} \cdot \frac{1 - \frac{P}{EA}}{1 - \left(1 - \frac{P}{EA}\right) \frac{P}{GA_s}}} \quad (\text{C.68})$$

Of course, this is based on the assumption that the expression under the square root is positive.

Integration constants  $C_1$  and  $C_2$  and also unknowns  $\delta Z_{ab}$  and  $\delta M_{ab}$  have to be determined from the boundary conditions. It is possible to treat various combinations of boundary conditions in a unified way, simply by introducing the appropriate buckling length.

1. For a column clamped at one end and free at the other, we set  $\delta Z_{ab} = 0$ , and the integration constants are determined from conditions  $\delta \varphi(0) = 0$  and  $\delta \varphi'(L) = 0$ . A nontrivial solution exists if  $\cos kL = 0$ , and the smallest positive value of  $k$  satisfying this condition is  $\pi/(2L)$ , which can be written as  $\pi/L_b$  where  $L_b = 2L$  is the buckling length.
2. For a simply supported column, we set again  $\delta Z_{ab} = 0$  and  $\delta M_{ab} = 0$ , and the integration constants are determined from conditions  $\delta \varphi'(0) =$

0 and  $\delta\varphi'(L) = 0$ . A nontrivial solution exists if  $\sin kL = 0$ , and the smallest positive value of  $k$  satisfying this condition is  $\pi/L$ , which can be written as  $\pi/L_b$  where  $L_b = L$  is the buckling length.

3. For a column clamped at both ends, we have to treat  $\delta Z_{ab} = 0$  and  $\delta M_{ab} = 0$  as unknowns and determine them simultaneously with the integration constants from conditions  $\delta\varphi(0) = 0$ ,  $\delta z_s(0) = 0$ ,  $\delta\varphi(L) = 0$  and  $\delta z_s(L) = 0$ . A nontrivial solution exists if  $\cos kL = 1$ , and the smallest positive value of  $k$  satisfying this condition is  $2\pi/L$ , which can be written as  $\pi/L_b$  where  $L_b = L/2$  is the buckling length.

The bifurcation condition can thus be written in a unified way as  $k = \pi/L_b$ , and when  $k$  is replaced by the expression in (C.68), the condition can be rewritten as

$$\left(\frac{1}{GA_s} + \frac{1}{P_E}\right) \left(1 - \frac{P}{EA}\right) P = 1 \quad (\text{C.69})$$

where  $P_E = EI\pi^2/L_b^2$  is the Euler buckling load evaluated for the given buckling length. In terms of  $P$ , condition (C.69) is a quadratic equation with roots

$$P = \frac{EA}{2} \left(1 \pm \sqrt{1 - \frac{4}{EA} \frac{P_E GA_s}{P_E + GA_s}}\right) \quad (\text{C.70})$$

If the discriminant (expression under the square root) is non-negative, both roots are positive. The lower value is obtained with the negative sign in front of the square root. The critical load for the Ziegler model under compression is thus given by

$$P_{Zc} = \frac{EA}{2} \left(1 - \sqrt{1 - \frac{4}{EA} \frac{P_E GA_s}{P_E + GA_s}}\right) = \frac{EA}{2} \left(1 - \sqrt{1 - \frac{4\pi^2\Gamma}{\Gamma s^2 + \pi^2}}\right) \quad (\text{C.71})$$

which is clearly an expression different from formula (C.42) that was derived for the Reissner model. Another difference is that, for the Ziegler model, bifurcation in tension is not possible, because we have not obtained any negative root.

In some cases the discriminant of equation (C.69) can be negative and the roots are then complex, which means that the fundamental solution never bifurcates (even in compression). The condition of a nonnegative discriminant can be converted into

$$(4GA_s - EA) P_E \leq EAGA_s \quad (\text{C.72})$$

For  $\Gamma \equiv GA_s/(EA) \leq 1/4$ , this condition is always satisfied and the critical load can indeed be evaluated from (C.71). For  $\Gamma \equiv GA_s/(EA) > 1/4$ , real roots are obtained only if the Euler load satisfies the condition

$$P_E \leq \frac{EAGA_s}{4GA_s - EA} = EA \frac{\Gamma}{4\Gamma - 1} \quad (\text{C.73})$$

which can be expressed in terms of slenderness as

$$s \geq \pi \sqrt{4 - \frac{1}{\Gamma}} \quad (\text{C.74})$$

It is interesting to explore what would happen if the condition is satisfied as an equality. For the typical case with  $\Gamma = 1/3$ , this corresponds to slenderness  $s = \pi$  and Euler load  $P_E = EA$ . The corresponding Ziegler critical load is  $P_{Zc} = EA/2$ . If the slenderness is reduced just a little bit, the critical load jumps to infinity. This can be interpreted as a consequence of the fact that by compressing the column, we make it shorter and thus reduce the buckling length, which has a stabilizing effect. On the other hand, the increasing compressive stress has a destabilizing effect. For very stocky columns, the stabilizing effect may dominate. Let us emphasize once again that analysis of such extreme cases is meant to elucidate the asymptotic properties of the mathematical model, while from the physical point of view it is not realistic to assume that the linear stress-strain law would still be applicable.

In summary, a bifurcation in compression is possible when  $\Gamma \leq 1/4$  (i.e.,  $4GA_s \leq EA$ ) or the slenderness satisfies condition (C.74). The corresponding critical strain is given by

$$\varepsilon_{Zc} = \frac{P_{Zc}}{EA} = \frac{1}{2} \left( 1 - \sqrt{1 - \frac{4\pi^2\Gamma}{\Gamma s^2 + \pi^2}} \right) \quad (\text{C.75})$$

Its dependence on the slenderness is illustrated by the graphs in Fig. C.18, where part (a) provides the global view and part (b) reveals more details in the range of low critical strains. For  $\Gamma = 1$ , the critical strain is given by

$$\varepsilon_{Zc} = \frac{1}{2} \left( 1 - \sqrt{\frac{s^2 - 3\pi^2}{s^2 + \pi^2}} \right), \quad \text{for } s \geq \sqrt{3}\pi \quad (\text{C.76})$$

and in the limit of  $\Gamma \rightarrow \infty$ , it is given by

$$\varepsilon_{Zc} = \frac{1}{2} \left( 1 - \sqrt{1 - \frac{4\pi^2}{s^2}} \right), \quad \text{for } s \geq 2\pi \quad (\text{C.77})$$

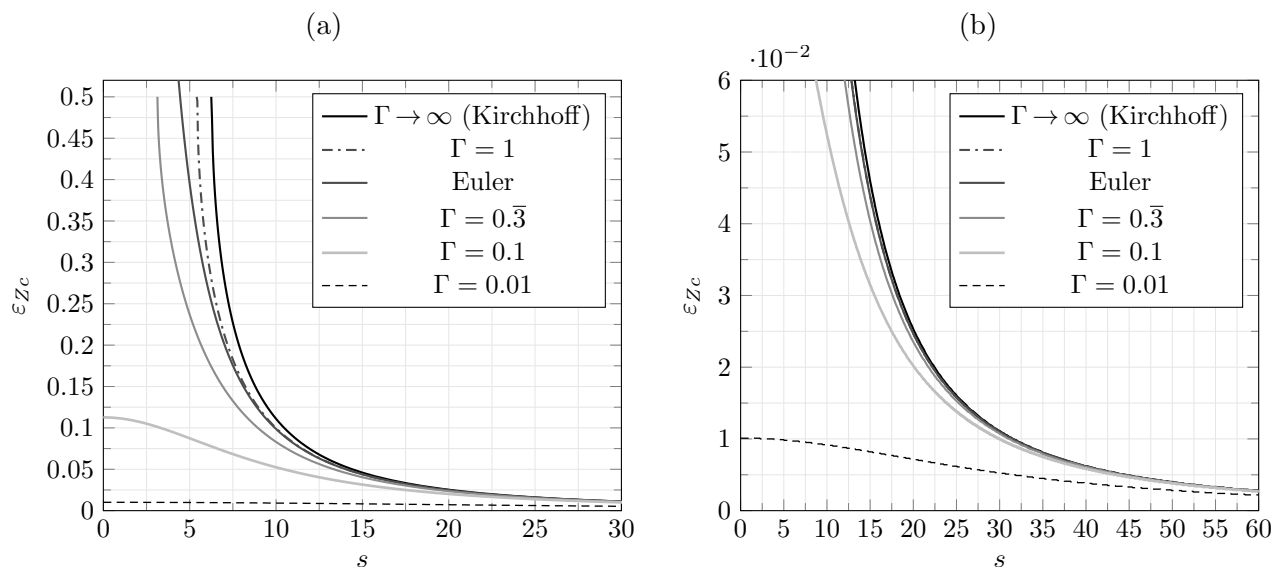


Figure C.18: Ziegler model: (a) dependence of the compressive critical strain  $\varepsilon_{Zc} = P_{Zc}/EA$  on the slenderness  $s$  for selected values of parameter  $\Gamma = GA_s/EA$ , (b) close-up view for small critical strain values.

For comparison, the Euler hyperbola is plotted in black.

For large slenderness  $s$  and general stiffness ratio  $\Gamma$ , one can use the approximation

$$\varepsilon_{Zc} \approx \frac{\pi^2 \Gamma}{\pi^2 + \Gamma s^2} \quad (\text{C.78})$$

which shows that the Euler hyperbola is approached (from below) as  $s \rightarrow \infty$ . In the opposite extreme, when the slenderness tends to zero, the limit behavior of the curve depends on the stiffness ratio  $\Gamma$ . For  $\Gamma \leq 1/4$ , the critical strain approaches a finite limit

$$\varepsilon_{Zc}|_{s=0} = \frac{1}{2} \left( 1 - \sqrt{1 - 4\Gamma} \right) \quad (\text{C.79})$$

which remains below 50 %. For  $\Gamma > 1/4$ , the critical strain attains its maximum value of 50 % when the slenderness becomes equal to  $\pi\sqrt{4 - 1/\Gamma}$ , and there is no bifurcation (and thus no critical strain) for still smaller slenderness values.

The effect of shear on stability was in a simplified form taken into account by Engesser[26], who proceeded in analogy to the Euler solution and preserved the assumption of axial incompressibility. Formula (9) from



Engesser[26] would be in the present notation written as

$$P_{Zc} = \frac{P_E}{1 + \frac{P_E}{GA_s}} \quad (\text{C.80})$$

This agrees with the solution of the reduced version of equation (C.69), in which  $EA$  is considered as infinite and thus the terms with  $EA$  in the denominator are deleted. The resulting equation is linear and has a unique solution (C.80).

An extension of Engesser’s analysis to the case of axially compressible columns was developed by Ziegler[27], who also critically compared both approaches to the stability of shear-flexible columns (Haringx versus Engesser/Ziegler) and identified the definition of internal forces as the reason why the results differ. Formula (5.14) from Ziegler[27] agrees with our (C.70). Ziegler restricted attention to the initial deviation from a straight shape and used certain approximations. Nevertheless, his sectional equations (4.5) exactly correspond to our (A.52), (A.72) and (A.54), and they can form a basis of a geometrically exact beam theory, which is why we refer to the formulation presented in Section Appendix A.2 as the Ziegler model. The link between the choice of sectional equations for beam models and large-strain continuum elasticity was also discussed by Bažant[44] and further developed in the Stability of Structures textbook by Bažant and Cedolin[45].

## References

- [1] S. Antman, *Nonlinear Problems of Elasticity*, Applied Mathematical Sciences, Springer New York, 2005.  
URL [https://books.google.it/books?id=\\_MagNyCXNqMC](https://books.google.it/books?id=_MagNyCXNqMC)
- [2] L. Euler, *De curvis elasticis*, Lausanne and Geneva: Bousquet (1744).
- [3] G. Kirchhoff, Ueber das Gleichgewicht und die Bewegung eines unendlich dünnen elastischen Stabes, *Journal für die reine und angewandte Mathematik* 1859 (56) (1859) 285–313.
- [4] S. Timoshenko, LXVI. On the correction for shear of the differential equation for transverse vibrations of prismatic bars, *The London, Edinburgh, and Dublin Philosophical Magazine and Journal of Science* 41 (245) (1921) 744–746. doi:10.1080/14786442108636264.

- [5] E. Reissner, On one-dimensional finite-strain beam theory: the plane problem, *Zeitschrift für angewandte Mathematik und Physik ZAMP* 23 (5) (1972) 795–804.
- [6] J. C. Simo, A finite strain beam formulation. The three-dimensional dynamic problem. I, *Computer Methods in Applied Mechanics and Engineering* 49 (1) (1985) 55–70.
- [7] T. Belytschko, L. Schwer, M. J. Klein, Large displacement, transient analysis of space frames, *International Journal for Numerical Methods in Engineering* 11 (1) (1977) 65–84. arXiv:<https://onlinelibrary.wiley.com/doi/pdf/10.1002/nme.1620110108>, doi:10.1002/nme.1620110108.  
URL <https://onlinelibrary.wiley.com/doi/abs/10.1002/nme.1620110108>
- [8] M. Crisfield, A consistent co-rotational formulation for non-linear, three-dimensional, beam-elements, *Computer Methods in Applied Mechanics and Engineering* 81 (2) (1990) 131–150. doi:[https://doi.org/10.1016/0045-7825\(90\)90106-V](https://doi.org/10.1016/0045-7825(90)90106-V).  
URL <https://www.sciencedirect.com/science/article/pii/004578259090106V>
- [9] C. Oran, A. Kassimali, Large deformations of framed structures under static and dynamic loads, *Computers & Structures* 6 (6) (1976) 539–547. doi:[https://doi.org/10.1016/0045-7949\(76\)90050-X](https://doi.org/10.1016/0045-7949(76)90050-X).  
URL <https://www.sciencedirect.com/science/article/pii/004579497690050X>
- [10] A. A. Shabana, H. A. Hussien, J. L. Escalona, Application of the Absolute Nodal Coordinate Formulation to Large Rotation and Large Deformation Problems, *Journal of Mechanical Design* 120 (2) (1998) 188–195. doi:10.1115/1.2826958.  
URL <https://doi.org/10.1115/1.2826958>
- [11] J. Gerstmayr, H. Sugiyama, A. Mikkola, Review on the Absolute Nodal Coordinate Formulation for Large Deformation Analysis of Multibody Systems, *Journal of Computational and Nonlinear Dynamics* 8 (3) (2013) 031016. doi:10.1115/1.4023487.  
URL <https://doi.org/10.1115/1.4023487>
- [12] A. Pagani, E. Carrera, Unified formulation of geometrically nonlinear refined beam theories, *Mechanics of Advanced Materials and Structures*

- 25 (1) (2018) 15–31. arXiv:<https://doi.org/10.1080/15376494.2016.1232458>, doi:[10.1080/15376494.2016.1232458](https://doi.org/10.1080/15376494.2016.1232458).  
URL <https://doi.org/10.1080/15376494.2016.1232458>
- [13] P. Jung, S. Leyendecker, J. Linn, M. Ortiz, A discrete mechanics approach to the cosserat rod theory—part 1: static equilibria, *International Journal for Numerical Methods in Engineering* 85 (1) (2011) 31–60. doi:<https://doi.org/10.1002/nme.2950>.  
URL <https://onlinelibrary.wiley.com/doi/abs/10.1002/nme.2950>
- [14] A. Tasora, S. Benatti, D. Mangoni, R. Garziera, A geometrically exact isogeometric beam for large displacements and contacts, *Computer Methods in Applied Mechanics and Engineering* 358 (2020) 112635. doi:<https://doi.org/10.1016/j.cma.2019.112635>.  
URL <https://www.sciencedirect.com/science/article/pii/S0045782519305195>
- [15] E. Marino, Isogeometric collocation for three-dimensional geometrically exact shear-deformable beams, *Computer Methods in Applied Mechanics and Engineering* 307 (2016) 383–410. doi:<https://doi.org/10.1016/j.cma.2016.04.016>.  
URL <https://www.sciencedirect.com/science/article/pii/S0045782516302080>
- [16] P. Frank Pai, Energy-consistent formulation and order deficiency of linear and nonlinear shear-deformable beam theories, *Thin-Walled Structures* 65 (2013) 7–13. doi:<https://doi.org/10.1016/j.tws.2013.01.001>.  
URL <https://www.sciencedirect.com/science/article/pii/S0263823113000025>
- [17] P. F. Pai, Problems in geometrically exact modeling of highly flexible beams, *Thin-Walled Structures* 76 (2014) 65–76. doi:<https://doi.org/10.1016/j.tws.2013.11.008>.  
URL <https://www.sciencedirect.com/science/article/pii/S0263823113002930>
- [18] A. Mohyeddin, A. Fereidoon, An analytical solution for the large deflection problem of Timoshenko beams under three-point bending, *International Journal of Mechanical Sciences* 78 (2014) 135–139. doi:<https://doi.org/10.1016/j.ijmecsci.2013.11.005>.

URL <https://www.sciencedirect.com/science/article/pii/S002074031300307X>

- [19] H. Beiranvand, S. A. A. Hosseini, New nonlinear first-order shear deformation beam model based on geometrically exact theory, *Journal of Vibration Engineering & Technologies* 11 (8) (2023) 4187–4204. doi:10.1007/s42417-022-00809-0.  
URL <https://doi.org/10.1007/s42417-022-00809-0>
- [20] R. A. Mejia-Nava, I. Imamovic, E. Hajdo, A. Ibrahimbegovic, Nonlinear instability problem for geometrically exact beam under conservative and non-conservative loads, *Engineering Structures* 265 (2022) 114446. doi:<https://doi.org/10.1016/j.engstruct.2022.114446>.  
URL <https://www.sciencedirect.com/science/article/pii/S0141029622005569>
- [21] P. Di Re, D. Addressi, C. Gatta, L. Parente, E. Sacco, Corotational force-based beam finite element with rigid joint offsets for 3d framed structures, *Computer Methods in Applied Mechanics and Engineering* 419 (2 2024). doi:10.1016/j.cma.2023.116656.
- [22] M.-Y. Kim, A. I. Mehdi, M. M. Attard, Finite strain theories of extensible and shear-flexible planar beams based on three different hypotheses of member forces, *International Journal of Solids and Structures* 193-194 (2020) 434–446. doi:<https://doi.org/10.1016/j.ijsolstr.2020.02.029>.  
URL <https://www.sciencedirect.com/science/article/pii/S002076832030069X>
- [23] M. Horák, E. La Malfa Ribolla, M. Jirásek, Efficient formulation of a two-noded geometrically exact curved beam element, *International Journal for Numerical Methods in Engineering* 124 (3) (2023) 570–619. doi:<https://doi.org/10.1002/nme.7133>.  
URL <https://onlinelibrary.wiley.com/doi/abs/10.1002/nme.7133>
- [24] M. Jirásek, E. La Malfa Ribolla, M. Horák, Efficient finite difference formulation of a geometrically nonlinear beam element, *International Journal for Numerical Methods in Engineering* 122 (2021) 7013–7053. doi:10.1002/nme.6820.
- [25] J. A. Haringx, On the buckling and the lateral rigidity of helical compression springs I, *Proc. Konink. Ned. Akad. Wet.* 45 (1942) 533–539.

- [26] F. Engesser, Die Knickfestigkeit gerader Stäbe, *Centralblatt der Bauverwaltung* 11 (49) (1891) 483–486.
- [27] H. Ziegler, Arguments for and against Engesser’s buckling formulas, *Ingenieur-Archiv* 52 (1982) 105–113.
- [28] J. Gerstmayr, H. Irschik, On the correct representation of bending and axial deformation in the absolute nodal coordinate formulation with an elastic line approach, *Journal of Sound and Vibration* 318 (3) (2008) 461–487.
- [29] J. C. Simo, L. Vu-Quoc, A three-dimensional finite-strain rod model. Part II: Computational aspects, *Computer Methods in Applied Mechanics and Engineering* 58 (1) (1986) 79–116.
- [30] G. R. Cowper, The shear coefficient in Timoshenko’s beam theory, *Journal of Applied Mechanics ASME* (1966) 335–340.  
URL [http://asmedigitalcollection.asme.org/appliedmechanics/article-pdf/33/2/335/5447638/335\\_1.pdf](http://asmedigitalcollection.asme.org/appliedmechanics/article-pdf/33/2/335/5447638/335_1.pdf)
- [31] M. Batista, A closed-form solution for reissner planar finite-strain beam using jacobi elliptic functions, *International Journal of Solids and Structures* 87 (2016) 153–166. doi:10.1016/J.IJSOLSTR.2016.02.020.
- [32] C. M. Lyritsakis, C. P. Andriotis, K. G. Papakonstantinou, Geometrically exact hybrid beam element based on nonlinear programming, *International Journal for Numerical Methods in Engineering* 122 (2021) 3273–3299. doi:10.1002/nme.6663.
- [33] M. Jamshidian, N. Boddeti, D. Rosen, O. Weeger, Multiscale modelling of soft lattice metamaterials: Micromechanical nonlinear buckling analysis, experimental verification, and macroscale constitutive behaviour, *International Journal of Mechanical Sciences* 188 (2020) 105956. doi:https://doi.org/10.1016/j.ijmecsci.2020.105956.  
URL <https://www.sciencedirect.com/science/article/pii/S002074032032419X>
- [34] J.-M. Battini, C. Pacoste, A. Eriksson, Improved minimal augmentation procedure for the direct computation of critical points, *Computer Methods in Applied Mechanics and Engineering* 192 (16) (2003) 2169–2185. doi:https://doi.org/10.1016/S0045-7825(03)00254-8.  
URL <https://www.sciencedirect.com/science/article/pii/S0045782503002548>

- [35] M. Batista, A closed-form solution for Reissner planar finite-strain beam using Jacobi elliptic functions, *International Journal of Solids and Structures* 87 (2016) 153–166. doi:<https://doi.org/10.1016/j.ijsolstr.2016.02.020>.  
URL <https://www.sciencedirect.com/science/article/pii/S0020768316000822>
- [36] H. Irschik, J. Gerstmayr, A continuum mechanics based derivation of Reissner’s large-displacement finite-strain beam theory: the case of plane deformations of originally straight Bernoulli–Euler beams, *Acta Mechanica* 206 (1) (2009) 1–21.
- [37] A. Humer, Exact solutions for the buckling and postbuckling of shear-deformable beams, *Acta Mechanica* 224 (7) (2013) 1493–1525.
- [38] A. Ibrahimbegović, On finite element implementation of geometrically nonlinear Reissner’s beam theory: three-dimensional curved beam elements, *Computer methods in applied mechanics and engineering* 122 (1–2) (1995) 11–26.
- [39] M. A. Crisfield, G. Jelenić, Objectivity of strain measures in the geometrically exact three-dimensional beam theory and its finite-element implementation, *Proceedings of the Royal Society of London. Series A: Mathematical, Physical and Engineering Sciences* 455 (1983) (1999) 1125–1147.
- [40] I. Elishakoff, Who developed the so-called Timoshenko beam theory?, *Mathematics and Mechanics of Solids* 25 (1) (2020) 97–116. doi:10.1177/1081286519856931.
- [41] D. Genovese, I. Elishakoff, Shear deformable rod theories and fundamental principles of mechanics, *Archive of Applied Mechanics* 89 (10) (2019) 1995–2003.
- [42] J. Blaauwendraad, Shear in Structural Stability: On the Engesser–Haringx Discord, *Journal of Applied Mechanics* 77 (3) (2010) 031005. arXiv:[https://asmedigitalcollection.asme.org/appliedmechanics/article-pdf/77/3/031005/5479538/031005\\_1.pdf](https://asmedigitalcollection.asme.org/appliedmechanics/article-pdf/77/3/031005/5479538/031005_1.pdf), doi:10.1115/1.3197142.  
URL <https://doi.org/10.1115/1.3197142>

- [43] D. Zaccaria, D. Bigoni, G. Noselli, D. Misseroni, Structures buckling under tensile dead load, *Proceedings of the Royal Society A: Mathematical, Physical and Engineering Sciences* 467 (2011) 1686–1700. doi:10.1098/rspa.2010.0505.
- [44] Z. P. Bažant, A correlation study of formulations of incremental deformation and stability of continuous bodies, *Journal of Applied Mechanics* 38 (1971) 919–928.  
URL <https://api.semanticscholar.org/CorpusID:121226196>
- [45] Z. P. Bažant, L. Cedolin, *Stability of Structures*, Oxford University Press, 1991.